Imaging and Genetics of Two Amyloid Related Diseases: Alzheimer's Disease and Down Syndrome

By

Mary Ellen I. Koran

Dissertation

Submitted to the Faculty of the

Graduate School of Vanderbilt University

in partial fulfillment of the requirements

for the degree of

DOCTOR OF PHILOSOPHY

in

Human Genetics

May, 2014

Nashville, Tennessee

Approved:

Jonathan Haines, PhD

Dana Crawford, PhD

Brian Welch, PhD

Chun Li, PhD

Tricia Thornton-Wells, PhD

DEDICATION

To my parents, sister, Cody, friends, and family for all of their encouragement and support throughout this adventure.

ACKNOWLEDGEMENTS

First, I would like to thank Dr. Tricia Thornton-Wells, who has been an amazing mentor, incredibly supportive and encouraging, and from whom I have learned much about mentoring students. I would also like to thank my committee members, Drs. Jonathan Haines, Dana Crawford, Chun Li, and Brian Welch whose constructive guidance helped guide and shape this dissertation and my career as a scientist. Dr. Haines has provided valuable insight into deciphering the genetics of Alzheimer's Disease, which resulted in significant contributions to Chapters 4 and 5 of this dissertation, and has been an indispensable mentor from the beginning, encouraging me to continue in the pursuit of a scientific career. Drs. Crawford and Li have substantially influenced the work described in Chapters 4 and 5, providing expertise in the statistical interpretation of the results and the construction of the applied methods, in addition to their encouraging reflections. Dr. Welch's contributions to Chapters 2 and 3 were indispensable: his knowledge of magnetic resonance physics, and more importantly, his ability and willingness to teach and share this knowledge were vital throughout the application and optimization of the sequences, the implementation of post-processing analyses, and the interpretation of the results. He was always supportive and positive, and has the rare talent of being able to turn extremely difficult theories into easily digestible concepts.

I would like to thank others beyond my committee as well. Dr. Timothy J. Hohman has applied his considerable expertise in neuroscience, imaging, statistics, and programming to this entire dissertation; I honestly would not have been able to accomplish as much as I did without his help and guidance. He is always willing to drop what he is doing to help others, and for this I am eternally grateful. R. Michael Sivley has applied his extensive

knowledge in programming to this entire dissertation as well, particularly Chapter 2 and Appendix A. Both Mike and Tim have become friends to me, and lab would not be the same without them here.

I would like to thank all the study volunteers for their time and willingness to participate in this research; without them this body of work would not exist.

I would like to thank my friends and family. From the beginning, they have been extremely loving and supportive. My mother has provided the encouragement to pursue whatever interests I could possibly imagine, my father has instilled the drive, ambition, and perseverance that continue to shape my personality and decisions, and my sister keeps me in check and brings me “back to earth” when I get too far away. Finally, I must thank my partner in life, Cody Goodwin. I honestly don’t think I would have made it through the tedium that is the first year of medical school without him. He provides me with balance and a healthy perspective on life and work, stimulates me intellectually, and most importantly, loves me unconditionally.

TABLE OF CONTENTS

Page

LIST OF TABLES

LIST OF FIGURES

Chapter 1

IMAGING GENETICS OF ALZHEIMER'S DISEASE AND DOWN SYNDROME: TWO AMYLOID BASED DISEASES

The advancement of *in vivo* imaging modalities that detect the neuropathologies associated with both Down Syndrome and Alzheimer's Disease present new opportunities to explore these diseases in living human subjects. Previously, these neuropathologies could not be detected until after autopsy or in a living patient, with a rarely taken brain biopsy. The use of quantitative traits derived from these imaging modalities offers increased power to detect associations with large-scale genetic data, and these studies fall under the category of *imaging genetics*. Imaging genetics studies can identify novel risk genes and elucidate gene function and novel mechanisms of disease pathology and etiology. Recent imaging genetics studies of the neuropathologies of Alzheimer's Disease and Down Syndrome have attempted to obtain a more complete and in depth understanding of the underlying genetic etiology of their pathologies. Here, we will briefly overview both diseases, the neuropathologies associated with each, the imaging modalities used to detect these pathologies, and finally, the studies combining these imaging modalities with genetic data.

Alzheimer's Disease

Alzheimer's Disease (AD) is an irreversible, degenerative disease of the brain that accounts for an estimated 55-75% of dementia cases each year [1]. This disorder results in a gradual loss of memory, judgment and cognitive function along with the massive

death of brain cells. While AD usually appears in individuals 65 years of age and older, less common forms do affect individuals earlier in adulthood. In 2000, there were 4.8 million people in the United States with AD , and that number is expected to increase to 13.2 million by 2050 [2], prompting many researchers throughout the scientific community to eagerly research ways in which the disease can be detected and prevented, or slowed.

Late onset Alzheimer's disease (LOAD) accounts for about 96% of AD cases and develops in patients over the age of 65, with early-onset AD affecting subjects less than 65 years of age and accounting for 4% of the AD population [3]. Clinical diagnosis of LOAD is based on a patient's symptoms and cognitive function assessed using a battery of neuropsychological tests [4]. When an individual is in the early-stages of AD, characteristic symptoms include problems with thinking, memory and concentration that may be attributed to normal aging and stress. As the disease progresses into mild cognitive impairment (MCI) and various stages of dementia, cognitive functions continue to decline. Most noticeably, short term memory becomes highly impaired [5]. In addition, language abilities, motor skills, perception and attention deteriorate eventually leaving many people unable to care for themselves and completely dependent on others [6]. Even with neuropsychological testing of these features of disease, LOAD cannot be definitively diagnosed until autopsy, when the neuropathological hallmarks can be detected. These hallmarks include amyloid beta plaques that can be immunohistochemically analyzed in brain sections [4]. Large amounts of amyloid beta peptide, a toxic protein fragment, are produced in the brain and as this peptide accumulates in the brain, extracellular senile amyloid beta plaques form [7]. Although still debated, these plaques may lead to nerve cell death and the progressive symptoms of

this disorder [8]. The brain of a patient with AD is marked by profound atrophy of the hippocampus and cerebral cortex [9].

LOAD has a complex genetic etiology that has proven difficult to unravel, involving heterogeneity and gene-gene and gene-environment interactions [1]. LOAD is not inherited in a Mendelian (dominant or recessive) manner, but the disease does cluster in families [1]. The heritability estimates of LOAD are high, with h^2 between 60 and 80%, but much of the genetic contribution to this condition remains unexplained [10,11].

Early work investigating the genetic contributions to LOAD found associations between disease status and the gene encoding apolipoprotein-E (*APOE*) [12,13]. Genetic studies in LOAD have continued with single marker genetic associations, or genome wide association studies (GWAS), in which disease status is the outcome variable. In these studies, 21 genes/genomic loci that have been confirmed to be associated with LOAD, but only *APOE* has a large effect size, with an odds ratio of about 3.7 for one copy of the high risk e4 allele [11,14]. The remaining 20 loci exhibit small effect sizes, with odds ratios hovering between 0.73 and 1.22 (these include: *BIN1, CLU, ABCA7, CR1, PICALM, MS4A6A, CD33, MS4A4E, CD2AP, EPHA1, HLA-DRB5–HLA-DRB1, PTK2B, SORL1, SLC24A4-RIN3, DSG2, INPP5D, MEF2C, NME8, ZCWPW1, CELF1, FERMT2,* and *CASS4* [11,14]. In depth reviews discussing the genetics of LOAD have been published elsewhere [15–17].

Down Syndrome

Down syndrome (DS; trisomy 21) is a neurodevelopmental disorder that is caused by the presence of three copies of chromosome 21. It occurs in 1 in every 691 live births in the US [18] and is the most common genetic cause of intellectual disability [19,20]. DS is typically

identified at birth or shortly thereafter and can be diagnosed prenatally using a combination of ultrasound, blood tests, amniocentesis, or chorionic villus sampling. Postnatally, the diagnosis of DS is initially based on common physical characteristics that can be observed in infancy, such as low muscle tone, a single crease across the palm of the hand, brachycephaly, and upward slanting palpebral fissures. Diagnosis can then be confirmed with karyotype analysis. The degree of cognitive impairment associated with DS ranges from mild to severe, with the mean IQ of 50 [20]. Individuals with DS exhibit deficits in language, verbal short term-memory, and explicit long-term memory; whereas visuospatial short-term memory, associative learning, and implicit memory are relatively preserved [21]. Common medical comorbidities include heart defects, digestive malformations, cataracts, seizures, leukemia, and sleep apnea. Advances in the treatment of these medical comorbidities have resulted in dramatic improvements in lifespan in the U.S., rising from 9 years in the early-twentieth century [22] to nearly 60 years in 2010 [23]. With this substantial increase in life expectancy for individuals with DS has come the need for an increased focus on health issues in aging people with DS. Most prominently, aging in individuals with DS is associated with an increased risk of developing AD, with up to 70 percent developing dementia by age 70 [24].

Adults with DS account for up to 60% of individuals with developmental disabilities who exhibit signs of AD [25]. The clinical presentation of AD in individuals with DS can be complex and less straightforward due to pre-existing intellectual disability. Further complicating the diagnostic picture is that the most commonly used neuropsychological batteries for assessing dementia in the general population are not effective in measuring cognitive dysfunction in people with intellectual disabilities because these subjects tend to score at or near the bottom of the normative range, exhibiting floor effects. Therefore, AD in subjects with DS is clinically diagnosed through specially designed

neuropsychological tests like the Dementia in People with Learning Disabilities (DLD), formerly known as the Dementia Questionnaire for Persons with Mental Retardation (DMR), which is commonly used to assess dementia in individuals with DS [26,27]. Generally, clinical signs of AD in persons with DS include a decline in long-term memory, learning ability, orientation, and increased dependence on caretakers [28]. However, these are often accompanied or preceded by personality changes consistent with frontal lobe dysfunction [29],as well as behavioral changes such as excessive over-activity or restlessness, sleep disturbance, an unwillingness to cooperate with caregivers, and auditory hallucinations [30]. It has been reported that the rate of deterioration increases with age in individuals with DS [28] and that the level of pre-existing cognitive function is associated with the rate of cognitive decline [31].

Postmortem studies have revealed that, by 40 years of age, nearly all individuals with DS have lesions present in the brain that meet the pathological criteria for AD, including amyloid beta plaques [32]. AD in DS may be linked to the presence of three copies of the *APP* gene, which resides on chromosome 21 and encodes the amyloid precursor protein. The extra copy of the *APP* gene leads to an increase in *APP* mRNA and protein expression in brains of individuals with DS [33]. Mutations in *APP* cause a rare autosomal dominant form of early onset AD in non-DS populations [34]. Individuals who inherit such mutations in the *APP* gene develop AD before age 65, often times as early as age 30. Isolated duplication of the *APP* locus on chromosome 21 (such that an individual would have 3 copies of *APP*) also results in an autosomal dominant, early-onset form of AD in non-DS populations [35]. Further evidence for a role of *APP* overexpression in the development of AD pathology and dementia in DS is demonstrated in a case study of an elderly adult with DS who had a microdeletion of *APP* resulting in *APP* disomy and did not develop dementia or significant AD pathology [36].

In addition to *APP* triplication, *APOE* genotype also modulates risk for developing AD in the DS population. Several studies have shown an increased risk with the *APOE*ε4 allele [36,37] and a decreased risk with *APOE*ε2 allele for individuals with DS [38], which mirrors what is observed in the general population.

In addition to the lesions seen neuropathologically in these subjects, adults with DS have reduced brain volumes compared to typically-developing controls (TDs) [21]. They exhibit a similar pattern of neurodegeneration to that seen in the early stages of AD in the general population [39] at an earlier age, and it has been suggested that this is indicative of accelerated brain aging in these patients [40].

Imaging Phenotypes in Alzheimer's Disease and Down Syndrome

Researchers and clinicians have employed multiple *in vivo* neuroimaging strategies to uncover the underlying structural, functional and pathological effects of DS and AD. Here, we will focus on the modalities that can detect changes in regional brain volume and the quantity of amyloid beta protein deposition in the brain.

Structural ImagingQuantified volumes of regions of interest in the brain can be derived from T1- or T2-weighted MRI scans and used as biomarkers of brain atrophy. Structurally, subjects with LOAD have significant deficits in volume compared to their normal aging counterparts, which can be detected by both CT and MRI sequences. AD is usually characterized by whole brain atrophy with extensive atrophy of the medial temporal lobe [41]. Structures in the medial temporal lobe, like the hippocampus, have been the focus of many of these studies, and atrophy in these structures correlates well with neuropathology found at autopsy [41]. Cortical atrophy of the medial temporal lobes, as measured using MRI in both transgenic mouse models and in humans, is a valid and

reliable biomarker for detection of preclinical LOAD [42–45]. During early stages of the disease, in subjects with MCI and early AD, atrophy is seen primarily in the entorhinal cortex and hippocampus and can reliably predict MCI conversion to AD [46,47]. The lateral ventricles, also, have repeatedly shown a relationship to AD status and progression [48–51]. The lateral ventricles normally dilate over time with age, as brain tissue volume decreases, but in patients with AD, the rate of ventricular dilation is much greater than in the normal aging population, indicative of underlying increased neuronal degeneration [52].

Volumetric MRI studies in DS subjects have revealed that adults with DS have reduced whole brain weight; reduced prefrontal, parietal, and temporal lobe volumes; and reduced amygdala, hippocampal , and cerebellar volumes compared to TD controls [21]. Adults with DS have an increase in parahippocampal volume and relatively preserved lenticular nuclei, basal ganglia, and occipital and parietal lobe volumes [21]. Non-demented elderly individuals with DS (> 50 years of age) have reduced whole brain, prefrontal, posterior cingulate, hippocampal, parahippocampal, amygdalar, and cerebellar volumes, as well as degeneration of the locus coeruleus and nucleus basalis of Meynert compared to TD controls [21]. Studies have shown that individuals with DS exhibit a similar pattern of neurodegeneration to that seen in the early stages of AD in the general population, where the earliest neuropathological changes present in the medial-temporal lobe (MTL) and progress to neocortex and subcortical regions [39]. However, a hypothesis of accelerated brain aging occurring in individuals with DS has been proposed since these changes occur earlier in DS versus TD subjects [40].

Amyloid Imaging

Positron emission tomography (PET) uses a radio-isotope tracer bound to a chemical with known physiological properties to produce images of functional or physiologic processes in the body. The isotope emits positrons which then annihilate and produce gamma ray photons that are detected by the PET scanner. Radio-labeled tracers have been developed that bind to amyloid beta plaques in living patients. Before these tracers were developed, the presence of amyloid beta plaques could only be confirmed at autopsy or through invasive brain biopsy. In AD, the tracers florbetapir (^{18}F-AV-45 or AV-45) and Pittsburgh Compound-B (PiB, *N*-methyl-[^{11}C]2-(4′-methylaminophenyl)-6-hydroxybenzothiazole) selectively bind amyloid beta plaques in living patients, have been correlated with disease onset and progression, have been validated post-mortem, and more recently have been included as biomarkers for classifying patients with AD in research studies [53–56]. In DS, florbetapir and PiB PET images have been used to quantify amyloid load and have been validated post-mortem as well [57,58].

Though PET has been approved for clinical detection of amyloid beta plaques, it is not ideal for routine screening or monitoring of patients, particularly before clinical symptoms are present, because it involves radiation exposure. The non-invasive imaging technique, T1ρ-weighted MRI (T1ρ) has been validated in a mouse model of AD to detect amyloid beta plaque *in vivo* [59] but has not yet been validated in humans. It is sensitive to chemical exchange rates, and provides a contrast that is distinct from conventional MR contrasts [60]. It is thought to be of particular use for investigating low-frequency interactions between macromolecules and water, like the interaction between amyloid beta plaques and surrounding water-based brain tissue [60].

Utilizing Imaging Modalities in Genetic Studies

By leveraging quantitative traits derived from imaging modalities, researchers can take advantage of the increased power these traits provide genetic association studies [61]. In order to do so, one must define the trait of interest first. To define phenotype, or disease status, in genetic studies, just as in the clinic, physicians and scientists traditionally depend on a patient's clinical symptoms as measured through a battery of cognitive tests [4]. There are strengths and weaknesses to using a solely clinical approach in defining outcome variable in genetic studies. This approach matches the diagnosis made in a clinical setting and these cognitive measures have been validated, normalized, and in use for decades, which allows data to be compiled across research centers. Despite these advantages, when compared to the neuropathological gold standard for diagnosis of AD at autopsy, the diagnostic accuracy of neurocognitive tests range from 65-96% and the specificity ranges between 23-88% [45]. Therefore, using only clinical disease status, as diagnosed by cognitive and neuropsychological tests, in genetic association studies introduces potential error into the results. There are many effects of a genetic variant—from protein to cell function to system physiology—that are intermediate to final disease status. Measuring these intermediate effects can provide endophenotypes for a genetic association study, potentially increasing the power to detect a genetic effect that ultimately impacts disease status [62]. To quantify these intermediary effects, biomarkers like protein levels in cerebrospinal fluid (CSF) or quantitative neuroimaging modalities like MRI and PET, have been added to the research criteria for AD diagnosis [63] and have been used in genetic studies as explored below. For AD, DS, and other neurological disorders, brain structure or pathology derived from imaging modalities can be the source of relevant quantitative traits (QTs) to be used as endophenotypes. Endophenotypes can provide increased statistical power

(and therefore decreased sample size requirements) over dichotomous outcome variables [64] and since both brain structure [65] and PET-derived amyloid load [66] are highly heritable, both are suitable as endophenotypes in genetic studies.

In recognition of this great opportunity and the need for large sample sizes for exploration of modest genetic effects, the Alzheimer's Disease Neuroimaging Initiative (ADNI) was developed. ADNI is as a joint venture between the National Institutes of Health (NIH) and private biotechnology and pharmaceutical companies with the goal of acquiring serial measurements of MRI, PET, neurocognitive testing and other biological markers, along with genetic data, in hundreds of older adults for the purpose of identifying biomarkers for early detection and monitoring of disease progression and response to treatment for AD. ADNI maintains a publicly available dataset that contains rich biomarker data on study participants with normal cognition and those diagnosed MCI or AD. This is an extraordinary resource for AD researchers, especially those interested in imaging genetics research. The availability of ADNI and other similarly sized data sets has advanced the field of imaging genetics in LOAD, by enabling the use of quantitative structural data from MRI and quantitative amyloid load from PET as endophenotypes in genetic association studies.

Imaging Genetics

Imaging Genetics in LOAD

Here we will focus on the progress made in imaging genetics of LOAD using PET and structural MRI modalities. As discussed above, structural MRI and quantified PET images are able to successfully quantify different aspects of brain pathology, and these

quantitative traits have been used in genetic association studies to confirm previous and identify novel genetic associations.

APOE

Although researchers have not yet found a specific gene that is determinative of the late onset form of AD, one genetic risk factor, *APOE*, does substantially increase a person's risk of developing the disease. *APOE* is located on chromosome 19 and encodes the protein apolipoprotein E that combines with lipids to form lipoproteins. There are three variants of this gene, *APOE* e2, *APOE* e3, and *APOE* e4 (average frequency (in percentage) across 430 populations: 6.4, 78.3, 14.5, respectively[67]). *APOE* e3, is the most common allele and, therefore, risk attributed to the other two allelic variants is compared against this reference allele. *APOE* e2 may provide some protection against the disease in younger individuals [68]. Risk for AD is highest in individuals who possess an *APOE* e4 allele. An individual's risk for developing AD increases from 20% when no *APOE* e4 alleles are present to 90% when two copies of the allele are present [13]. It is important to note, however, that the increased risk conferred by *APOE* e4 is lower for African Americans and Hispanics than it is for Caucasians [69].

Using AV-45 ligand PET images and genetic data collected by ADNI on 555 subjects, Ramanan, et.al., confirmed the association of *APOE* (rs429358) with amyloid load in Caucasian subjects [70]. In fact, there is a gene dosage effect of the e4 risk allele on PET-derived amyloid load that has been observed in cognitively normal people [71] as well as MCI subjects [72]. The *APOE* e4 allele has also been associated with faster conversion rates from MCI to AD in PIB-positive MCI subjects [73].

In a genome wide association study (GWAS) using quantitative endophenotypes derived from MRI, *APOE* has also been associated with multiple measures of brain volume, grey matter density, and cortical thickness extracted from structural MRI through FreeSurfer and voxel-based morphometry [74]. A variant in *APOE* (rs429358) was associated with volumetric measures of the left and right amygdalar and hippocampal regions, right middle temporal lobe, left and right inferior parietal lobe, and right cerebral white matter [74]. These associations were all significant at $p < 10^{-7}$.

TOMM40

TOMM40 is a gene adjacent to *APOE* and is reported to be a contributor to LOAD risk, though this is debated [70,75]. It encodes a channel-forming subunit of the multisubunit translocase of the outer mitochondrial membrane (TOMM complex), which plays a role in the transport of cytoplasmic peptides and proteins into mitochondria. Given that mitochondrial dysfunction has been widely implicated in the etiology of LOAD, this association of *TOMM40* with LOAD was logical. *TOMM40* has been associated with measures of brain structure volume, grey matter density, and cortical thickness extracted from structural MRI: a variant in *TOMM40* (rs2075650) was significantly associated with bilateral hippocampal volume and left amygdalar volume [74]. In a PET imaging GWAS, variants in *TOMM40* displayed significant association with Amyloid beta levels but, their association signals disappeared ($P > 0.05$) when APOE ε4 status was included as a covariate, so the validity of the association of *TOMM40* with LOAD and its endophenotypes is still contentious [70].

BCHE

In addition to confirming the association of APOE with amyloid load in 555 ADNI subjects with AV-45 ligand PET scans, Ramanan, et.al., discovered the association of *BCHE* (rs509208) with amyloid load [70]. *BCHE,* located on chromosome 3, encodes butyrylcholinesterase and has been associated with amyloid beta plaques and neurofibrillary tangles along with amyloid angiopathy in AD [76]. Together, variants in *BCHE* and *APOE* explained 15% of the variance in amyloid load [70]. The risk variant of *BCHE* has been associated with further risk of LOAD in *APOE* e4 carriers and with cognitive decline in the later stages of the illness [77]. However, some studies have found that the risk variant of *BCHE* has an important role in the progression of AD in which subjects carrying the risk allele, or K-variant, exhibited a slower rate of cognitive decline [78]. These observations have potential implications for the treatment of AD with cholinesterase inhibitors that inhibit the production of butyrylcholinesterase as the disease progresses.

GRIN2B

GRIN2B, located on chromosome 12, encodes the *N*-methyl-d-aspartate (NMDA) glutamate receptor NR2B subunit that has previously been associated with temporal lobe volume, excitotoxic cell death and is already a therapeutic target in Alzheimer's disease [79]. In this study, a variant in *GRIN2B* (rs10845840) was associated with bilateral temporal lobe volume with $p < 5 \times 10^{-7}$ and the risk alleles for lower temporal lobe volume at this SNP were significantly over-represented in AD and MCI subjects versus controls [79].

DHCR24

An association with *DHCR24*, encoding 24-dehydrocholesterol reductase, which confers resistance to amyloid, was discovered in the ADNI dataset using PiB-PET imaging as a quantitative trait [80]. The minor allele of an intronic SNP (rs7551288) within this gene was associated with lower amyloid beta load as measured by PiB uptake. Major allele homozygotes had higher amyloid beta load as measured by PiB uptake in frontal regions. Because of the role of *DHCR24* in conferring resistance to amyloid beta and oxidative stress-induced apoptosis, the others posit that this result supports a neuroprotective role.

Other genes

Using structural MRI derived quantitative traits derived from Caucasian subjects from ADNI, Shen, et. al. reported genetic associations with SNPs located near *EPHA4*, *TP63* and *NXPH1* [74], and another group has shown an association with *EFNA5*, *CAND1*, *MAGI2*, *ARSB*, and *PRUNE2* [75]. These genes are involved in the regulation of protein degradation, apoptosis, neuronal loss and neurodevelopment. Thus, they have been identified as candidate genes associated with an increased risk of developing AD

Gene-Gene Interactions

Exploration beyond single gene association studies is necessary for complex diseases with complex etiologies and pathologies. This is just beginning to be explored, using quantitative traits derived from imaging modalities as the phenotype of interest. Previous gene-gene interaction studies using quantitative traits from brain images of patients with LOAD have implicated interactions between: *CR1* and *APOE*, and *GSK3B* and amyloid genes using quantified amyloid-based PET as the outcome variable [81,82], and calcium

signaling and axon guidance genes using quantified entorhinal and hippocampal volumes [83].

Gaps in Knowledge Addressed

Though PET has been approved for clinical detection of amyloid beta plaque pathology *in vivo*, since it involves radiation exposure, it is not ideal for routine screening or monitoring of patients, particularly before clinical symptoms are present. New biomarkers of amyloid beta pathology are needed and the exploration of the use of T1ρ MRI in humans *in vivo* is the next step to validate its use as a biomarker of this pathology. If T1ρ is validated as a proxy for amyloid beta deposition, it could easily be implemented to monitor disease progress or classify patients in research and clinical trials. Thus, the first goal of this research is to analyze the utility of T1ρ MRI in human adults with DS, who have a high probability of amyloid beta deposition compared to adults in the general population.

Further, we will explore the "accelerated brain aging" hypothesis in DS patients put forward by Beacher, et.al. [40]. We will analyze region of interest volume using T1-weighted structural MR images in subjects with DS and compare age-related changes in these measurements to those in normal control subjects and also in subjects with another neurodevelopmental disorder (Williams Syndrome) to further explore this hypothesis. With the quantified T1-weighted images, we will extract meaningful endophenotypes to evaluate the relationship between both *APOE* status and dementia status as measured by neuropsychological tests and each of these endophenotypes.

The final goal of this research is to employ imaging genetics techniques in the large, publicly available ADNI dataset to tease apart the genetic etiology of the amyloid and

neuro-atrophy pathologies of LOAD. As described above, the etiology of LOAD still eludes us despite its prevalence and considerable research efforts devoted to it. We will employ an innovative strategy to address two major challenges in LOAD research: (1) clinical heterogeneity and (2) biological interactions by using PET and MRI derived quantitative endophenotypes to dissect clinical heterogeneity, and by directly investigating gene-gene interactions for their association with these endophenotypes.

Chapter 2

VALIDATION OF T1P MAGNETIC RESONANCE IMAGING IN HUMAN ADULTS WITH AMYLOID BETA PLAQUE DEPOSITION

Introduction

Positron Emission Tomography (PET) has been approved for clinical detection of amyloid beta plaque pathology *in vivo* but because it involves radiation exposure, it is not ideal for routine screening or monitoring of patients, particularly before clinical symptoms are present. New non-invasive biomarkers of amyloid beta plaque pathology are needed.

T1ρ-weighted Magnetic Resonance Imaging (MRI) is an MR sequence that has been validated to detect amyloid beta plaque *in vivo* in a mouse model of AD [59] (Figure 1), but has not yet been validated in humans. In this sequence, instead of allowing transverse magnetization (M_{xy}) to relax undisturbed, a low frequency radio-frequency pulse (RF) is applied in the transverse plane for a relatively long period of time, “locking” the spins in the orientation of the RF, hence the names of the RF frequency and the duration of its application: spin-lock frequency (FSL), and spin-lock time (TSL), respectively [84]. This RF pulse slows de-phasing and prolongs the decay of magnetization, allowing the transverse magnetization to interact with lattice processes occurring at the low frequency of the RF. Therefore, T1ρ is sensitive to slow motions with low frequencies, and T1ρ will decrease (i.e. protons will relax faster) around lattice processes moving at these low frequencies [60,85]. Healthy brain tissue allows for more free motion of water than the diseased brain which is overrun with large protein based amyloid beta plaques [60]. This

high protein content hinders water motion such that theoretically, in the diseased brain, T1ρ will be shorter than healthy brain tissue's T1ρ times [60].

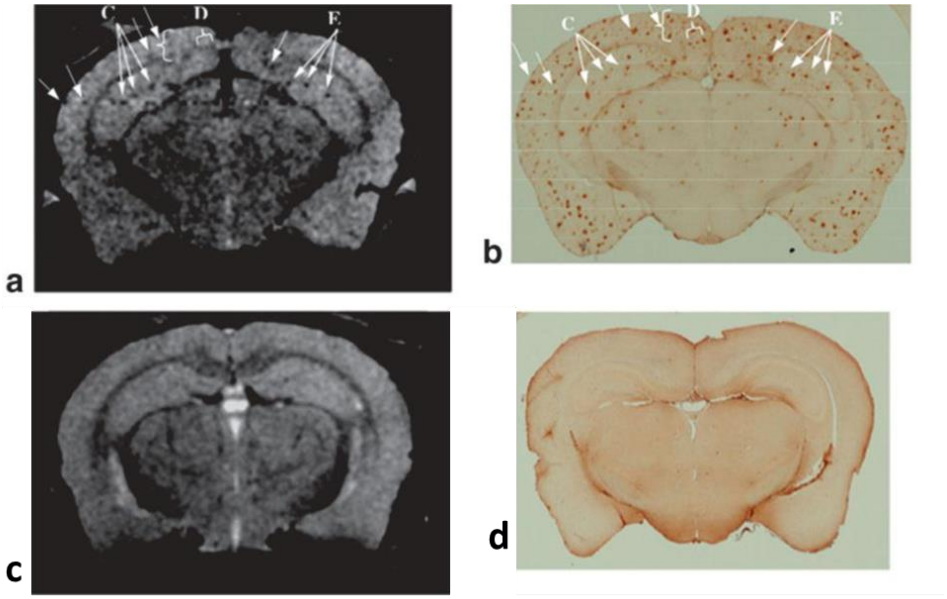

Figure 1: T1ρ-weighted MRI validated in a mouse model of Alzheimer's Disease.

Adapted from Borthakur, et. al. (2006) [59]. T1ρ MRI in a mouse model of Alzheimer's Disease (APP/PS1 mouse) (a) and in a control mouse (c). Corresponding histologic images immunostained for amyloid beta deposits in the APP/PS1 mouse (b) and in the control mouse (d). The hypointensities in the T1ρ images align with the immunostained amyloid beta in the APP/PS1 mouse, but are absent in the control mouse.

In a mouse model of AD (*APP/PSEN1* transgenic mouse), amyloid beta plaques were detectable as hypointensities on the T1ρ-weighted MR images in the AD-related cortical and hippocampal regions, which corresponded to shortened T1ρ at the amyloid beta plaques and agreed with the theory outlined above (Figure 1) [59]. Hypointensities in the thalamic/hypothalamic regions also are detected on MRI as seen in Figure 1 but there were no stained amyloid plaques in these regions and the authors did not comment on

this discrepancy. T1ρ could be detecting other low frequency proteins or molecules in this region. Very high resolution images were acquired (78 µm x 78 µm x 130 µm) on these mice and required the mice to be anesthetized and to be scanned for three hours. After MRI acquisition, the mice were sacrificed, and the brains were immunohistochemically stained for amyloid beta plaque. The stained brain slices were aligned with the MRI slices to compare the exact location of the stained plaque and the hypointensities on MRI. There was general congruency between the stained and MR slices, validating the ability of T1ρ MRI to pick up an amyloid beta plaque *in vivo* [59]. Extension of this validation to humans is necessary for this MR sequence.

In humans, T1ρ MRI has been used in patients with breast cancer, gliomas, cartilage degeneration, Parkinson's Disease, and AD [86–89]. In relation to AD, T1ρ MRI has been quantified in patients with AD, MCI, and age matched normal controls, but unlike in the mouse studies, T1ρ *increased* in human subjects with MCI and AD (Figure 2) [89–92]. This is opposite of what is expected theoretically in subjects with increased amyloid beta load and opposite of what was observed in the mouse model study [89–92]. This reversal was attributed to T1ρ detecting increased extracellular space caused by late stage disease related neuronal loss which typically accompanies diagnoses of MCI and AD [89–92]. Therefore, T1ρ is not validated in humans as of yet. We aimed to avoid the problems encountered in this prior human study by attempting to validate T1ρ in subjects adults with DS *without dementia* who have a high probability of having amyloid beta plaque load prior to neuronal cell loss, since amyloid beta plaques are expected to deposit prior to neuronal cell death [93].

Further, in each of the prior studies of T1ρ in humans, T1ρ was quantified using one FSL (500 Hz) on a 1.5 Tesla (1.5 T) MRI scanner. We were interested in quantifying T1ρ across multiple FSLs using a higher field strength scanner, i.e. 3 Tesla (3 T), in order to

quantify the T1ρ dispersion curve at higher resolution [84]. The dispersion curve can characterize the macromolecular make-up of a tissue, and in human brain, the dispersion curve has only been quantified in normal subjects [84].

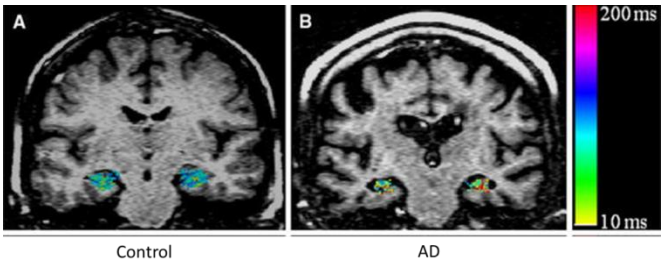

Figure 2: T1ρ- weighted MRI maps in human subjects with Alzheimer's Disease. Adapted from Haris, et. al. (2009) [91]. T1ρ was measured in (A) control and (B) late onset AD (LOAD) subjects in the hippocampus at 1.5 Tesla (1.5 T). Higher values are seen in the LOAD subjects compared to the control subjects, and this may be due to the detection of increased extra-cellular space caused by disease related neurodegeneration, instead of plaque burden.

Methods and Materials

Subjects

Data from 38 subjects recruited via community-based recruitment and collaborations with Vanderbilt clinicians has been analyzed. Subjects are classified as normal cognition (NC) or Down Syndrome (DS) based on prior clinical diagnosis and physical manifestations (Table 1). Adults with DS and NCs were recruited using flyers and website postings with IRB-approved language targeting adults over 18 years of age.

Because of the early onset of amyloid pathology in subjects with DS, the DS subjects were much younger than the NC subjects. However, all DS subjects were over 18 years of age. For adults with DS, we further recruited from local and regional educational centers for individuals with intellectual disabilities, community based living centers, caregiver support groups, and employment assistance programs. Diagnosis of normal cognition in the general population cohort is based on a battery of cognitive tests administered by a qualified masters-level neuropsychologist. A similar cognitive testing battery is also administered to the DS subjects. The cognitive tests applied to these subjects quantify cognitive impairment, memory, learning, vocabulary, attention, task speed, and comprehension. Participants with NC and the caretakers of the subjects with DS were also asked about the presence of first degree family history of AD. Participants are free to take as many breaks as needed to avoid exhaustion.

Table 1 Demographics for community-based recruitment.

DS = Down Syndrome. NC = Normal Cognition. N = number of subjects. Age = average age of group. CA = Caucasian.

	DS	**NC**
N	16	22
Age	43	68
Race (# not CA)	0	6
%Female	43.75%	81.82%
# *APOE* e4 carriers	4	5
# e2 *APOE* carriers	2	2

All participants with DS exhibited the physical, cognitive and behavioral profile of DS, and they previously had received a clinical diagnosis of the disease. NC subjects are over 65 years of age to avoid subjects with early onset AD. The DS subjects are all over 18 years of age because of the early onset of amyloid pathology in subjects with DS. Subjects recruited from the general population and caregivers of individuals with DS gave informed consent, while participants with DS gave assent, for this study which included MR imaging, genotyping, and cognitive testing. All study procedures were approved by the Vanderbilt University Institutional Review Board. As per this protocol, two subjects with incidental findings had their MRIs reviewed by a neuro-radiologist who determined if the patient should be contacted for clinical follow-up.

MRI

Adults participated in an magnetic resonance imaging (MRI) scan in a Philips Achieva 3-Tesla scanner (Philips Medical Systems, Inc., Best, Netherlands) using an eight-channel SENSE head coil, housed in the Vanderbilt University Institute of Imaging Science (Nashville, TN).

T1

Full brain, high-resolution T1-weighted Turbo Field-Echo pulse sequences were acquired with the following parameters: Echo Time/Repetition Time (TE/TR) = 4.6 ms / 9 ms, shot interval/inversion time (TS/TI) = 1166.401 ms / 402.8176 ms, slice thickness = 1 mm, slices = 150, in-plane voxel size = 1 mm x 1 mm, field of view (FOV) = 25.6 cm x 25.6 cm x 15 cm.

T1ρ

Fluid-attenuated T1ρ pre-encoded Turbo Spin-Echo pulse sequences were acquired, modeled after the 1.5 T sequence used in the previous T1ρ human studies [89]. Six T1ρ images were acquired after application of three different FSLs (0, 275 and 550 Hz) both at two different TSLs (20 and 80 ms). All six T1ρ images were acquired with these parameters: TE/TR = 15 ms / 2700 ms, slice thickness = 5 mm, slices = 12, in-plane voxel size = 2.5 mm x 2.5 mm, FOV = 20.5 cm x 20.5 cm x 6.0 cm with coverage of key temporal, parietal, and frontal regions affected in AD Figure 3).

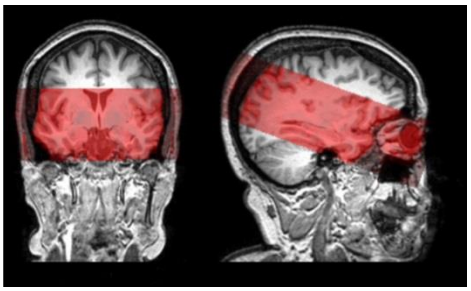

Figure 3: Example of image acquisition for T1ρ validation study.

The T1ρ acquisition area is overlaid in red on a T1-weighted image of an example subject. Key structures such as frontal, temporal, and parietal regions, and hippocampus are covered by the T1ρ scan.

Imaging Analysis

Quality Control

The raw T1- and T1ρ-weighted images were visually inspected for any artifacts and subjects were discarded if significant artifact was present in any one of the images. Of the 38 subjects analyzed, only 17 have T1- and T1ρ-weighted images that pass quality control (8 DS, 9 NC). Most of the scans were discarded because of ringing artifacts in the T1ρ images caused by use of the incorrect “patch” placed on the scanner before MRI acquisition. Salvaging the discarded datasets was discussed with VUIIS faculty, and they recommended removing the slices of the image that had these artifacts while keeping the unaffected slices. After re-visualization of these images, we determined that when an image was acquired under the incorrect patch, all slices were affected and had ringing artifacts, rendering the entire scan un-usable in these analyses. The subjects with NC were further classified by the presence or absence of a family history (at-risk (AR) based on a positive first degree family history of AD and NC, respectively). Demographics for these subjects can be found in Table 2.

Table 2 Demographics for subjects with T1ρ analyzed.

DS = Down Syndrome. NC = Normal Cognition. N = number of subjects. Age = average age of group. CA = Caucasian.

	DS	**AR**	**NC**
N	8	3	6
Age	47	65	65
Race (# not CA)	0	1	2
%Female	62.50%	100.00%	66.67%
# *APOE* e4 carriers	2	2	1
# *APOE* e2 carriers	0	0	1

T1ρ Region of Interest-based analysis

After visual inspection of the 3D T1-weighted images, to parcellate the brain into cortical and subcortical tissue classes and derive quantitative estimates of brain volume, we used an automated, non-biased atlas-based Bayesian segmentation procedure, applied in FreeSurfer v.5.0 (http://surfer.nmr.mgh.harvard.edu/) [94]. FreeSurfer preprocessing for volumetric T1-weighted images included: motion correction, brain extraction and removal of non-brain tissue using a hybrid watershed/surface deformation procedure [95]; automated spatial transformation and white matter segmentation of subcortical volumetric structures [96]; intensity normalization, tessellation of gray matter/white matter

boundary and automated topology correction [97]; and surface deformation following intensity gradients to optimally place gray matter/white matter and gray matter/cerebrospinal fluid borders at the location where the greatest shift in intensity defines the transition to the other tissue class [94]. Image outputs from each stage of FreeSurfer processing were visually inspected. Only images that passed quality control were used. Quantitative estimates of volume were derived in a large set of spatially distinct region of interests (ROIs) that covered the entire brain, as specified in the Desikan-Killiany Atlas [98]. This atlas includes parcellations of gray and white matter and segmentations of subcortical gray matter, and also includes summary volumes (i.e. total cortex volume). This segmentation is robust to anatomical variability of neurological diseases and aging, including ventricular enlargement, which was important in this study[99].

The six T1ρ scans (taken at TSL= 20 and 80 ms with FSL= 0, 275 and 550 Hz) for each subject were aligned to the T1ρ scan acquired at TSL=20 ms and FSL=275 Hz [T1ρ20, 275]. For each FSL, voxel-wise T1ρ maps for each subject were generated by solving in MATLAB (http://www.mathworks.com/products/MATLAB/) the equation

$$S(TSL) = S_o e^{-TSL/T1\rho} \quad \text{..... (1)}$$

which describes T1ρ (Figure 4) [100]. *S(TSL)* is the signal intensity as a function of TSL, and S_o is the baseline signal intensity. Since multiple TSLs were used, the natural logarithm of each voxel's signal intensity was fit as a function of the TSL using a linear least-square algorithm in SPM8 (www.fil.ion.ucl.ac.uk/spm/) (Figure 4). The resulting slopes of the linear fitted line were negated and inverted to derive T1ρ and negated to derive R1ρ. This analysis yielded voxel-wise T1ρ and R1ρ quantitative maps scaled in milliseconds and 1/milliseconds, respectively, for each FSL.

The automatically generated ROI labels from FreeSurfer were aligned to the original T1-weighted image. Next, the high resolution T1-weighted image and the ROI label aligned to it were co-registered to the lower resolution T1ρ20, 275 to reduce interpolation artifacts that occur when registering a lower resolution image to a higher resolution image. The ROI labels were then in the same spatial configuration as the R1ρ quantitative maps. The ROI labels were applied to these maps for each FSL and the mean R1ρ value for each ROI at each FSL was extracted using FreeSurfer. These values were then plotted versus FSL in R (http://www.r-project.org/) to create dispersion curve plots for each subject for each ROI. Subjects who had less than 95% of an ROI covered, as determined by comparing the volume of each ROI covered by the T1ρ image with the volume of the ROI covered by the T1 image, had that ROI dropped to keep 0-value voxels not covered by the T1ρ-weighted MRI from skewing the ROI average.

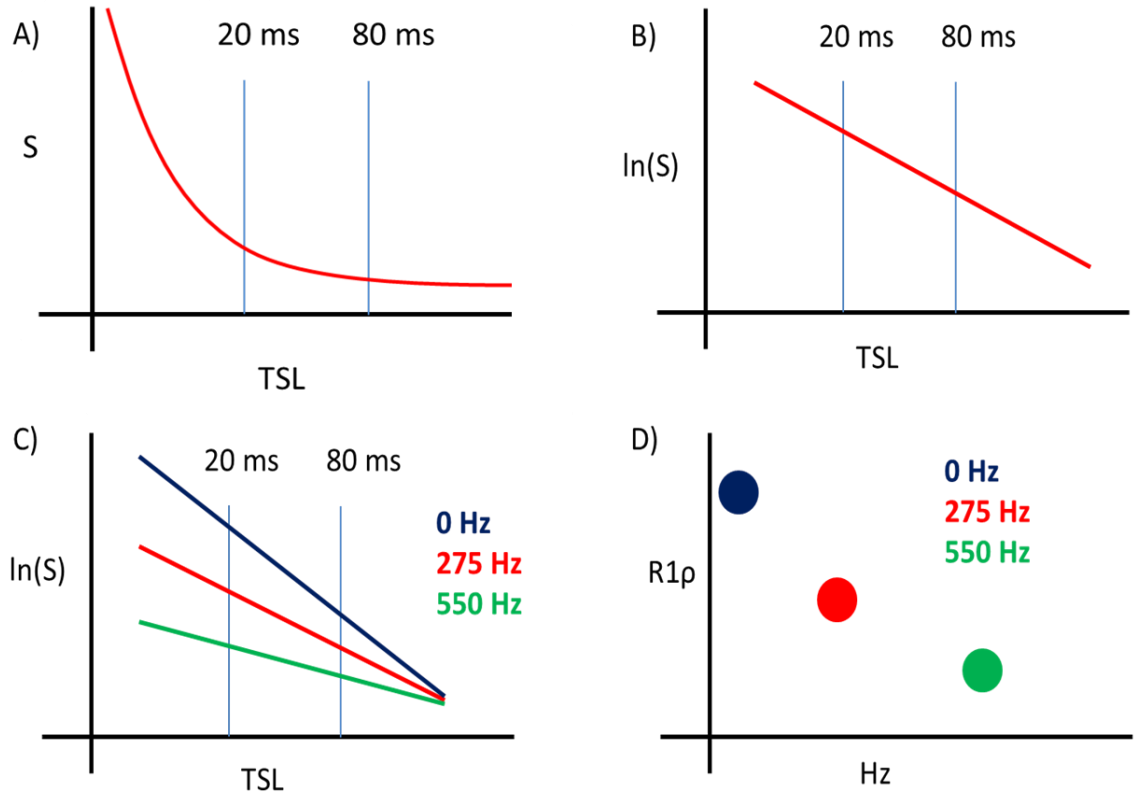

Figure 4: Quantification of T1ρ weighted MRI and the T1ρ dispersion curve

(A) T1ρ is collected at TSLs of 20 and 80 ms.
(B) The natural logarithm of each voxel's intensity is linearly fitted as a function of these TSLs and by solving Equation 1.
(C) (A) and (B) are repeated for each FSL (0, 275, and 550 Hz). The slopes of the linearly fitted lines are negated and inverted and negated to derive T1ρ and R1ρ, respectively, for each FSL.
(D) The dispersion curve consists of the quantified R1ρ (1/ T1ρ) values at 0, 275 and 550 Hz plotted as a function of FSL.

We used an image subtraction method to derive a contrast (exchange rate contrast,

ERC) based upon the features of the dispersion curves, where

$$ERC = 4 * \frac{(R1\rho(FSL{=}0) - R1\rho(FSL{=}275))(R1\rho(FSL{=}275) - R1\rho(FSL{=}550))}{(R1\rho(FSL{=}0) - R1\rho(FSL{=}550))^2} \quad \text{..... (2)}$$

(Figure 5) [101]. The ERC characterizes the frequency at which maximum inflection in the T1ρ dispersion curve occurs. The average ERC for each ROI for all subjects was calculated and the group mean differences were analyzed for significant differences.

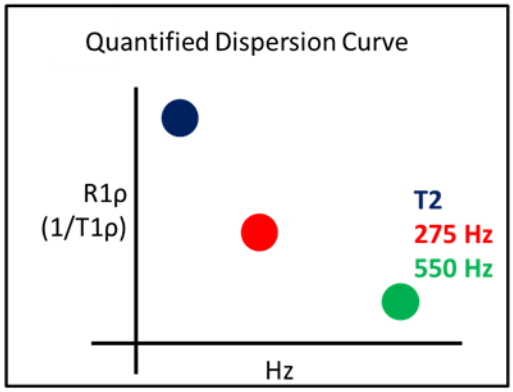

$$ERC = 4 * \frac{(R1\rho(FSL = 0) - R1\rho(FSL = 275))(R1\rho(FSL = 275) - R1\rho(FSL = 550))}{(R1\rho(FSL = 0) - R1\rho(FSL = 550))^2}$$

Figure 5: Exchange rate contrast (ERC) equation and calculation for the T1ρ validation study

T1ρ Voxel-based analyses

T1ρ was also analyzed at the voxel-wise level. For a voxel-wise analysis, all images have to be in the same space, and must be co-registered to a template space, which is a disadvantage of this method compared to the ROI based method described previously. In exchange, the voxel-wise method allows for voxel-wise differences to be detected, as opposed to having to average voxels across an entire ROI as necessary in FreeSurfer. As in the ROI based method, the T1ρ-weighted images were all aligned to T1ρ20, 275. These realigned images were then normalized to standard Montreal Neurological

Institute (MNI) template space, using the Normalize (Estimate + Write) function with the T1-weighted image as the source image. As above, for each FSL, voxel-wise T1ρ maps for each subject were generated by solving Equation 1 in MATLAB. A voxel based analysis was performed on the resulting quantitative T1ρ maps at 0, 275, and 550 Hz using a one-way ANOVA comparing DS vs. AR, DS vs. NC and AR vs. NC, using a combination of two very liberal thresholds: $p < 0.05$ and an extent threshold of 1 voxel.

Pipeline

An automatic pipeline was designed, tested, and implemented to analyze the T1-weighted and T1ρ-weighted MR images after manual inspection for both the ROI- and voxel-based analyses. The code for the entire pipeline can be found in Appendix A. Equation 1 was solved via MATLAB scripts provided to us by faculty in the VUIIS and code in SPM8 and FreeSurfer was created to complete the analysis pipeline. A Python script was created to automatically pull the images from VUIIS to our own servers. This entire pipeline is implemented in MATLAB and Unix environments and uses FreeSurfer to automatically segment and parcellate the T1-weighted images, align and co-register the T1- and T1ρ-weighted images, calculate the T1ρ and R1ρ statistical parametric maps, and pull information from these maps so that the dispersion curves can be plotted for each subject for each region of interest (Figure 6) and the voxel-wise analysis (Figure 7) can be run. An overview of both pipelines can be seen in Figure 8. All code for these pipelines can be found in Appendix A.

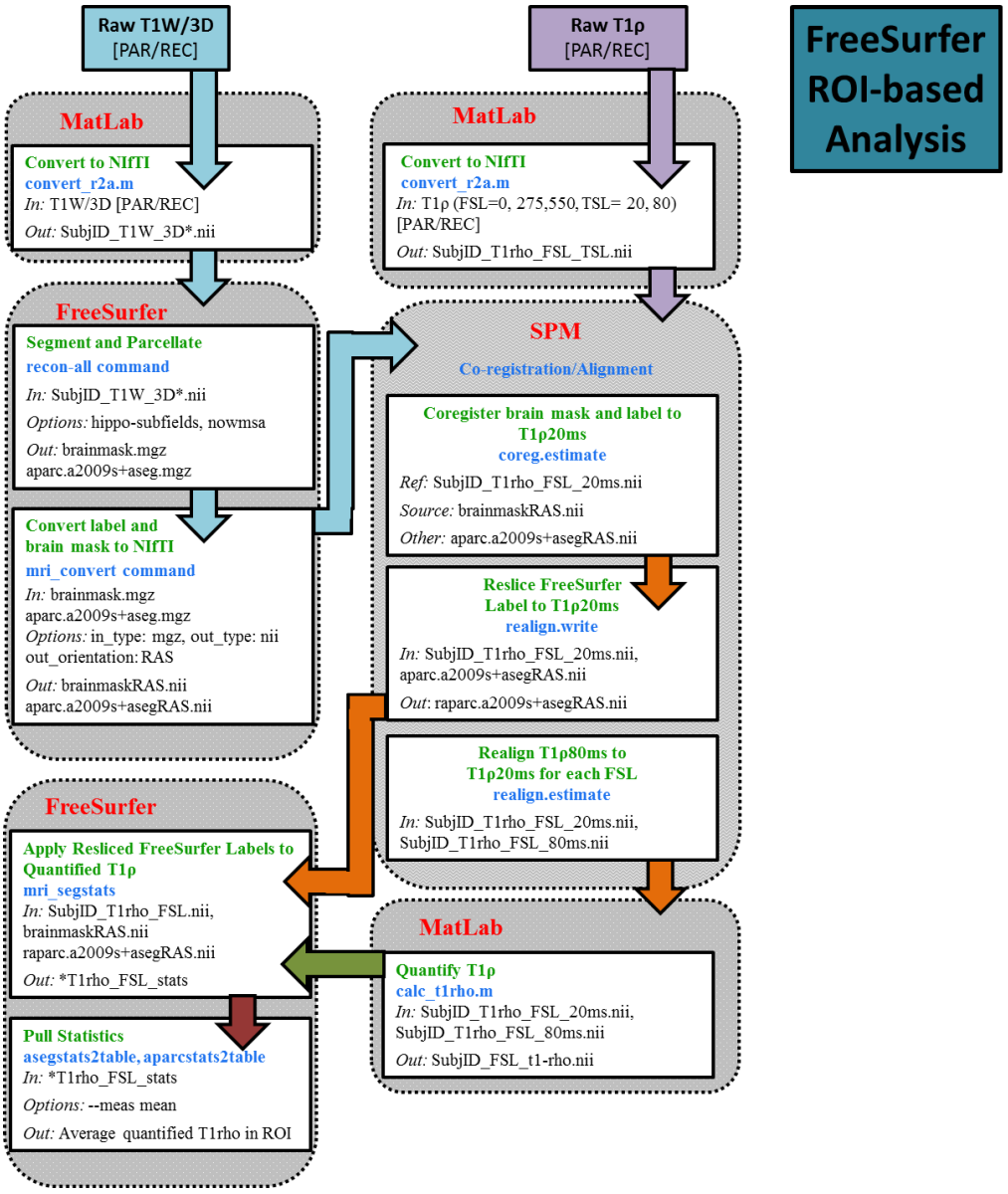

Figure 6: Region of interest (ROI) based analysis pipeline using FreeSurfer ROI parcellation and segmentation for the T1ρ validation study

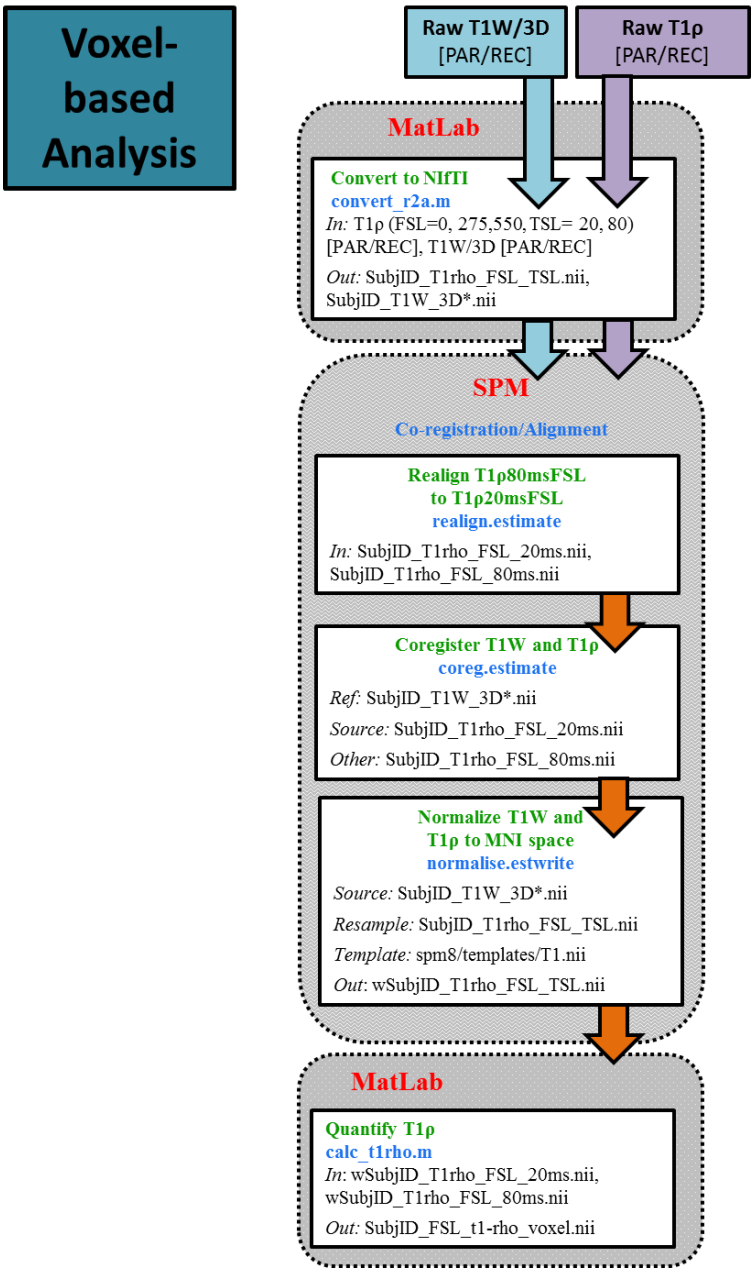

Figure 7: Voxel-based analysis pipeline for the T1ρ validation study

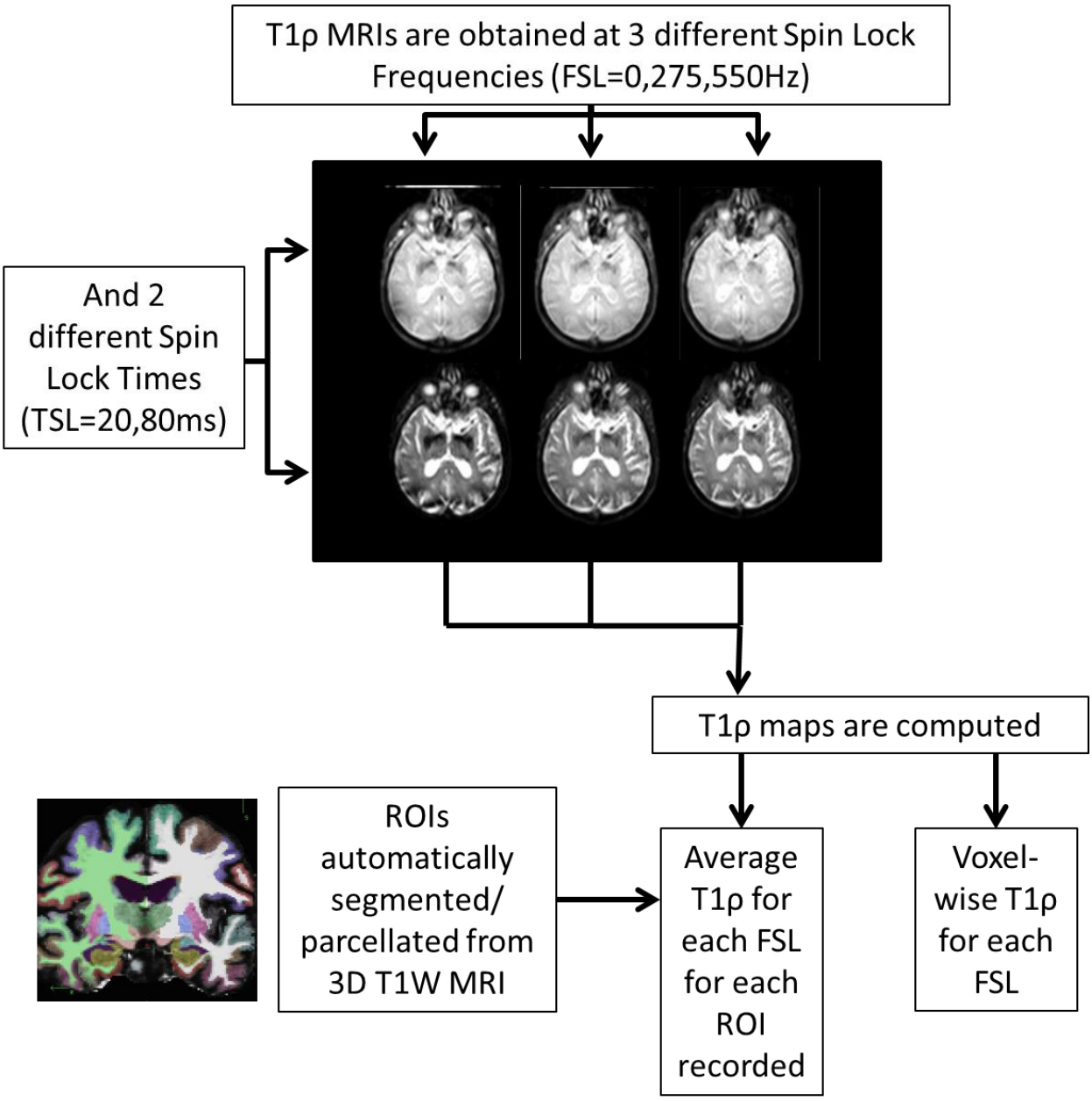

Figure 8: Overview of both region of interest (ROI) and voxel-based pipelines for the T1ρ validation study

Results

Example T1ρ maps determined by solving Equation 1 (Figure 4) for example DS, NC, and AR subjects can been seen in Figure 9. In any of the ROIs tested (Table 3), there were no differences between the groups when analyzing dispersion curve slope (Figure 10) nor when comparing ERC across group in any ROI (Figure 11). For the purpose of this manuscript, as an example, we will display results from the left hippocampus. In the voxel-wise analysis, no voxels were significantly different between the two groups using very liberal thresholds of extent = 1 voxel and $p < 0.05$.

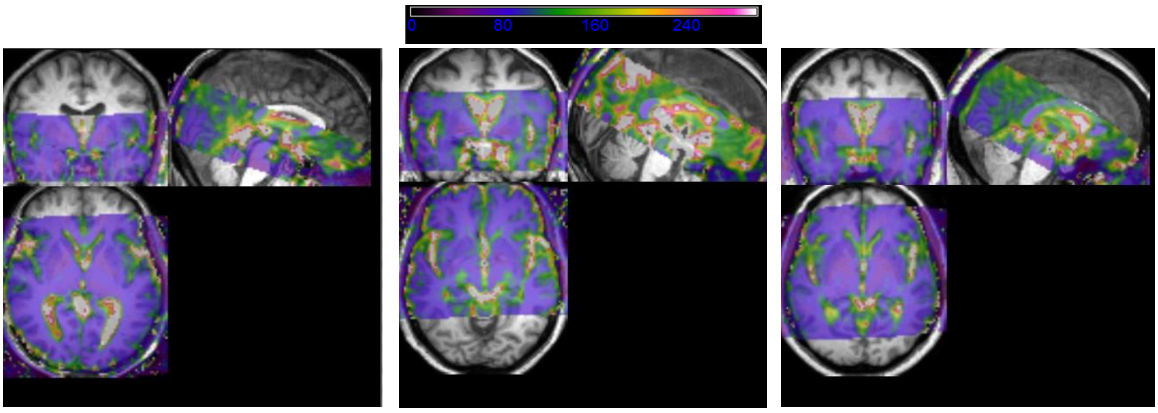

Figure 9: Example calculated T1ρ maps for human subjects.

Cross-sections of one DS, AR, and NC (left to right) subject. T1ρ maps (550 Hz) are overlayed on T1-weighted images.

Table 3 Regions of interest (ROIs) tested in T1ρ validation analysis.

ROIs		
CC_Anterior	ctx-lh-precuneus	ctx-rh-pericalcarine
CC_Central	ctx-lh-rostralanteriorcingulate	ctx-rh-postcentral
CC_Mid_Anterior	ctx-lh-superiorparietal	ctx-rh-posteriorcingulate
CC_Mid_Posterior	ctx-lh-superiortemporal	ctx-rh-precuneus
CC_Posterior	ctx-lh-supramarginal	ctx-rh-rostralanteriorcingulate
ctx-lh-bankssts	ctx-lh-temporalpole	ctx-rh-superiorparietal
ctx-lh-cuneus	ctx-lh-transversetemporal	ctx-rh-superiortemporal
ctx-lh-entorhinal	ctx-rh-bankssts	ctx-rh-supramarginal
ctx-lh-frontalpole	ctx-rh-cuneus	ctx-rh-temporalpole
ctx-lh-fusiform	ctx-rh-entorhinal	ctx-rh-transversetemporal
ctx-lh-inferiorparietal	ctx-rh-frontalpole	Left-Accumbens-area
ctx-lh-inferiortemporal	ctx-rh-fusiform	Left-Amygdala
ctx-lh-insula	ctx-rh-inferiorparietal	Left-Caudate
ctx-lh-isthmuscingulate	ctx-rh-inferiortemporal	Left-Hippocampus
ctx-lh-lateraloccipital	ctx-rh-insula	Left-Pallidum
ctx-lh-lateralorbitofrontal	ctx-rh-isthmuscingulate	Left-Putamen
ctx-lh-lingual	ctx-rh-lateraloccipital	Left-Thalamus-Proper
ctx-lh-medialorbitofrontal	ctx-rh-lateralorbitofrontal	Left-VentralDC
ctx-lh-middletemporal	ctx-rh-lingual	Right-Accumbens-area
ctx-lh-parahippocampal	ctx-rh-medialorbitofrontal	Right-Amygdala
ctx-lh-parsopercularis	ctx-rh-middletemporal	Right-Caudate
ctx-lh-parsorbitalis	ctx-rh-parahippocampal	Right-Hippocampus
ctx-lh-parstriangularis	ctx-rh-parsopercularis	Right-Pallidum
ctx-lh-pericalcarine	ctx-rh-parsorbitalis	Right-Putamen
ctx-lh-postcentral	ctx-rh-parstriangularis	Right-Thalamus-Proper
ctx-lh-posteriorcingulate		Right-VentralDC

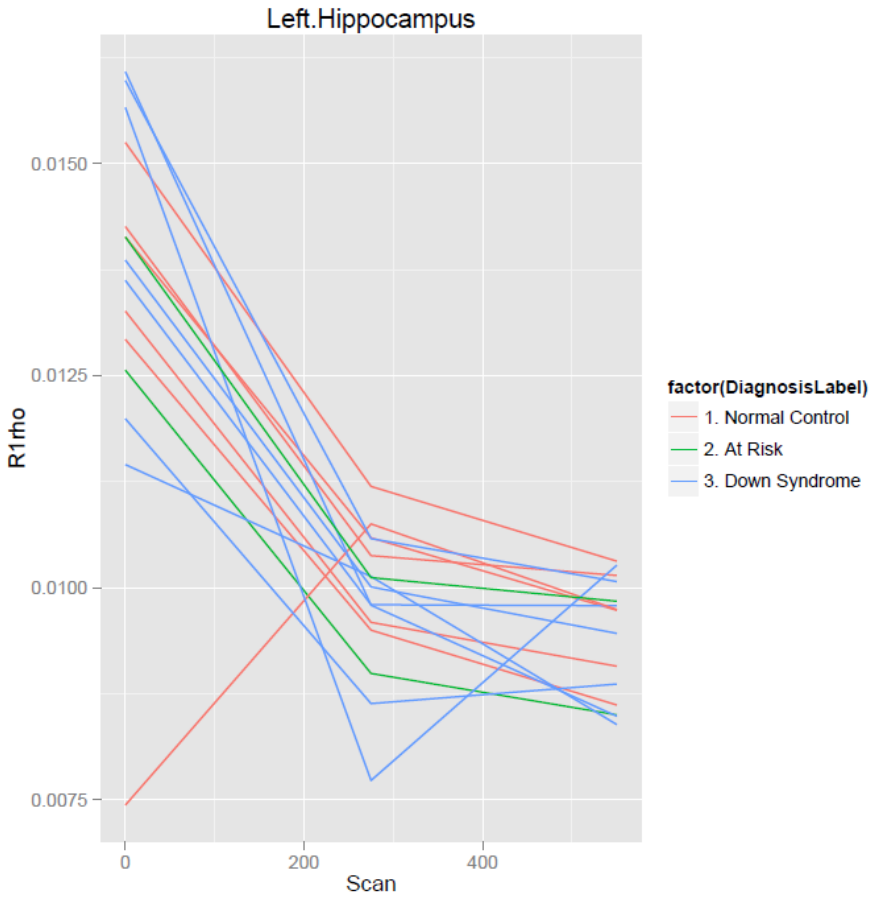

Figure 10: Example of quantified T1ρ dispersion curves plotted in human subjects.

The dispersion curves are plotted for each subject's left hippocampus, plotting average R1ρ versus spin lock frequency (FSL=0, 275, 550 Hz). Subject group for each subject is indicated by line color (red: normal control, green: at risk, blue: Down Syndrome).

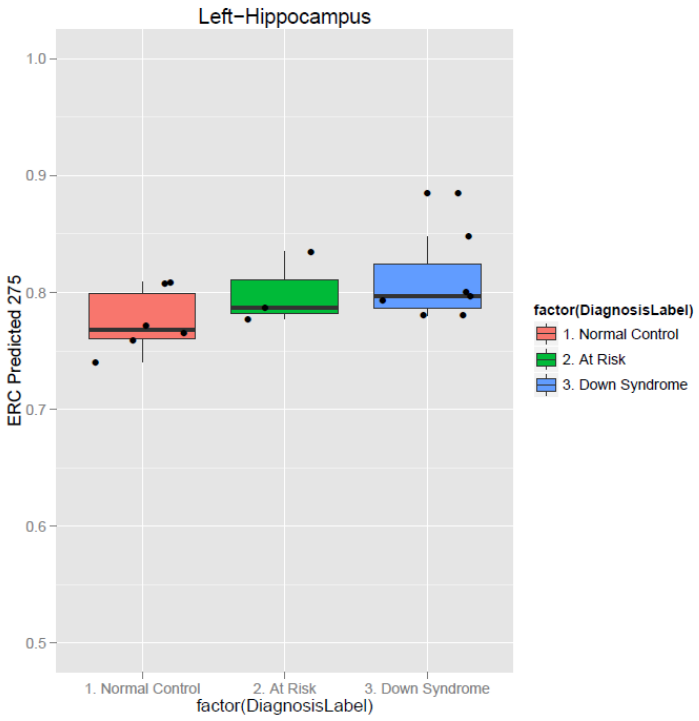

Figure 11: Example of quantified exchange rate contrast (ERC) values of the left hippocampus plotted within groups.

Discussion

In Figure 9 no apparent differences are visually detected between scans of subjects with DS and those who are AR or NC. Because of the size of the voxels in this study, this is not indicative of negative results, and further analyses were necessary. The dispersion curves were quantified for each subject. The quantified dispersion curves (Figure 10) generally fit what was theoretically expected (Figure 4), with R1ρ at 0 Hz greater than R1ρ at 275 Hz, which was greater than R1ρ at 550 Hz. There are outlier subjects whose dispersion curves do not follow this trend. Interestingly, when removal of these scans was performed and this trend was discovered, we found that this trend did not occur for

all of the ROIs in one subject, but instead, this occurred across multiple subjects in differing ROIs. The deviations from expectations in the dispersion curves presented here are most likely due to subtle movement artifacts that were not detected upon visual inspection of each image, and in the continuation of this study, as the total number of subjects increases over time, subjects whose dispersion curves do not follow this trend can be removed from the analysis, or each individual scan that does not follow the trend can be removed. Further analysis of these dispersion curves was completed, with computation of ERC values. The theoretical trend for ERC values has not been established, and discussion with faculty at the VUIIS is ongoing regarding this topic. Therefore, in Figure 11, an interesting trend may be forming (two sampled t-test comparing NC to DS group: $t = 1.0631$, $p = 0.3105$), but in order to definitively draw a conclusion, the sample size for each group must increase to inform this discussion.

These negative and inconclusive results are not necessarily indicative of failure of T1ρ to detect amyloid beta plaque in humans, though it is indicative of the failure to validate the approach in humans in this study's sample population.

There are many potential reasons for these negative results, which leads to future directions for this project. First, when computing T1ρ from the slope of the natural logarithm of signal as a function of TSL, we were not be able to rule out voxels based on r^2 value because we only had two TSL values. This would have eliminated voxels that are outliers, perhaps due to partial volume effects. Therefore in the future, using more than two TSL values in image acquisition would allow for further quality control of the images and their quantification. The voxel size of the images acquired on our human subjects may have been too large to detect the effects of amyloid beta plaque, as the voxels were over four orders of magnitude larger than those seen in the successful mouse model study. In the future, this sequence could be validated on an autopsy brain

of a patient with clinically diagnosed AD or an elderly individual with DS. A high resolution image could be acquired, as these brains can be scanned for hours. These brains could then be immunohistochemically stained for amyloid beta plaque to compare to the MR images acquired, mimicking the study performed in the mouse model [59]. In this study, if hypointensities were seen on the T1ρ images of the autopsy brain which aligned with the immunohistochemically stained brain slices, this could be repeated in control subjects to control for false positive hypointensities. To continue this validation, high-resolution T1ρ images could be acquired on live patients who most likely have plaque (elderly DS or AD patients). In these patients, since brain samples are not practical, this could be validated with amyloid PET imaging. Alternatively, these patients could be recruited from hospice care, as was done in previous PET validation studies [55]. In this study design, T1ρ MRI could be acquired on patients who physicians consider nearing the end of life. After death, the brains of these patients would be donated to research, and could be immunohistochemically stained for amyloid beta plaque and these stained images and the MR images could be compared as described previously.

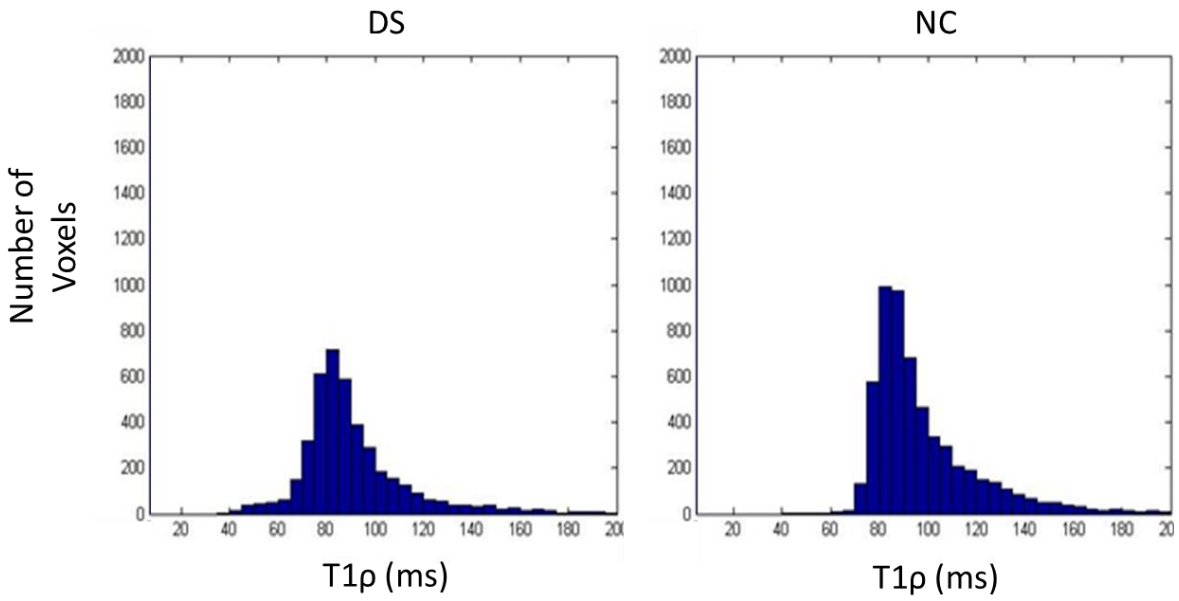

Figure 12: Representative histograms of the T1ρ values in AD-related regions of interest. Histograms for the inferior parietal lobe for one Down Syndrome (DS) subject (left) and one Normal Control (NC) subject (right) are presented. The x-axis here is T1ρ value in milliseconds (ms) and the y-axis is the number of voxels at this value within a given ROI.

The voxel-wise T1ρ maps may still hold important information, even with these relatively large voxel sizes. In the ROI-based method the true signal originating from amyloid beta plaques may be drowned out by the surrounding normal tissue when taking the mean value of an entire ROI. To ameliorate this, we turned to a voxel based approach, but this approach may also have been flawed: in theory, we do not expect each individual to have amyloid beta plaques at the exact same voxel locations. Therefore, instead of looking at differences between each voxel, the *distribution*, including kurtosis and skewness, of T1ρ values within each ROI in the groups should be investigated, using the histogram function in MATLAB (see Appendix A for example code). This has been explored in two sample subjects, but is being extended to the entire cohort (Figure 12). In future analyses, the differences between the groups' distributions can be tested with a two-sample Kolmogorov-Smirnov test.

In conclusion, though these results did not validate T1ρ in human subjects, they are not necessarily indicative of the failure of T1ρ to detect amyloid beta plaque in general. The T1ρ sequence should be pursued as an alternative strategy to PET detection of amyloid beta plaque with the changes in sequence parameters and/or methodology as explained above.

Chapter 3

DIFFERENCES IN AGE-RELATED EFFECTS ON BRAIN VOLUME IN DOWN SYNDROME AS COMPARED TO WILLIAMS SYNDROME AND TYPICAL DEVELOPMENT

Introduction

It has been suggested that individuals with Down Syndrome (DS) experience accelerated brain aging as evidenced by significant age-related reduction in brain volume, but to date, it is not known whether this is an effect of neurotoxic pathology evident in DS or a pre-existing feature of impaired neurodevelopment [40]. In the current study, we aimed to dissociate the contribution of neurodevelopment versus neurodegeneration in regional brain volume in DS. We compared a wide age range of adults with DS to adults with a second neurodevelopmental disorder, Williams Syndrome (WS), and we also compared both neurodevelopmental disorders to a typically developing (TD) control group.

Etiology and Presentation of Down Syndrome and Williams Syndrome

DS is a neurodevelopmental disorder caused by the presence of three copies of chromosome 21 (trisomy 21). It occurs in one in every 691 live births in the US [18] and is the most common genetic cause of intellectual disability [19,20]. The degree of cognitive impairment associated with DS ranges from mild to severe, with the mean IQ of 50, or

moderate intellectual disability [20]. Individuals with DS exhibit deficits in language, verbal short term-memory, and explicit long-term memory; whereas visuospatial short-term memory, associative learning, and implicit memory are relatively preserved [21]. Advances in the treatment of medical comorbidities, such as heart defects and digestive malformations, have resulted in dramatic improvements in life expectancy for individuals with DS living in the U.S., rising from 9 years in the early-twentieth century [22] to nearly 60 years in 2010 [102]. Although individuals with DS present with a unique cognitive and behavioral profile, they do share some basic characteristics with individuals who have Williams Syndrome.

Williams Syndrome (WS) is a neurodevelopmental disorder caused by the hemizygous deletion of 26-28 genes on chromosome 7 [103]. The prevalence of WS is one in every 7,500 live births [104]. As with DS, WS is associated with cognitive impairment. The average IQ for individuals with WS is approximately 50-60, indicating mild to moderate intellectual disability [105,106]. The WS cognitive profile is characterized by deficits in visuospatial and implicit memory and strengths in language, verbal short-term memory, face and object recognition, and music processing skills [107–111]. In addition, individuals with WS often demonstrate increased non-social anxiety and phobias, paired with hyper-sociability and heightened empathy [112–114]. Similar to individuals with DS, persons with WS have experienced a significant increase in mean life expectancy following advances in treatment for medical comorbidities, particularly cardiac defects. There is very little literature on aging or life expectancy in WS, but there are documented cases of persons with WS who lived to be 70 years old [115].

Brain Morphometry in Down Syndrome and Williams Syndrome

On average, children and young adults with DS or WS have an overall smaller brain volume compared to TD individuals of similar age [116]; however the specific brain areas that show significant volumetric differences compared to TD are distinct for each of the neurodevelopmental disorders. Individuals with DS tend to have smaller frontal, amygdalar, and cerebellar volumes compared to TDs; whereas individuals with WS on average have smaller midbrain, thalamic, basal ganglia, and occipital and superior parietal lobe volumes compared to age-matched TDs [117,118]. It is important to also note that as a group, individuals with DS have an increase in parahippocampal volume and relatively preserved lenticular nuclei, basal ganglia, and occipital lobe volumes[20,21,119] while young adults with WS have relatively preserved frontal lobe, anterior cingulate, superior temporal gyrus, fusiform gyrus, amygdalar, and cerebellar volumes compared to TDs [21,117,119].

In addition to the pre-existing smaller volumes of frontal, amygdalar and cerebellar structures, non-demented older adults with DS (> 50 years of age) also have smaller whole prefrontal, posterior cingulate, hippocampal, and parahippocampal volumes when compared to age-matched TD adults [21]. Studies have shown that as individuals with DS age, they exhibit a similar pattern of neurodegeneration to that seen in the early stages of AD in the general population, in which the earliest neuropathological changes present in the medial-temporal lobe (MTL) and progress to neocortex and subcortical regions [39]. However, in individuals with DS these neuropathological changes happen at a much younger age compared to the general population, which has been attributed to accelerated brain aging [40].

At present, very few studies have assessed changes in brain morphology in older adults with WS [120]. One study showed an overall 15% smaller brain volume in individuals with WS compared to TD controls; however, they found no difference in the magnitude of this finding between older individuals with WS and a group of younger persons with WS, suggesting the effect might not be age-related [115].

Study Aims

The aims of the current study were to: (1) confirm previous findings of accelerated brain aging in DS versus TD, (2) document any age-related differences in brain volume seen in WS versus TD, and (3) test for age-related effects that are unique to DS. If accelerated brain aging seen in DS is primarily due to DS-specific neurodegenerative processes, then we would hypothesize that in the DS group, the age-related effects would be greater than those in the TD and WS groups. If, however, the accelerated brain aging is instead associated with a non-specific vulnerability due to atypical neurodevelopment, then we would hypothesize that both DS and WS groups would have greater age-related differences as compared to TD adults than they would compared to each other.

Methods

Study Participants

The current study included 14 Caucasian, DS adults (7 males; mean age 39.0; age range: 19-63), 58 WS adults (38 males; mean age 25.4, age range: 16-58), and 81 TD

adults (39 males; mean age 36.1, age range: 18-89.5). Demographic characteristics along with their corresponding statistical values are detailed in Table 4. Adults with DS or TD were recruited using flyers and website postings with IRB-approved language targeting adults over 18 years of age. For adults with DS, we further recruited from local and regional educational centers for individuals with intellectual disabilities, community based living centers, caregiver support groups, and employment assistance programs. Participants with WS were recruited through the annual Academy of Country Music Lifting Lives Music Camp, which is organized by the Vanderbilt Kennedy Center for Research on Human Development. All participants with WS or DS exhibited the physical, cognitive and behavioral profile of WS and DS, respectively, and they previously had received a clinical diagnosis of the disease. Adults with typical neurodevelopment were ascertained either as age-matched controls for study participants with WS or as healthy older adults who served as controls for a general population study of age-related cognitive impairment. The three groups were tested for differences in age and sex, using an independent samples t-test and a chi-square test, respectively.

Table 4 Demographics for volume analysis

Down syndrome (DS), Williams's syndrome (WS), and typically developing (TD) controls. SD= standard deviation, N=number, t=t-statistic.

										Group Contrasts					
	DS (N=14)			**TD** (N=82)			**WS** (N=41)			**DS v TD**		**WS v TD**		**DS v WS**	
	Range	Mean	SD	Range	Mean	SD	Range	Mean	SD	t	p-value	t	p-value	t	p-value
Age (years)	19 - 63	39	13	18 - 90	36	18	16 - 58	26	8	0.61	0.54	-3.44	1.0E-03	4.31	7.1E-05
										DS v WS v TD					
		N	%		N	%		N	%			$\chi 2$	p-value		
Male Sex		7	50		40	49		24	59			1.89	0.39		

Participants with TD and caregivers of individuals with DS or WS gave informed consent, while participants with DS or WS gave informed assent for this study. All study procedures were approved by the Vanderbilt University Institutional Review Board.

Magnetic Resonance Imaging Acquisition

Adults participated in an magnetic resonance imaging (MRI) scan in a Philips Achieva 3-Tesla scanner (Philips Medical Systems, Inc., Best, Netherlands) using an eight-channel SENSE head coil, housed in the Vanderbilt University Institute of Imaging Science (Nashville, TN). High-resolution three-dimensional anatomical T1-weighted MRI images were acquired using a turbo field echo (TFE) sequence with full brain coverage and the following parameters: field of view = 256×256 mm^2; in plane voxel resolution = 1×1 mm^2; repetition time (TR) = 8.9 ms; echo time (TE) = 4.6 ms; flip angle = 8°; slice thickness = 1 mm and 170 slices with no slice gap.

Neuroimaging Analysis

As described in Chapter 2, FreeSurfer processing was utilized to parcellate the brain into cortical and subcortical tissue classes and derive quantitative estimates of brain volume [94]. Image outputs from each stage of FreeSurfer processing were visually inspected independently by two imaging analysts (Courtney Edwards, Mary Ellen Koran). The raw T1-weighted images were visually inspected for any artifacts and subjects were discarded if significant artifact was present in any one of the images. The FreeSurfer output was visualized using FreeSurfer's tkmedit command and following the FreeSurfer Troubleshooting Reconstruction Work Flow on the FreeSurfer homepage (https://surfer.nmr.mgh.harvard.edu/fswiki/) to ensure that the parcellation and

segmentation steps were properly completed. Only images that passed quality control by both analysts were used; seven DS, five WS, and five TD adults were not included in the analysis because of failure to pass quality control, leaving a total of 14, 58 and 81 adults in each category, respectively. Quantitative estimates of volume were derived in a large set of spatially distinct region of interests (ROIs) that covered the entire brain, as specified in the Desikan atlas [98]. This atlas includes parcellations of gray and white matter and segmentations of subcortical gray matter, and also includes summary volumes (i.e. total cortex volume). Parcellations of the gray and white matter and segmentations of subcortical gray matter were included, along with two summary measurements of total gray and total white matter. See Table 5 and Table 6 for complete lists of ROIs included and excluded in the following analyses, respectively. The regions excluded from the analysis were either not of interest (i.e. choroid plexus) or were summation measures of sub-regions that were already included (i.e. total gray volume). Total intracranial volume (ICV) was also estimated in FreeSurfer, and all ROI measures were normalized to ICV.

Table 5 Regions of interest included in volume analysis

Included Regions of Interest		
3rdVentricle	lh_lingual_volume	rh_medialorbitofrontal_volume
4thVentricle	lh_medialorbitofrontal_volume	rh_middletemporal_volume
5thVentricle	lh_middletemporal_volume	rh_paracentral_volume
BrainStem	lh_paracentral_volume	rh_parahippocampal_volume
CC_Anterior	lh_parahippocampal_volume	rh_parsopercularis_volume
CC_Central	lh_parsopercularis_volume	rh_parsorbitalis_volume
CC_Mid_Anterior	lh_parsorbitalis_volume	rh_parstriangularis_volume
CC_Mid_Posterior	lh_parstriangularis_volume	rh_pericalcarine_volume
CC_Posterior	lh_pericalcarine_volume	rh_postcentral_volume
LeftAccumbensarea	lh_postcentral_volume	rh_posteriorcingulate_volume
LeftAmygdala	lh_posteriorcingulate_volume	rh_precentral_volume
LeftCaudate	lh_precentral_volume	rh_precuneus_volume
LeftCerebellumCortex	lh_precuneus_volume	rh_rostralanteriorcingulate_volume
LeftCerebellumWhiteMatter	lh_rostralanteriorcingulate_volume	rh_rostralmiddlefrontal_volume
LeftHippocampus	lh_rostralmiddlefrontal_volume	rh_superiorfrontal_volume
LeftInfLatVent	lh_superiorfrontal_volume	rh_superiorparietal_volume
LeftLateralVentricle	lh_superiorparietal_volume	rh_superiortemporal_volume
LeftPallidum	lh_superiortemporal_volume	rh_supramarginal_volume
LeftPutamen	lh_supramarginal_volume	rh_temporalpole_volume
LeftThalamusProper	lh_temporalpole_volume	rh_transversetemporal_volume
LeftVentralDC	lh_transversetemporal_volume	RightAccumbensarea
lh_bankssts_volume	rh_bankssts_volume	RightAmygdala
lh_caudalanteriorcingulate_volume	rh_caudalanteriorcingulate_volume	RightCaudate
lh_caudalmiddlefrontal_volume	rh_caudalmiddlefrontal_volume	RightCerebellumCortex
lh_cuneus_volume	rh_cuneus_volume	RightCerebellumWhiteMatter
lh_entorhinal_volume	rh_entorhinal_volume	RightHippocampus
lh_frontalpole_volume	rh_frontalpole_volume	RightInfLatVent
lh_fusiform_volume	rh_fusiform_volume	RightLateralVentricle
lh_inferiorparietal_volume	rh_inferiorparietal_volume	RightPallidum
lh_inferiortemporal_volume	rh_inferiortemporal_volume	RightPutamen
lh_insula_volume	rh_insula_volume	RightThalamusProper
lh_isthmuscingulate_volume	rh_isthmuscingulate_volume	RightVentralDC
lh_lateraloccipital_volume	rh_lateraloccipital_volume	CortexVol
lh_lateralorbitofrontal_volume	rh_lateralorbitofrontal_volume	CorticalWhiteMatterVol
	rh_lingual_volume	

Table 6 Regions of interest not included in volume analysis

Not Included
CSF
Leftchoroidplexus
LeftnonWMhypointensities
Leftvessel
LeftWMhypointensities
lhCortexVol
lhCorticalWhiteMatterVol
nonWMhypointensities
OpticChiasm
rhCortexVol
rhCorticalWhiteMatterVol
Rightchoroidplexus
RightnonWMhypointensities
Rightvessel
RightWMhypointensities
SubCortGrayVol
SupraTentorialVol
TotalGrayVol
WMhypointensities

Genotyping

Adults with DS had blood drawn for DNA extraction, which was directly genotyped for *APOE* using pre-made TaqMan single nucleotide polymorphism (SNP) genotyping assays of rs7412 and rs429358 from Applied Biosystems (ABI; Foster City, California). Negative controls (no template) and positive controls (DNA samples with known genotypes from Coriell Institute for Medical Research, Camden, New Jersey) were included on the plate for assay validation. Since genotyping was performed in a research laboratory that is not CLIA-certified, genotyping results were not returned to patients or their clinicians.

Cognitive Testing

For all participants with DS, we conducted a comprehensive battery of cognitive and neuropsychological tests, including the Dementia Questionnaire for People with Learning Disabilities (DLD) [26]. Although there is no "gold standard" for assessing dementia in individuals with DS, studies have shown that the DLD is useful in the differential diagnosis of dementia [27,121]. The DLD is a 50-item questionnaire that consists of eight subtests (short-term memory, long-term memory, spatial and temporal orientation, speech, practical skills, mood, activity and interest, and behavioral disturbance) that assess both cognition and social skills. The sum of cognitive scores (SCS) is calculated from the short-term memory, long-term memory, spatial and temporal orientation subtests. The sum of social scores (SOS) is calculated from the speech, practical skills, mood, activity, and interest and behavioral disturbance subtests. Higher scores on each subtest indicate greater impairment. A masters-level study coordinator with training and experience in cognitive and neuropsychological assessment administered the DLD.

Statistical Analysis

Our first two aims were to confirm previous findings of accelerated aging in DS compared to TD and to test for a comparable effect in WS relative to TD. In order to approach these aims we implemented a general linear model in R (http://www.R-project.org) across 103 separate regions of interest (ICV-corrected volume of each ROI = Diagnosis + Age + Sex + Diagnosis x Age). Diagnosis was dummy coded in the regression model with TD set as the reference category. Thus, our model included two diagnosis main effects (DS as 0 or 1 and WS as 0 or 1) and two interaction terms: age x DS and age x WS which statistically compare the age-related slopes of regional volume between the respective diagnostic category and typically developing controls. This method and a three category method in ANCOVA are statistically equivalent [122]. However, in the linear regression method used here, the t-tests based on dummy coded variables directly tests the alternative hypothesis that the coded group differs from the reference group (in this case, TD controls), which aids in the interpretation of results.

Sex was coded as a binary discrete variable (male as 0; female as 1). A Bonferroni corrected significance threshold of $p<4.85 \times 10^{-4}$ was applied to the interaction terms in order to correct for the 103 ROIs tested (see Table 5 for list of ROIs tested). A *post hoc* analysis was conducted to determine the sensitivity of results due to outliers. Outliers were defined as adults with ICV-corrected total gray matter volume outside of the grand mean +/- 2 standard deviations, a relatively strict correction (calculated in SPSS, www.ibm.com/software/analytics/spss/).

A final aim was to test for age-related effects unique to DS. The same general linear model was used (ICV-corrected volume of each ROI = Diagnosis + Age + Sex + Diagnosis x Age), but we only included DS and WS in our diagnostic category (WS = 0

and DS = 1). The same Bonferroni correction was applied to determine the significant interaction terms and again a *post hoc* analysis was performed after removing statistical outliers.

Secondary Exploratory Analyses

In order to further explore age-related volume that is specific to DS, we performed linear regression to test for an association between brain volume and other cognitive and genetic risk factors. To control for Type I error, we restricted our analysis to brain regions that showed significant age-related effects, which were stronger in DS relative to TD or WS. Predictors included age, sex, and the variable of interest. For each ROI we tested for an association with DLD-SOS or DLD-SCS as the continuous variable of interest. Since DLD data were only collected for participants with DS, analyses were restricted to the DS group. We report the t-statistic for the variable of interest (DLD-SOS or DLD-SCS), along with its unadjusted p-value, and we report the change in R^2 comparing the full model with the variable of interest to the reduced model (Table 7).

Next we performed an exploratory analysis to determine the relationship between *APOE* genotype and age-related volume effects in DS. The absence/presence of *APOE* ε4 alleles was coded as 0/1 respectively. We report the R^2 of the full model with *APOE*, the change in R^2 with the addition of *APOE,* and the unadjusted p-value of the *APOE* term (Table 7).

Table 7 Relationship between volume and DLD cognitive scores or *APOE* in brain regions showing a correlation with age in Down Syndrome participants. p-values are uncorrected and those < 0.05 are bolded.

	DLD-SCS			**DLD-SOS**			***APOE***		
Region of Interest	**t**	**Change in R^2**	**p-value**	**t**	**Change in R^2**	**p-value**	**t**	**Change in R^2**	**p-value**
LILV	2.37	0.21	**0.042**	4.72	0.38	**0.001**	2.61	0.22	**0.026**
RILV	2.56	0.25	**0.031**	4.01	0.38	**0.003**	2.47	0.22	**0.033**
Left Superior Parietal	-1.32	0.06	0.219	0.41	0.01	0.693	-1.06	0.04	0.315
Left Pars orbitalis	-1.66	0.08	0.131	-1.32	0.06	0.220	-1.23	0.10	0.247
Left Inferior Parietal	-1.21	0.07	0.256	-1.59	0.10	0.146	-1.87	0.06	0.091
Right Post Central Gyrus	-0.54	0.01	0.604	-1.11	0.05	0.294	0.05	0.00	0.961
Left Ventricle	0.57	0.01	0.582	2.06	0.13	0.069	1.45	0.07	0.178
Right Ventricle	0.91	0.03	0.386	2.59	0.15	**0.029**	1.78	0.08	0.105

Table 8 Brain regions where volume had a significant relationship with age between participants with Down Syndrome and typically developing controls in the model Volume of ROI = Age + Sex + Diagnosis + Diagnosis x Age. p-values are uncorrected, 103 tests were analyzed.

	DS x Age Interaction Term		
Region of Interest	**t**	**Change in R^2**	**p-value**
LILV	4.31	0.09	3.25E-05
RILV	4.05	0.10	9.03E-05
Left Superior Parietal	-4.02	0.08	1.01E-04
Left Inferior Parietal	-3.97	0.08	1.23E-04
Left Pars Orbitalis	-3.82	0.07	2.11E-04
Right Post Central Gyrus	-3.67	0.07	3.58E-04

Table 9 Brain regions where volume had a significant relationship with age between participants with Down Syndrome and Williams Syndrome in the model Volume of ROI = Age + Sex + Diagnosis + Diagnosis x Age. p-values are uncorrected, 103 tests were analyzed.

	Diagnosis Term (DS vs. WS)		
Region of Interest	**t**	**Change in R^2**	**p-value**
Right Lateral Ventricle	4.42	0.14	8.64E-05
Left Lateral Ventricle	3.75	0.12	1.35E-04

Results

Our first analysis attempted to replicate previous findings of accelerated aging in DS and to test for similar effects in WS. Consistent with previous findings, the DS group showed

significantly greater age-related effects on grey matter volume relative to TD controls in the regions of the orbitofrontal cortex (the left pars orbitalis) and the parietal cortex (the left superior parietal lobe, the left inferior parietal lobe and the right post central gyrus) (see Table 8, full results in supplementary Appendix B

SUPPORTING INFORMATION FOR CHAPTER 3

Table 20). Individuals with DS also showed significantly increased age-related effects on volume of the left and right inferior lateral ventricles (LILV and RILV, respectively). In contrast, there were no significant differences in age-related volume between WS and TD controls. The summary measurements of total white matter and total gray matter volumes were also analyzed, and the DS group showed greater age-related effects on total grey matter volume (unadjusted-p=0.007) while there was no significant effect in the total white matter volume measure (unadjusted-p=0.055). As a post-hoc analysis, older TD subjects were dropped in order to analyze only those subjects whose ages overlapped (subjects older than the oldest DS subject were dropped (63 years)). Only the left superior parietal lobe remains significant at the Bonferroni corrected level ($p = 4.49 \times 10^{-4}$).

Our second analysis compared age-related volume in DS to age-related volume in WS (Table 9). The DS group showed a stronger relationship between age and volume for the left and right lateral ventricles relative to WS, and this difference remained significant after correcting for multiple comparisons. Plots of age versus volume for all significant ROIs are presented in Figure 13 and Figure 14.

To investigate whether outliers were driving the observed effects, we removed the participants whose ICV-corrected total gray matter volume was outside of two standard deviations of the grand mean, and we repeated our analyses. One DS subject and four WS adults were removed, but no outliers were identified for the TD group. The interaction model term (Diagnosis x Age) remained significant after Bonferroni correction for the left superior parietal lobe and the right lateral ventricle, and in all the other ROIs found significant in primary analyses, the interaction term was significant at a nominal (unadjusted) $p<0.05$. No additional ROIs reached Bonferroni significance. These results are presented in Table 10, Table 11, and Figure 15.

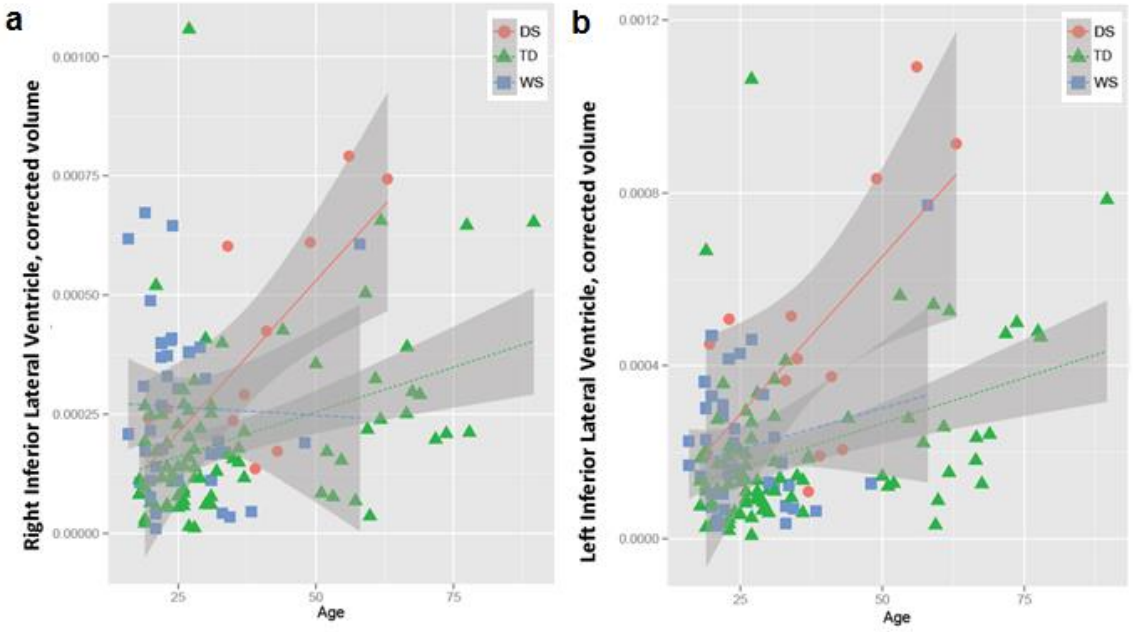

Figure 13: Relationship between inferior lateral ventricle volume and age in Down Syndrome, Williams Syndrome, and typically developing controls.

Regional brain volumes normalized to ICV are plotted in relationship to age across the three subject groups (Down syndrome (DS) in red, typical development (TD) in green, and William syndrome (WS) in blue) in: (a) left inferior lateral ventricle (LILV) and (b) right inferior lateral ventricle (RILV)

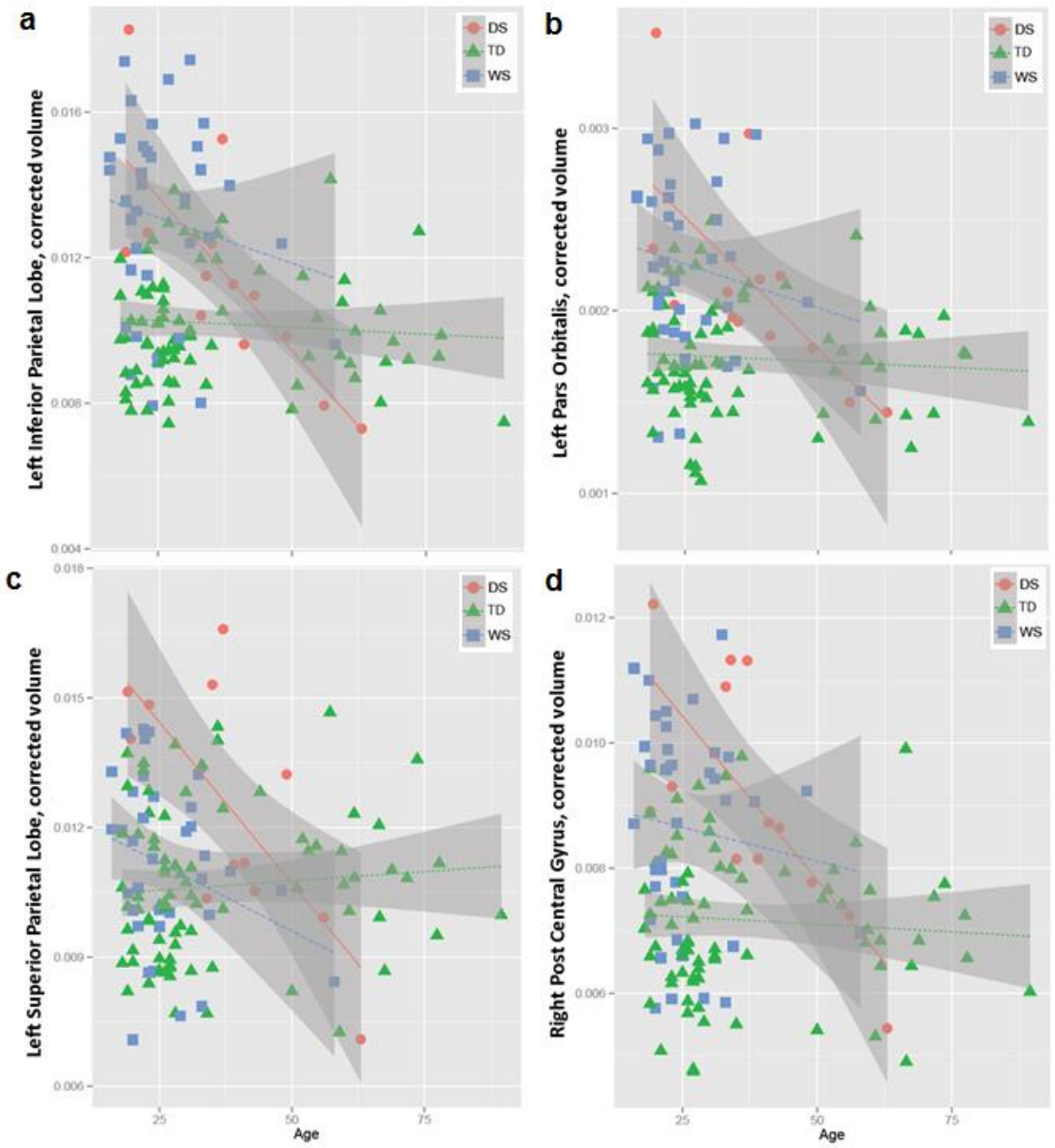

Figure 14: Relationship between regional brain volumes and age in Down Syndrome, Williams Syndrome, and typically developing controls.

Regional brain volumes normalized to ICV are plotted in relationship to age across the three subject groups (Down syndrome (DS) in red, typical development (TD) in green, and William syndrome (WS) in blue) in (a) left inferior parietal lobe, (b) left pars orbitalis, (c) left superior parietal lobe, and (d) right post central gyrus.

Table 10 Brain regions where volume had a significant relationship with age between participants with Down Syndrome and typically developing controls after outliers removed.

Bolded p-values still pass Bonferroni correction ($p<4.85 \times 10^{-4}$).

ROI	DS x Age		
	t	Change in R^2	p-value
LILV	2.39	0.04	1.8E-02
RILV	2.12	0.05	3.6E-02
Left Superior Parietal	-3.64	0.07	**4.0E-04**
Left Inferior Parietal	-3.48	0.07	7.1E-04
Left Pars Orbitalis	-3.20	0.06	1.7E-03
Right Post Central Gyrus	-3.26	0.06	1.4E-03

Table 11 Brain regions where volume had a significant relationship with age between participants with Down Syndrome and Williams Syndrome after outliers removed.

Bolded p-values still pass Bonferroni correction.

ROI	DS vs. WS		
	t	Change in R^2	p-value
Right Lateral Ventricle	4.20	0.024	**1.34E-04**
Left Lateral Ventricle	3.73	0.022	5.50E-04

Figure 15: Relationship between regional brain volumes and age in Down Syndrome, Williams Syndrome, and typically developing controls after outliers were removed.

This figure shows results from analyses which excluded adults with gray matter volumes normalized to intracranial volume (ICV) that fell outside two standard deviations of the grand mean. Regional brain volumes normalized to ICV are plotted in relationship to age across the three subject groups (Down syndrome (DS) in red, typical development (TD) in green, and William syndrome (WS) in blue) in (a) the left inferior lateral ventricle (LILV), (b) right inferior lateral ventricle (RILV), (c) left inferior parietal lobe, (d) left pars orbitalis, (e) left superior parietal lobe, and (f) right post central gyrus.

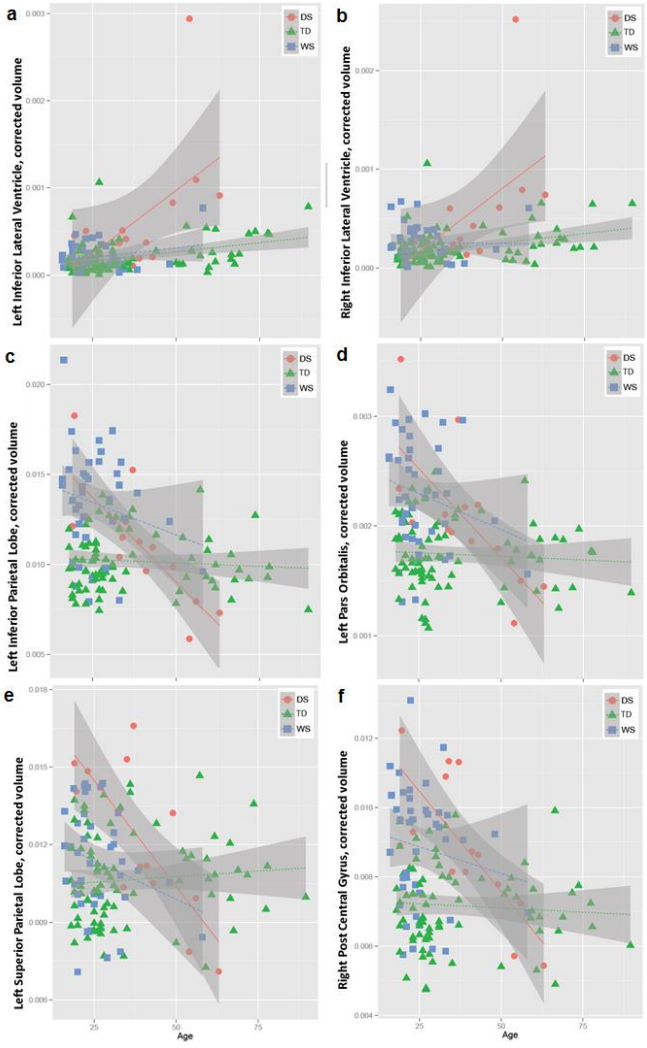

In secondary analyses, we explored the relationships between brain volume in the eight significant ROIs reported above and the DLD-SOS score, the DLD-SCS score, and *APOE* status in DS adults using linear regression. Two, or 14%, of the subjects with DS had *APOE* e2 alleles, and three, or 21%, had e4 alleles. These frequencies are slightly

higher than expected from the allele frequencies in the general or DS populations, but this differential may be due to small sample size [123,124]. Full results are presented in Table 7. All three variables were significantly associated with LILV and RILV volume ($p<0.05$). DLD-SCS and -SOS scores were significantly correlated ($r^2=0.770$, $p=0.002$) and explained similarly high rates of variability in regional brain volume. DLS-SCS scores explained 20.6 and 24.7% of the variance in LILV and RILV volume, respectively ($p=0.042$ and $p=0.031$; Figure 16). DLD-SOS scores explained 38.3 and 37.6% of variance in LILV and RILV volume, respectively ($p=0.001$ and $p=0.003$; Figure 17). DLD-SOS was also significantly associated with the overall right ventricular volume ($p=0.029$) and explained 15% of right ventricular volume variance. *APOE* explained 22% of the variance in LILV and RILV volume with $p=0.026$ and 0.033, respectively (Figure 18).

After the one DS subject who could be considered an outlier based on gray matter volume (as described above) was removed, the relationships between DLD-SCS and RILV and between DLD-SOS and LILV remained significant ($p=0.037$ and 0.009, respectively). However, the associations in all other ROIs that were significant in primary analyses were no longer significant after outlier removal. The removed subject was one of three adults who had an $\varepsilon 4$ allele.

Figure 16: Regional brain volumes in relation to Dementia Questionnaire for People with Learning Disabilities-sum of cognitive scores (DLD-SCS) in the Down Syndrome cohort.

Regional brain volumes normalized to ICV are plotted in relationship to DLD-SCS across the Down syndrome subject group in: (a) Right inferior lateral ventricle (LILV) and (b) Left inferior lateral ventricle (RILV). Subject data points are marked as APOE ε4 carriers (x) or non-carriers (o). For visualization purposes, we have overlaid a linear trend line for all data points, but note this line does not reflect covariate adjustments in the statistical model tested.

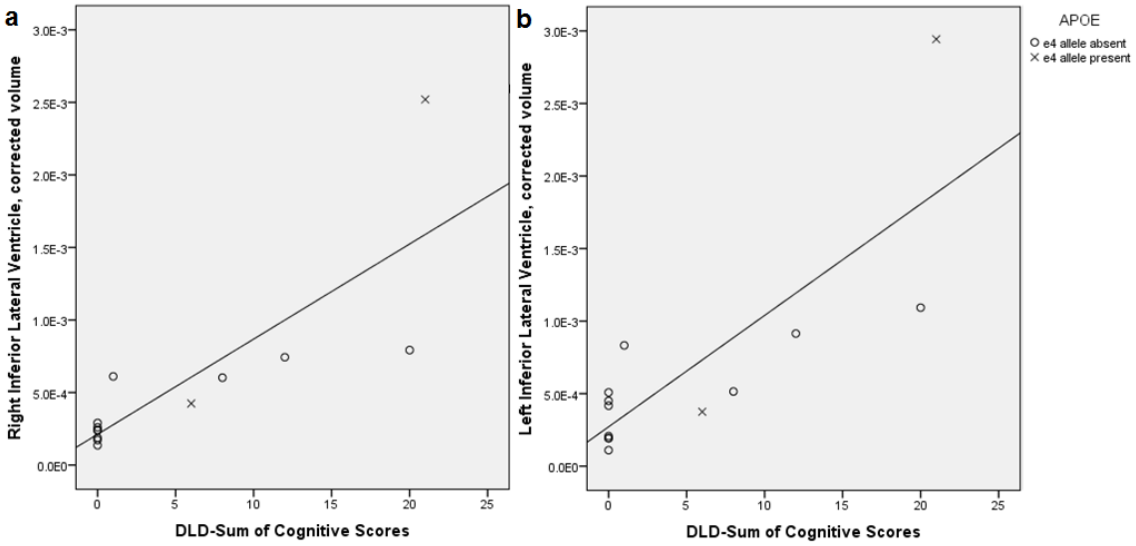

Figure 17: Regional brain volumes in relation to Dementia Questionnaire for People with Learning Disabilities-sum of social scores (DLD-SOS) in the Down Syndrome cohort.

Regional brain volumes normalized to ICV are plotted in relationship to DLD-SOS across the Down syndrome subject group in: (a) Right inferior lateral ventricle (LILV) and (b) Left inferior lateral ventricle (RILV). Subject data points are marked as APOE ε4 carriers (x) or non-carriers (o). For visualization purposes, we have overlaid a linear trend line for all data points, but note this line does not reflect covariate adjustments in the statistical model tested.

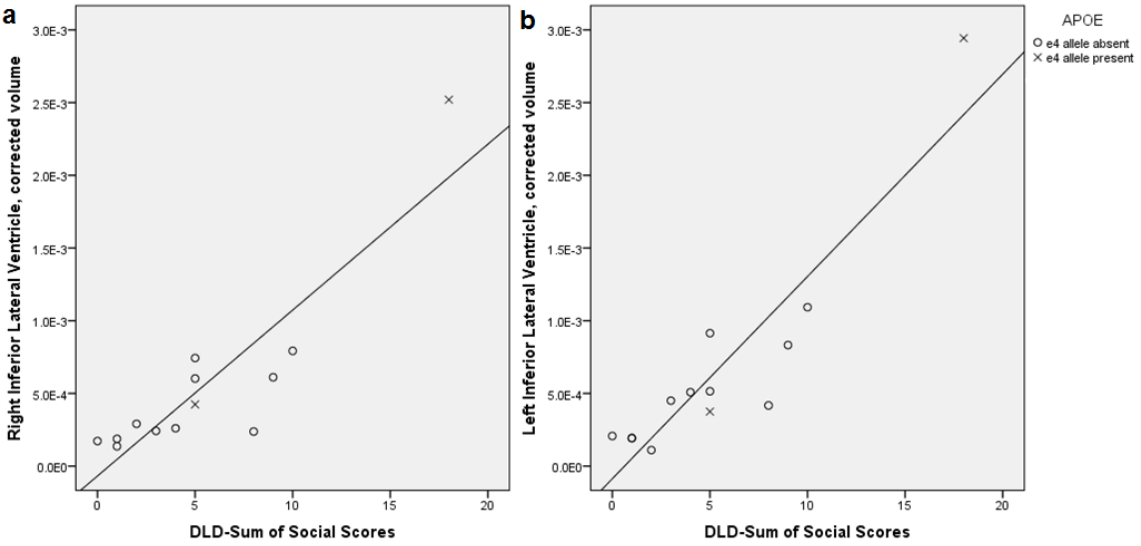

Figure 18: Relationship between age and brain region volumes stratified by APOE risk allele carrier status.

For the purpose of visualization, regional brain volumes normalized to ICV are plotted in relationship to age across the Down syndrome subject group, with adults marked as APOE ε4 carriers (x) or non-carriers (o) in: (a) Left inferior lateral ventricle (LILV) and (b) Right inferior lateral ventricle (RILV). For visualization purposes, we have overlaid a linear trend line for all data points reflecting *APOE* e4 presence (dotted line) or absence (non-dotted line), but note this line does not reflect covariate adjustments in the statistical model tested. Also note that there are three *APOE* e4 carriers.

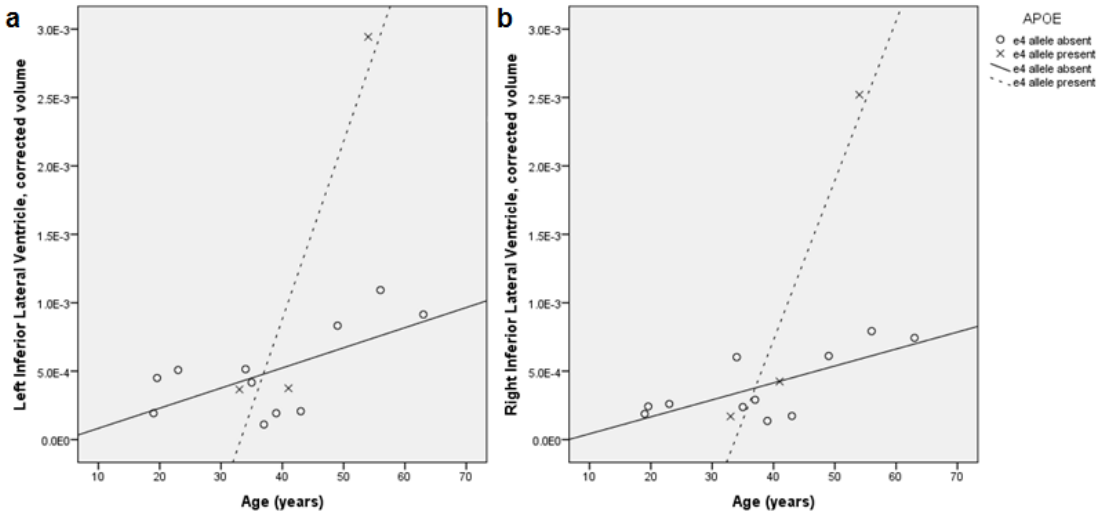

Discussion

The first aim of the current study was to confirm previous findings of accelerated brain aging in DS [40]. In previous studies, adults with DS had significantly stronger relationships between age and volume in the frontal, parietal, and temporal lobes, and the lateral ventricles [40]. We replicated these findings in the frontal lobe (specifically, the left pars orbitalis gyri frontalis inferioris), the parietal lobe (specifically, the left superior and left inferior parietal cortices and the right post central gyrus), and in the lateral ventricles (specifically, the LILV and RILV).

Interestingly, atrophy in these grey matter regions may be explained by the link between DS and Alzheimer's Disease (AD). Individuals with DS are at a greatly increased risk of developing AD, with up to 70 percent developing dementia by the age of 70 [24]. In fact, adults with DS account for up to 60% of individuals with developmental disabilities who exhibit signs of AD [25]. The risk for AD in DS is primarily linked to triplication of the amyloid precursor protein (*APP*), which is on chromosome 21 [33]. However, one's genotype at the apolipoprotein E (*APOE*) gene, whose protein product is involved in the processing of amyloid beta isoforms, modulates risk for developing AD in the DS population [36,37]. Postmortem studies have revealed that plaque load in adults with DS increases with age and by 40 years of age, nearly all individuals with DS have amyloid beta plaques in the brain [32], and this characteristic feature of AD has neurotoxic effects that can lead to neurodegeneration and loss in brain volume [125]. More specifically, both the frontal and parietal lobes have shown increased amyloid load as measured by positron emission tomography (PET) in participants with DS [58]. Therefore, the age-related affects detected in this study may be due to the neurotoxic effects of age-related increases in amyloid load in adults with DS.

Age-related volume in DS relative to WS adults was significant in the left and right total lateral ventricles, even after Bonferroni correction for multiple comparisons, and there was a stronger relationship between age and volume in the inferior lateral ventricles when comparing the DS and TD groups. Both of these results are particularly interesting given the high prevalence of AD in DS and the association between ventricular dilation and AD. Volume of the lateral ventricles has repeatedly shown a relationship to AD status and disease progression in the general population [48–51]. The lateral ventricles normally dilate over time with age, as brain tissue volume decreases, but in patients with mild cognitive impairment (MCI) or AD, the rate of ventricular dilation is much greater

than in the general aging population [52]. The inferior lateral ventricles are surrounded by subcortical gray matter structures and these structures, particularly the hippocampus, entorhinal cortex, and amygdala, accumulate amyloid beta plaques and exhibit atrophy in AD [4,52] and DS [126–130]. Since ventricular dilation is cumulatively and inversely reflective of atrophy of these surrounding structures [131], and since we found that the strong relationship between age and ventricular volume is specific to DS (and not present in WS), the results seen in this study may be reflective of the neurotoxic effects of AD pathology in the structures surrounding the ventricles.

We also investigated whether the WS group experienced accelerated aging compared to the TD group, but we did not find evidence to support this hypothesis, which is in line with the one previously reported finding of aging WS adults [115]. This may be due to the difference in age ranges between the WS and TD groups (Table 4), and further investigation of age-related volume in WS in a larger study, preferably with longitudinal data, is warranted.

As an exploratory analysis in the DS cohort only, regions with significant age-related changes (in DS vs. TD and DS vs. WS) were evaluated for association with DLD-SOS and DLD-SCS tests and *APOE* ε4 carrier status. We observed a significant relationship between inferior lateral ventricle volume and both the cognitive and social scores on the DLD, a test that measures dementia-related impairments in the DS population. The social sub-score of the DLD was also significantly associated with right ventricular volume. Previous studies have shown that individuals with DS have increased regional brain atrophy with onset of dementia [126,128,129,132], and in the current study, we observed that higher levels of dementia symptomology (as measured by the DLD) were associated with increased ventricular volume, an MRI biomarker of neurodegeneration.

APOE is a very strong genetic risk factor predisposing patients to AD-associated neurodegeneration, with even TD adults who are carriers of the ε4 risk allele showing greater neurodegeneration before symptom onset [133]. While *APOE* is also associated with further increased risk of AD in the DS population, to our knowledge, this is the first study in DS to investigate the association of *APOE* ε4 carrier status with MRI volume data. The observed ε4 carrier frequency was 3/28 alleles, or 11%, which is similar to the frequency observed in the general population (13%). However, one of the three ε4 carriers was the DS group outlier, and it was this subject who drove the difference in brain volume by *APOE* genotype. Thus, we are not able to make a strong conclusion based on these data, and future analyses with larger sample sizes will be necessary to confirm an effect of *APOE* on brain volume in Down syndrome.

The present results must be interpreted within the framework of our statistical models. The WS and DS groups differed in mean age, but in all cases, we included covariates related to neurodegeneration including age and sex in an effort to control for these factors. The highly significant p-values we observed seem to be driven in part by one DS outlier, as evidenced in Table 10 and Table 11, but the effect sizes (i.e., the differences in the volume versus age trends) do not change when the outliers are removed (Figure 15). Furthermore, though this study found a significant age-related difference in DS adults in AD-related regions, we may have been underpowered to detect more subtle AD-related changes due to 1) the relatively small sample size of the DS group, 2) the strict statistical threshold used for significance, and 3) the fact that FreeSurfer parameter estimates for smaller subcortical areas, such as the entorhinal cortex and hippocampus, are known to exhibit greater error [134]. Despite this, some AD-related regions were nominally significant at an unadjusted $p<0.005$ (left hippocampus: p=0 .0023, right amygdala: p=0.0042, left amygdala: p=0.0042). These results warrant further analysis of

age-related affects in AD-related regions in a larger cohort of DS adults. In the future, to optimize this study, we would ideally want to age-match the populations under study.

In conclusion, we used a whole-brain ROI approach to investigate the relationship between age and MRI-derived brain volume across adults with a neurodevelopmental disorder (DS and WS) or typical development. We also incorporated cognitive test data and genetic risk data in a secondary exploratory analysis of the DS group. We found that adults with DS had profound age-related effects in grey matter regions of the orbitofrontal cortex (the left pars orbitalis) and the parietal cortex (the left superior parietal lobe, the left inferior parietal lobe and the right post central gyrus), and in the left and right inferior lateral ventricles, as compared to WS adults. By combining imaging and cognitive testing data, we concluded that the inferior lateral ventricles, which are surrounded by structures that typically atrophy in normal aging and also in diseased states like AD, were also associated with dementia rating scores in the DS group. While *APOE* also showed a trend for association with regional brain volume, a larger sample size will be needed to accurately estimate this effect.

Supporting Information

Example code used in this analysis is available in Appendix B.

Chapter 4

GENETIC INTERACTIONS ASSOCIATED WITH LONGITUDINAL CHANGES IN VENTRICLE SIZE IN ALZHEIMER'S DISEASE

Adapted from:

Koran ME, Hohman TJ, Meda SA, Thornton-Wells TA. Genetic Interactions within Inositol-Related Pathways are Associated with Longitudinal Changes in Ventricle Size. Journal of Alzheimer's Disease. In Press.

Introduction

Late onset Alzheimer's disease (LOAD) is a devastating, degenerative neurological disease that affects over 5 million people in the United States alone, an already substantial statistic that is expected to triple by 2050 (www.alz.org) [3]. The complex genetics of LOAD have proven difficult to unravel due to the disease's clinical and genetic heterogeneity. To date, 21 genes/genomic loci have been confirmed by replication and meta-analysis to be associated with LOAD [11,14]. Of these genes, only *APOE* has a large effect with an odds ratio of about 3.7 for one copy of the high risk ε4 allele; the remaining genes exhibit small effect sizes, with odds ratios hovering between 0.73 and 1.22 [11,14]. In order to increase our power and biological interpretability of this complex disease, we expanded our analysis beyond the traditional approach of testing for single marker effects using binary disease status as the primary outcome. In this

study, we include rich phenotypic information derived from magnetic resonance imaging (MRI) quantitative traits (QTs) as our outcomes, which addresses the problem of clinical heterogeneity, and we explicitly test for gene-gene interactions, which confronts the issue of genetic heterogeneity [135].

Though these have not been replicated, interactions have shown significant associations in many other complex diseases such as schizophrenia [136], autism [137] and type 2 diabetes [138]. In LOAD, previous gene-gene interaction studies have implicated interactions between *CR1* and *APOE* [81], cholesterol trafficking genes [139,140], tau phosphorylation genes [141], and calcium signaling and axon guidance genes [83]. These studies demonstrate that important mechanistic insight can be garnered from investigating higher order genetic relationships in complex diseases like LOAD.

For LOAD and other brain-based diseases, brain structure derived from imaging modalities can be the source of relevant QTs or endophenotypes. Endophenotypes are biological measurements that are more proximal to genetic function and pathology than disease status [62] and can provide increased statistical power (and therefore decreased sample size requirements) over dichotomous outcome variables [64]. Many measurements of brain structures correlate with LOAD status and to have greater sensitivity in detecting early pathological changes [142]. QTs from structural MRI have been used as endophenotypes in LOAD GWAS previously [74], and in this study, we extend that work by investigating associations of an endophenotype of LOAD with gene-gene interactions.

The lateral ventricles have repeatedly shown a relationship to Alzheimer's disease (AD) status and progression [48–51]. The lateral ventricles normally dilate over time with age, as brain tissue volume decreases, but in patients with mild cognitive impairment (MCI) or AD, the rate of ventricular dilation is much greater than in the normal aging population [52].

MRI measurements of lateral ventricle expansion correlate with disease status, with ventricular volumes and rates of dilation increasing from healthy controls (HC) to MCI and from MCI to AD [52]. The inferior horns of the lateral ventricles are surrounded by gray and white matter structures (corpus callosum, hippocampus, amygdala, caudate nucleus, deep white matter, and thalamus). These structures, particularly the hippocampus and amygdala, often deteriorate in AD, and patients with AD and MCI have significantly higher rates of tissue atrophy in these structures than normal aging adults [52], and ventricular dilation is inversely reflective of atrophy of these surrounding structures [131]. Ventricular dilation is evident 10 years before clinical symptoms, and dilation rate rapidly accelerates two years prior to initial MCI diagnosis, making longitudinal MRI measurement of ventricular dilation a plausible clinical trial biomarker for disease inclusion or progression criteria [52]. Because of the evidence demonstrating atrophy of brain structures surrounding the inferior lateral ventricles (ILVs) in LOAD and because changes in these structures are reflected and magnified in the ILVs, we chose to investigate genetic associations with longitudinal change in volume of these structures.

While correction for multiple testing in single-marker genome-wide association analysis is highly burdensome, due to combinatorics, in genome-wide interaction analyses it is essentially prohibitive except perhaps for very large datasets [143]. However, interaction analyses limited to known candidate genes are unduly constrained by information from previously published studies [144]. Alternative strategies may instead conduct intelligent variable selection based on prior biological knowledge assembled from a wide variety of scientific disciplines [145]. In this study, we selected genes participating in common biological pathways for investigation of gene-gene interactions associated with the endophenotype of ILV atrophy rate. By doing so, we aimed to increase the biological

plausibility of interactions that are novel to AD, while decreasing computational burden. We hypothesized that novel gene-gene interactions would be significantly associated with the dilation of the ILVs and that the novel interactions will generate new or altered hypotheses regarding the etiology of this disease.

Materials and Methods

Data used in the preparation of this article were obtained from the ADNI database (adni.loni.ucla.edu). The ADNI was launched in 2003 by the National Institute on Aging (NIA), the National Institute of Biomedical Imaging and Bioengineering (NIBIB), the Food and Drug Administration (FDA), private pharmaceutical companies and non-profit organizations, as a $60 million, 5-year public-private partnership. The primary goal of ADNI has been to test whether serial magnetic resonance imaging (MRI), PET, other biological markers, and clinical and neuropsychological assessment can be combined to measure the progression of MCI and early AD. Determination of sensitive and specific markers of very early AD progression is intended to aid researchers and clinicians in developing new treatments and monitoring their effectiveness, as well as lessening the time and cost of clinical trials.

The Principal Investigator of this initiative is Michael W. Weiner, MD, VA Medical Center and University of California – San Francisco. ADNI is the result of efforts of many co-investigators from a broad range of academic institutions and private corporations, and subjects have been recruited from over 50 sites across the U.S. and Canada. The initial goal of ADNI was to recruit 800 adults, ages 55 to 90, to participate in the research, approximately 200 cognitively normal older individuals to be followed for 3 years, 400

people with MCI to be followed for 3 years and 200 people with early AD to be followed for 2 years. Further information on ADNI can be found here [146].

Subjects

Participants were enrolled based on the criteria outlined in the ADNI-1 protocols (http://www.adni-info.org/Scientists/AboutADNI.aspx). Information on ADNI subject protocols can be found here [147]. To minimize population stratification, only Caucasian subjects who had both genotype data and T1-weighted MRI data were included. Demographic data are presented in Table 12.

Table 12 Demographic data for genetic interaction association with longitudinal inferior lateral ventricle volume change

	Clinical Diagnosis[#]		
	Normal Control	Mild Cognitive Impairment	Alzheimer's Disease
Number of Patients	187	191	352
Number of *APOE*-ε4 Carriers	45	81	231
Number of Females	85	61	146
Mean Baseline Age (SD[^])	75.98 (5.61)	75.79 (7.09)	75.13 (7.33)
Mean Years of Education (SD[^])	16.11 (2.79)	15.73 (3.01)	15.32 (2.97)
Mean RILV slope* (SD[^])	70.55 (77.37)	119.85 (123.15)	237.67 (185.37)
Mean LILV slope* (SD[^])	68.52 (78.63)	121.65 (110.92)	237.55 (179.6)

Clinical Diagnosis[#]:
Normal Control subjects had a Mini-Mental Status Examination (MMSE) score between 24 and 30, a Clinical Dementia Rating (CDR) score of 0, and were not depressed (Geriatric Depression Scale score < 6).
Mild Cognitive Impairment subjects had a MMSE score between 24 and 30; objective memory impairment, subjective memory impairment, and a CDR score of 0.5.
Alzheimer's Disease subjects met clinical criteria for dementia, had an MMSE of between 20 and 26, and had CDR score of .5 or 1.
SD[^]: standard deviation.
LILV/RILV*: Left/Right inferior lateral ventricles.

Genotyping

Genotyping was performed by the ADNI Genetics Core using the Illumina Infinium Human-610-Quad BeadChip. Further information about the ADNI Genetics Core efforts can be found here [148]. ADNI quality control (QC) steps included removing copy number variant probes, strand checking, base pair position checking, and allele specificity checking [149]. Further QC was performed using PLINK software (version 1.07; [150]), excluding SNPs with a genotyping efficiency < 95%, out of Hardy Weinberg Equilibrium ($p<1x10^{-6}$), or with a minor allele frequency (MAF) of < 5%. Subjects were excluded if they had a call rate < 95%, if there was a reported versus genetic sex inconsistency, or if relatedness was established (PI_HAT > 0.5). After QC, 515,839 SNPs and 730 subjects remained available for discovery analyses.

Analysis of Imaging Data

Structural T1-weighted MRI scans were acquired on subjects at baseline, 12, 24, and 36 month follow-up appointments as per the ADNI protocol [151]. Further information on ADNI's MRI protocols can be found here [151,152]. Cortical reconstruction and volumetric segmentation of these images were performed with the FreeSurfer [153] image analysis suite version 4.3 by the ADNI consortium which has been described in detail elsewhere [154]. An early version of the longitudinal image processing framework was used to process the sequential scans [155]. Volumes of the right and left ILV (RILV and LILV, respectively) were calculated in FreeSurfer (in mm^3) for every scan available for each individual in the dataset and slopes of change in RILV and LILV volume over time were calculated in SAS 9.3 (SAS Institute Inc., Cary, NC) using mixed model regression (PROC MIXED) to leverage the longitudinal data available in ADNI-1. We used the

slopes of change of the LILV and RILV as our primary outcome measurement (mm^3/year) and included a measurement of intracranial volume (ICV in mm^3) as a covariate in all volume analyses, which was also defined with FreeSurfer.

SNP-SNP Interaction Analysis

Genotype data that passed QC were analyzed in a pathway-based interaction analysis using the publicly available InterSNP v1.0.10 program [156]. We took advantage of InterSNP's pathway based option that tests SNP-SNP pairs between genes that belong to a common biological pathway derived from all of the pathways in the Kyoto Encyclopedia of Genes and Genomes (KEGG) database (http://www.genome.jp/kegg/). The KEGG database is a collection of manually curated pathways based on published literature for metabolism, genetic and environmental information processing, and human diseases, including AD [157,158]. This option decreases the number of tests performed and also increases the interpretability of an interaction based on *a priori* information. SNP-SNP interaction effects were explored using a dominant model and a linear regression framework for QTs [156]. A total of 130,512,955 SNP-SNP interaction pairs were tested for each region of interest (ROI), and SNP-SNP pairs were considered significant after Bonferroni correction accounting for the number of pairs tested ($p < 3.83x10^{-10}$). All SNPs were entered into the model as binary variables (minor allele absent or present) to attenuate the problem of data sparsity commonly confronted in interaction analyses.

Model covariates included: baseline age (in years), sex, education (in years), *APOE* status (number of ε4 risk alleles), and last diagnosis recorded as of January 2013 (1= Normal, 2=MCI, 3=AD). Each of these covariates was chosen to avoid confounding, with the goal of identifying interactions which explain variance *beyond* these known risk

factors. The brain is known to atrophy over time even in normal aging [159], and the rate of change differs by sex [160]. Education level is correlated with age of disease onset [161]. *APOE* is a very strong genetic risk factor predisposing patients to LOAD, with even normal subjects who are carriers of the risk allele showing greater neurodegeneration before any symptom onset [133]. And finally, atrophy rates are known to trend with disease status, wherein AD>MCI>HC [48–50,162].

Significant SNP-SNP interactions were annotated to their gene-gene pairs using dbSNP (Homo sapiens, updated in build 137) and their common pathways using KEGG. InterSNP calculates contingency tables which can be seen in Table 13. The difference in R^2 for these models was calculated in SPSS as $R^2 = R^2_{\text{(full model with interaction term)}} - R^2_{\text{(reduced model without interaction term)}}$. Visualization of interaction effects was created in SPSS as well, showing rate of change by allelic combination (Figure 19, Figure 20, Figure 21, Figure 22).

Table 13 Contingency tables for significant SNP-SNP interactions from genetic interaction association with longitudinal inferior lateral ventricle volume change

		rs178051*(PI4KA)*		**Total**
		T	*C*	
rs9295289*(SYNJ2)*	*T*	552	107	659
	C	61	9	70
Total		613	116	729

		rs3744566*(MYH2)*		**Total**
		C	*T*	
rs11596284*(PARD3)*	*A*	557	98	655
	C	63	10	73
Total		620	108	728

		rs7154732*(ABHD12B)*		**Total**
		T	*C*	
rs11614805*(PDE3A)*	*C*	579	60	639
	T	81	5	86
Total		660	65	725

		rs1922127*(PRKG1)*		**Total**
		G	*A*	
rs11590865*(OR2L13)*	*A*	460	194	654
	G	56	18	74
Total		516	212	728

Results

Pathway Based Interaction Analysis:

Demographic information is presented in Table 12. The study sample included 187 NC, 191 MCI, and 352 AD subjects. The number of *APOE*-ε4 carriers is enriched in the AD and MCI subjects. The slopes of the RILV and LILV increased from NC to MCI to AD subjects. We identified four Bonferroni-corrected significant SNP-SNP interactions in the RILV corresponding to the gene-gene pairs: *SYNJ2-PI4KA***,** *PARD3-MYH2*, *PDE3A-ABHD12B*, and *OR2L13-PRKG1,* in order of significance (Table 15). None of the SNPs involved had significant main effects in the dominant model (all main effects had uncorrected $p \geq 0.01$).

One Bonferroni-corrected ($p < 3.83 \times 10^{-10}$) significant SNP-SNP interaction was discovered in the LILV corresponding to *SYNJ2-PI4KA*. The specific SNP-SNP interaction corresponding to *SYNJ2-PI4KA* was the same in both the RILV and LILV and was the most significant in both hemispheres (RILV: $p = 9.13 \times 10^{-12}$; LILV: $p = 8.17 \times 10^{-13}$). This gene-gene pair belongs to the metabolic, the inositol phosphate metabolism and the phosphatidylinositol signaling system pathways in KEGG (hsa001100, hsa00562 and hsa04070, respectively), and neither gene is involved in additional KEGG pathways independently. The effect of this interaction was in the same direction for both hemispheres (β_{LILV}=352.44 and β_{RILV}=351.88) and explained >4% of the variance in both the RILV and LILV ($R^2_{RILV} = 0.043$, $R^2_{LILV} = 0.046$). As seen in Figure 19 and Figure 20, having the minor allele for both genes corresponded to an increased rate of change in both ILVs. This interaction was consistent across subjects with MCI and AD diagnoses (Figure 21 and Figure 22). Contingency tables showing sample sizes by genotype

combination are presented in Table 13, and contingency tables by diagnosis status are shown in Table 14.

Table 14 Contingency tables for SNP-SNP interaction between *SYNJ2* and *PI4KA* for association study with longitudinal inferior lateral ventricle volume change.

NC: Normal Control; MCI: Mild Cognitive Impairment; AD: Alzheimer's Disease. Cells represent count, or number of subjects in each category.

		Diagnosis					
		NC		MCI		AD	
		rs9295289 SYNJ2					
		Minor Allele Absent	Minor Allele Present	Minor Allele Absent	Minor Allele Present	Minor Allele Absent	Minor Allele Present
PI4KA rs178051	Minor Allele Absent	148	15	147	14	257	32
	Minor Allele Present	23	1	29	1	55	7

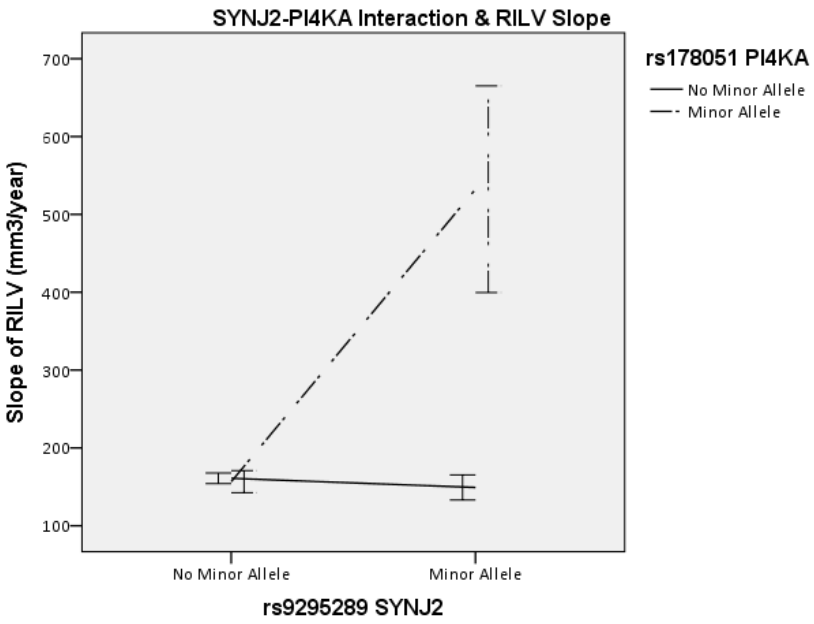

Figure 19: Effect of *SYNJ2* and *PI4KA* interaction on right inferior lateral ventricle volume change. The model included volume change as the outcome variable, and SNP effects and SNPxSNP interactions, and covariates of baseline age, sex, education in years, *APOE* status, and diagnosis. $p = 9.13 \times 10^{-12}$. Contingency tables showing sample sizes by genotype combination are presented in Table 13.

Bars represent one standard error.

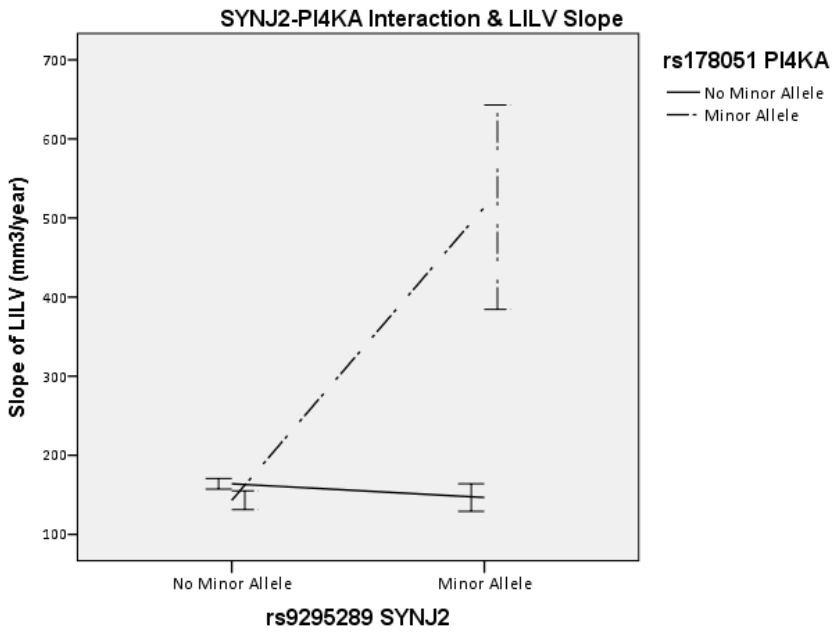

Figure 20: Effect of *SYNJ2* and *PI4KA* interaction on left inferior lateral ventricle volume change. The model included volume change as the outcome variable, and SNP effects and SNPxSNP interactions, and covariates of baseline age, sex, education in years, *APOE* status, and diagnosis. $p = 8.17 \times 10^{-13}$. Contingency tables showing sample sizes by genotype combination are presented in Table 13.

Bars represent one standard error.

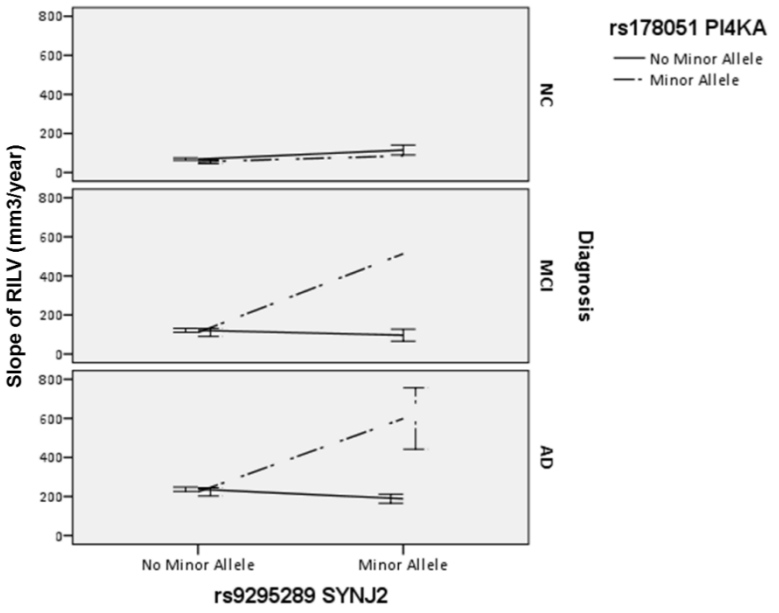

Figure 21: Effect of *SYNJ2* and *PI4KA* interaction on right inferior lateral ventricle volume change across diagnoses. The model included volume change as the outcome variable, and SNP effects and SNPxSNP interactions, and covariates of baseline age, sex, education in years, *APOE* status, and diagnosis. $p = 9.13 \times 10^{-12}$. Contingency tables by diagnosis status are shown in Table 14.

Table 14.

Bars represent one standard error.

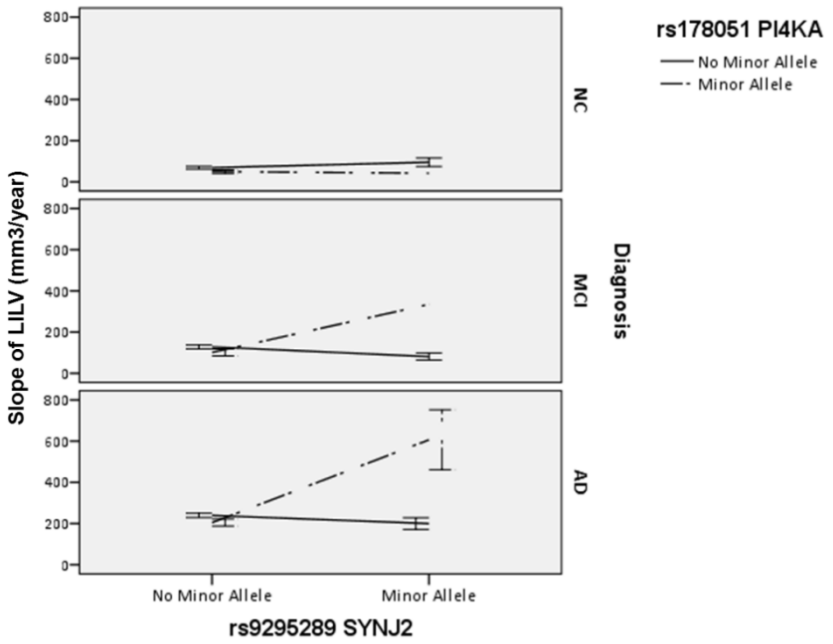

Figure 22: Effect of *SYNJ2* and *PI4KA* interaction on left inferior lateral ventricle volume change across diagnoses. The model included volume change as the outcome variable, and SNP effects and SNPxSNP interactions, and covariates of baseline age, sex, education in years, *APOE* status, and diagnosis. $p = 8.17 \times 10^{-13}$. Contingency tables by diagnosis status are shown in Table 14.

Table 14.

Bars represent one standard error.

The *PDE3A*- *ABHD12B* interaction that was significantly associated at the Bonferroni-corrected level with change in the RILV did not pass Bonferroni correction in the LILV ($p=1.59 \times 10^{-8}$). The other SNP-SNP interactions associated with the RILV did not show a strong trend in the LILV. Full results can be seen in Table 15. As a post-hoc analysis, we examined the effect of the significant interactions between *SYNJ2-PI4KA***,** *PARD3*-

MYH2, *PDE3A- ABHD12B*, and *OR2L13-PRKG1* on the average volume of RILV and LILV combined ($p=1.52x10^{-13}$, $3.49x10^{-8}$, $1.34x10^{-10}$, $1.85x10^{-7}$, respectively, Table 22).

Table 15 Full results with Bonferroni corrected significant SNP-SNP interactions for genetic interaction association with longitudinal inferior lateral ventricle volume change. 130,512,955 interactions were tested, leading to a threshold of $p < 3.83x10^{-10}$.

	Gene 1			Gene 2			Interaction Term		
ROI	SNP	Gene	Main Effect p-value	SNP	Gene	Main Effect p-value	p-value	R^2	t
RILV	**rs9295289**	***SYNJ2***	**0.10**	**rs178051**	***PI4KA***	**0.04**	**9.10E-12**	**0.04**	**7**
	rs11596284	*PARD3*	0.30	rs3744566	*MYH2*	0.89	3.20E-10	0.04	6
	rs11614805	*PDE3A*	0.78	rs7154732	*ABHD12B*	0.91	3.60E-10	0.04	6
	rs11590865	*OR2L13*	0.01	rs1922127	*PRKG1*	0.19	3.60E-10	0.04	6
LILV	**rs9295289**	***SYNJ2***	**0.14**	**rs178051**	***PI4KA***	**0.34**	**8.20E-13**	**0.05**	**7**

ROI: region of interest. RILV: Right inferior lateral ventricle. LILV: Left inferior lateral ventricle. Chr: Chromosome. SNP: reference SNP number of first SNP in SNP-SNP pair. Gene: gene corresponding to SNP. Main Effect p-value: Main effect of SNP on ROI. P-value: nominal p value. R^2= R^2 for full model –R^2 for reduced model (without interaction term). t: t-statistic for interaction term. Bolded interaction was significant at Bonferroni corrected levels in both the RILV and LILV

Discussion

In this study, we focused on the ILVs, which are used frequently as a source of quantitative endophenotypes for LOAD [48–50,162], and we limited hypothesis testing to SNP-SNP pairs within KEGG pathways. Our quantitative trait and pathway-based interaction analysis yielded several interesting candidate gene-gene interactions, one of which was significantly associated with change in both the right and left ILV. Using existing biological knowledge, we were able to deduce a plausible biological context for these significant interactions.

The SNP-SNP interaction rs9295289-rs178051 are both intronic to the genes *SYNJ2* and*PI4KA*, respectively, and have minor allele frequencies of 9.6% and 15.9%, respectively. The interaction was significantly associated with change in the RILV and LILV, and with the average rate of change in the combined ILV. Below we present evidence suggesting that the biological mechanism for this statistical interaction may involve the perturbation of the phosphatidylinositol (PI) signaling system that results in a down-regulation of the Akt cell survival pathway, resulting in decreased neuronal survival as reflected by increased volume of the ventricles.

Both *SYNJ2* and *PI4KA* are involved in the synthesis of 1-Phosphatidyl-1D-*myo*-inositol-4P (PIP) (Figure 23). *SYNJ2* (MIM: 609410) encodes synaptojanin-2, which is a ubiquitously expressed inositol polyphosphate 5-phosphatase that dephosphorylates 1-Phosphatidyl-1D-*myo*-inositol-4,5P_2 (PI-4,5P_2) to PIP, and *PI4KA* (MIM: 600286) encodes PI 4-kinase, which phosphorylates phosphatidylinositol (PI) to PIP (Figure 23).

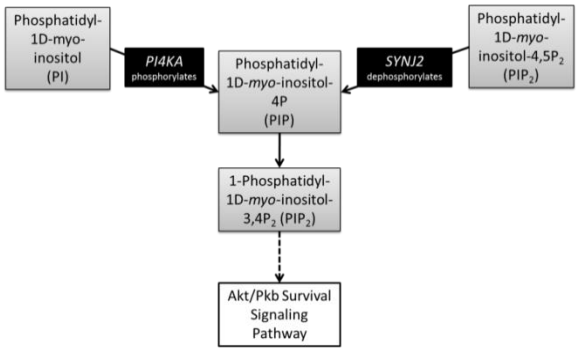

Figure 23: Phosphatidylinositol and Akt/PKB Survival Signaling Pathway.

Adapted from the KEGG Phosphatidylinositol signaling system (hsa04070, found at http://www.genome.jp/dbget-bin/www_bget?hsa04070)

In multiple cohorts, PIP levels were observed to be reduced in the temporal cortices of patients with LOAD [163,164]. Further, PI kinase activity was decreased while PIP kinase activity remained stable, suggesting that PI kinases, like that encoded by *PI4KA*, have a specific functional relevance to LOAD [163,165]. PIP is important because it can be phosphorylated to form 1-Phosphatidyl-1D-*myo*-inositol-3,4P_2 (PI-3,4P_2), which activates the protein Akt, also known as Protein Kinase B (PKB) [166]. Akt/PKB has proliferative and anti-apoptotic cell response function [166] and regulates neuronal survival [167], protect from the neurotoxic effects of AD associated amyloid beta protein [168], and mediate neuronal cell death when its activation is inhibited [169]. Thus, a decrease in PIP synthesis could disrupt a vital mechanism of neuroprotection. Variation in either *SYNJ2* or *PI4KA* might modulate the efficiency of PIP synthesis, but perhaps disruption of both routes of PIP synthesis is required to have detrimental effects seen in our study as increased ventricle dilation.

Evidence that *PI4KA* is involved in LOAD derives primarily from its role in the synthesis of PIP. However, there is some additional literature linking *SYNJ2* to cognitive function, which would lend further support for a role in Alzheimer disease. The protein

synaptojanin-2 is localized at nerve terminals in the brain [170]. The gene is differentially expressed in hippocampal sub-regions of the marmoset primate [171] and shows decreased expression in the human temporal cortex in persons with major depressive disorder [172]. *SYNJ2* has been associated with cognitive abilities in two independent elderly cohorts [173]. Finally, haploinsufficiency of *SYNJ2* due to a microdeletion on 6q is associated with a syndrome that presents with microencephaly, developmental delay and agenesis of the corpus callosum [174].

Thus, the genetic interactions associated with ILV atrophy rate in this study may be mapping variants in *SYNJ2* and *PI4KA* that interact to decrease synthesis of PIP and its phosphorylated form (PI-3,4P_2), which is required for activation of the neuroprotective, Akt-mediated, cell survival signaling pathway.

Conclusions

In conclusion, by using a pathway based approach, we identified four SNP-SNP interactions significantly associated with AD related quantitative endophenotypes, one of which was significantly associated with bilateral volume change of the inferior lateral ventricles. Focusing on this interaction, we used existing biological knowledge of within-pathway interactions and proposed a plausible biological context for this statistical interaction, which suggests that volume change in the LOAD brain might be mediated by alterations of the inositol signaling pathway, leading to deficits in neuroprotective mechanisms.

The most common variable selection strategy for interaction studies only selects SNPs with main effects to test for interactions. It is important to emphasize that such an

approach would not have discovered any of the Bonferroni-significant interactions presented here, highlighting the strength of the pathway-based approach we took.

The present results must be interpreted within the framework of our statistical models. In all cases, we included covariates related to disease status and progression including age, sex, education, diagnosis and *APOE* status. Thus, all significant interactions are explaining variance beyond known predictors of risk, and while the contributions of these interactions appear to be meaningful, the implications should not be extended without considering the variance accounted for by the other factors in our model. The interactions in this study represent dominant effects (carriers versus non-carriers), and the results were interpreted accordingly. Because of the sheer number of tests, we were not able to curate the number of other interactions mapping to the gene-gene interaction between *SYNJ2* and *PI4KA* that did not reach Bonferroni significance.

In the future, the interactions found in this study should be replicated in independent datasets to confirm the SNP-SNP associations. Furthermore, functional analyses could help clarify the basis of these statistical genetic interactions and provide greater specificity for identification of targets for clinical intervention or diagnosis. Further molecular studies on the relationship between *SYNJ2* and *PI4KA* and the PI / PI-3,4P_2 / Akt balance are warranted to draw definite conclusions about the relationship between risk variants in *SYNJ2* and *PI4KA* causing downstream decreases in PI-3,4P_2, Akt mediated cell survival signaling and, ultimately, increased neurodegeneration.

We limited our studies to interactions within pathways, but interactions between genes across pathways may be related to disease risk as well and warrant further exploration. By using KEGG pathways, we also biased our results toward mechanisms that are well-studied. As a result, there may be other novel interactions in other realms of biology that

this strategy did not discover. While the sample size utilized in this study is considered large for imaging studies, it is still modest compared with most case-control genetic association studies being conducted at this time, and this is a limitation of the current study as well. We advocate for similar analyses in other complex neurological or neuropsychiatric disorders to improve our understanding of the mechanisms underlying genetic risk for disease. We continued to explore this using other endophenotypes from imaging modalities in the following chapter.

Supporting Information

Example code used in this analysis is available in Appendix C.

Chapter 5

GENETIC INTERACTIONS FOUND BETWEEN CALCIUM CHANNEL GENES MODULATE AMYLOID LOAD MEASURED BY POSITRON EMISSION TOMOGRAPHY

Adapted from:

Koran ME, Hohman TJ, Thornton-Wells TA. Genetic interactions found between calcium channel genes modulate amyloid load measured by positron emission tomography. Human Genetics. In Press.

Introduction

The complex genetic etiology of late onset Alzheimer's disease (LOAD) has proven difficult to unravel, with the most significant ten genes associated with LOAD explaining only 35% of the variability in disease risk [11]. For complex diseases like LOAD, it is imperative that we look beyond single marker analyses to explore biologically-plausible interactions and that we address the considerable heterogeneity present in disease status information by using meaningful intermediate phenotypes. In this study, we investigate the influence of interactions between genes previously associated with Alzheimer's Disease (AD) on amyloid beta load in an effort to better understand the genetic etiology of amyloid beta deposition and, by extension, risk for LOAD.

Previous gene-gene interaction studies in LOAD have implicated interactions between: *CR1* and *APOE* using quantified amyloid beta Positron Emission Tomography (PET) as

the outcome variable [81]; and between cholesterol trafficking genes (Rodríguez-Rodríguez et al. 2009; 2010), and tau phosphorylation genes (Mateo et al. 2009) in case-control analyses. These studies indicate the important information that can be garnered from investigating higher order genetic relationships in complex diseases like LOAD. The current study aims to conduct a more comprehensive analysis of gene-gene interactions between variants associated with AD risk, while leveraging quantitative measurements of AD-associated neuropathology, which can increase statistical power [64]. For brain-based diseases, quantitative data can be derived from neuroimaging, such as PET. PET imaging can be used to quantify levels of amyloid in the brain by utilizing a radiotracer such as florbetapir (^{18}F-AV-45 or AV-45) or and Pittsburgh Compound-B (PiB, *N*-methyl-[^{11}C]2-(4′-methylaminophenyl)-6-hydroxybenzothiazole). These tracers selectively bind to amyloid beta in living patients, have been correlated with disease onset and progression, have been validated post-mortem, and have been included as biomarkers for classifying patients with AD in research studies [53–56].

Genetic interaction studies are prone to the problem of over fitting, which can result in spurious associations that are not replicated in independent datasets. This problem is exaggerated when large-scale (e.g., genome-wide) explorations are conducted, since the number of false positive findings is greatly increased. However, by focusing on interactions between genes known to be involved in disease-related biological processes, one can maximize *a priori* biological plausibility and post-hoc interpretability while reducing the multiple testing correction threshold and computational burden [175]. Because of the smaller number of subjects in ADNI with PET scans versus MRI studied in the previous chapter, only interactions between genes from the AD pathway of the Kyoto Encyclopedia of Genes and Genomes (KEGG) database were investigated. The AD KEGG pathway (hsa05010) includes genes related to amyloid and tau processing,

apoptosis, mitochondrial dysfunction, free radical production, and calcium homeostasis (http://www.genome.jp/kegg/pathway/hsa/hsa05010.html).

Though this study had relatively smaller sample size compared to the previous study outlined in chapter 4, in this study, there were multiple cohorts of subjects with PET scans and therefore, we were able to attempt to replicate any interactions discovered. Replication is a challenge for genetic interaction analysis because the biological "unit" or level at which one tries to replicate or validate findings is debatable. Attempts to replicate at the SNP level are rife with problems unrelated to verification of a true biological effect [176]. SNP-level replication is problematic largely due to the fact that most genotyped SNPs are not functional and are merely tagging a putative functional element. Differences in linkage disequilibrium patterns across samples from a single population can result in variable efficiency of tag SNPs and even reverse directionality of effects, wherein a tag SNP is in linkage disequilibrium to the risk allele in one sample but the reference or protective allele in another sample [176]. Likewise, allelic heterogeneity, in which multiple SNPs in a gene have a similar effect, can result in reduced statistical power and a failure to confirm an association with any particular SNP, even when all are associated with the disease of interest [176]. Indeed, since SNPs generally exert their effects either by altering the structure of a protein, the probability of transcription, or the efficiency of translation, their biological relevance is properly interpreted at the gene level (i.e., whether a protein is functional, whether it is present in deficient or excessive levels, etc.) as long as the proper annotation between SNP and gene is made. Thus, in this study, we use a gene-based approach to validate significant interactions from the discovery set in two additional independent datasets. A similar replication approach was previously successful in validating a novel gene-gene interaction underlying high density lipoprotein cholesterol [143,145].

Methods

Data used in the preparation of this article were obtained from the ADNI database (adni.loni.ucla.edu) as described previously in chapter 4.

Subjects

Participants were enrolled based on the criteria outlined in the ADNI protocols (http://www.adni-info.org/Scientists/AboutADNI.aspx; http://adni.loni.ucla.edu/wp-content/uploads/2008/07/ADNI2_Protocol_FINAL_20100917.pdf; http://adni.loni.ucla.edu/wp-content/uploads/2008/07/ADNI_Go_Protocol.pdf). Only subjects in the ADNI cohorts who had both genotype data and either PiB or AV-45 PET scans and were Caucasian (in order to minimize population stratification) were included in analyses. Subjects from ADNI-1 with AV-45 PET imaging data were included in the discovery data set. The Stage 1 validation dataset included subjects from ADNI-GO and ADNI-2 with AV-45 PET imaging data, excluding all participants who were also present in the discovery dataset. The Stage 2 validation dataset included subjects from ADNI-1 with PiB PET imaging data, while excluding subjects from either of the previous two datasets. Demographic data are presented in Table 16.

Table 16 Demographic data for genetic interaction association with PET amyloid load

Discovery Dataset	Clinical Diagnosis		
	Normal Control[#]	Mild Cognitive Impairment[#]	Alzheimer's Disease[#]
Number of Patients	67	53	43
Number of APOE-4 Carriers	14	17	28
Number of Females	33	16	15
Mean Baseline Age *(SD[*])*	76.52 *(5.171)*	74.92 *(7.372)*	72.70 *(6.383)*
Mean Years of Education *(SD[*])*	16.10 *(3.036)*	15.58 *(3.207)*	16.02 *(2.866)*
Mean AV-45 SUVR[**] *(SD[*])*	1.22 *(0.188)*	1.35 *(0.288)*	1.47 *(0.270)*
Stage 1 Validation Dataset			
Number of Patients	110	223	40
Number of APOE-4 Carriers	28	90	29
Number of Females	56	94	15
Mean Baseline Age *(SD[*])*	74.03 *(5.725)*	72.10 *(7.445)*	73.10 *(9.342)*
Mean Years of Education *(SD[*])*	16.42 *(2.579)*	16.12 *(2.658)*	15.53 *(2.641)*
Mean AV-45 SUVR[**] *(SD[*])*	1.28 *(0.237)*	1.35 *(0.251)*	1.54 *(0.225)*
Stage 2 Validation Dataset			
Number of Patients	17	59	19
Number of APOE-4 Carriers	4	34	11
Number of Females	6	19	7
Mean Baseline Age *(SD[*])*	77.59 (*5.161*)	75.97 *(8.049)*	73.47 *(8.746)*
Mean Years of Education *(SD[*])*	15.65 *(2.668)*	16.14 *(2.726)*	15.00 *(2.828)*
Mean PiB SUVR[**] *(SD[*])*	1.56 *(0.355)*	1.81 *(0.368)*	1.88 *(0.305)*

* SD – standard deviation

** SUVR - Standardized uptake value ratio normalized composite score for amyloid tracer

Normal Control subjects had a Mini-Mental Status Examination (MMSE) score between 24 and 30, a Clinical Dementia Rating (CDR) score of 0, and were not depressed (Geriatric Depression Scale score < 6).

Mild Cognitive Impairment subjects had a MMSE score between 24 and 30; objective memory impairment, subjective memory impairment, and a CDR score of 0.5.

Alzheimer's Disease subjects met clinical criteria for dementia, had an MMSE of between 20 and 26, and had CDR score of .5 or 1.

Genotyping

Genotyping in the ADNI-1 discovery dataset was performed using the Illumina Infinium Human-610-Quad BeadChip. Quality control (QC) was performed using PLINK software

(version 1.07; [150]) as described in chapter 4, excluding SNPs with a genotyping efficiency < 95%, out of Hardy Weinberg Equilibrium ($p<1x10^{-6}$), or with a minor allele frequency (MAF) of < 5%. Subjects were excluded if they had a genotyping call rate < 95%, if there was a reported-versus-genetic sex inconsistency, or if relatedness with another subject was established (PI_HAT > 0.5). After QC, 515,839 SNPs and 163 subjects remained available for discovery analyses. For the Stage 1 validation dataset, DNA samples from ADNI-GO and ADNI-2 were genotyped on the Illumina HumanOmni1-Quadv1 array. QC was performed in PLINK with the same criteria as the discovery data set, resulting in 605,317 SNPs and 373 subjects available for validation analyses. Genotyping on the subjects included in the Stage 2 validation dataset was performed using the Illumina Infinium Human-610-Quad BeadChip and the same QC measures were applied (leaving 95 subjects and 515,839 SNPs).

Effects of interactions on amyloid deposition

Quantification of amyloid deposition

Amyloid deposition was quantified using the AV-45 or PiB tracers. Methods relating to PiB data acquisition and calculation have been extensively described [177,178], as have methods relating to AV-45 data acquisition [179]. In summary, for both datasets, Standardized Uptake Value Ratio (SUVR) images were normalized to the cerebellum (PiB) or cerebellar gray matter (AV-45) and co-registered to the subject-specific T1-weighted structural MRI images. A composite score was calculated as the mean normalized SUVR across the anterior cingulate, frontal, lateral temporal, middle temporal, parietal, precuneus, and occipital cortices (PiB) and the cingulate (anterior and

posterior), frontal, lateral temporal, middle temporal, and lateral parietal (including the precuneus and supramarginal gyrus) cortices (AV-45). These regions were parcellated using FreeSurfer image analysis suite [153]. The composite score for each subject was used as the outcome measure of amyloid deposition in all three analyses.

SNP-SNP interaction analysis: Discovery

Genotype data that passed QC were analyzed in an interaction analysis using the publicly available InterSNP program v1.0.10 [156]. We tested the hypothesis that gene-gene interactions explain variance in amyloid pathology beyond variance related to age, sex, education, disease status, and *APOE* genotype. Only SNPs that were in a gene in the AD KEGG Pathway were analyzed, and only interactions between (not within) genes were tested. To maximize post-hoc biological interpretability, only SNPs that were in a 5' untranslated region (UTR), 3' UTR, intron, or exon of a gene (annotated using the product support files available for download at Illumina.com) were included. 1196 SNPs that mapped to 43 genes were available in the discovery dataset (

Table 17). Across all possible gene-gene pairs from the AD KEGG Pathway, 634,864 SNP-SNP interactions were tested. All SNPs were modeled as binary variables (minor allele absent or present) to attenuate the problem of data sparsity commonly confronted in interaction analyses. The outcome measure was the composite mean normalized SUVR (as described above). The covariates included were: baseline age in years, last diagnosis recorded as of the January 2013 data release (1= Normal, 2=MCI, 3=AD), education in years, sex, and *APOE* status (number of $\varepsilon 4$ risk alleles). SNP-SNP interaction effects were explored using a genotypic model and a linear regression framework for quantitative traits [156]. Interactions were considered of interest if their p-value exceeded a moderate threshold of $\alpha < 5x10^{-6}$. A t-test statistic and R^2 effect size for each SNP-SNP interaction of interest were calculated in SPSS (http://www-01.ibm.com/software/analytics/spss/) using the same covariate, phenotype, and genotype files as used in InterSNP. Effects were plotted in SPSS as well.

Table 17 Genes included in discovery dataset of the genetic interaction association with PET amyloid load.

Chr: Chromosome number. # of SNPs: Number of SNPs tested per gene.

Gene	Chr	# of SNPs
ATF6	1	55
CALML6	1	5
CASP9	1	21
NCSTN	1	18
CASP8	2	24
EIF2AK3	2	18
IL1B	2	7
GSK3B	3	30
ITPR1	3	345
MME	3	69
CASP3	4	20
SNCA	4	40
TNF	6	19
CDK5	7	6
CYCS	7	9
LPL	8	38
GNAQ	9	91
GRIN1	9	14
CASP7	10	30
FAS	10	34
IDE	10	36
APBB1	11	19
BACE1	11	20
BAD	11	13
CAPN1	11	22
FADD	11	3
APAF1	12	30
CACNA1C	12	478
LRP1	12	41
NOS1	12	117
PSEN1	14	20
ADAM10	15	55
CHP	15	22
RYR3	15	623
ATP2A1	16	12
NAE1	16	6
ERN1	17	39
MAPT	17	31
APOE	19	3
PLCB1	20	539
APP	21	125
BID	22	40
MAPK1	22	43

SNP-SNP interaction analysis: Stage 1 Validation

We used gene-based replication strategy in our subsequent validation analyses (Neale and Sham, 2004), such that only gene-gene pairs represented in significant interactions from discovery analyses were tested in the first validation set. In order to further reduce multiple testing, within each gene, we selected only independent SNPs using LD pruning implemented in PLINK with an r^2 threshold of 0.6 (--indep-pairwise 50 5 .6), resulting in 31,068 total SNP-SNP tests. Pairwise LD was calculated with SNAP (SNP Annotation and Proxy Search, available at http://www.broadinstitute.org/mpg/snap/) using data from the European (CEU) population in 1000 Genomes Pilot 1. We used a conservative Bonferroni correction for gene-level multiple comparisons based on the number of SNP-SNP interactions tested within each gene-gene pair. SPSS was used to calculate the t-test statistic and R^2 effect size and to plot the effects.

SNP-SNP interaction analysis: Stage 2 Validation

Further validation of the gene-gene interaction was conducted in a post hoc analysis. We tested the SNPs that passed correction in the discovery and Stage 1 validation datasets that corresponded to the gene-gene interaction validated in Stage 1. Interactions between the SNPs were tested in SPSS using the identical model with the same covariates as in the previous analyses with PiB SUVR measure as the outcome variable. A conservative Bonferroni correction for the 4 SNP-SNP interactions tested was employed ($p < 0.0125$). SPSS was used to calculate the t-test statistic and R^2 effect size and to plot the effects of these interactions as well.

Results

Discovery Dataset

The model we tested included the major AD risk factors of age, sex, education, diagnosis, and *APOE* status, such that all significant interaction terms explained additional variance beyond these strong risk factors. Six SNP-SNP pairs that mapped to four gene-gene interactions were noted of interest at $\alpha < 5x10^{-6}$: *CACNA1C-ATF6* (2 SNP-SNP interactions), *NOS1-GNAQ* (1 SNP-SNP interaction), *PLCB1-CACNA1C* (2 SNP-SNP interactions), and *RYR3-CACNA1C* (1 SNP-SNP interaction). All main effects for these SNPs were not significant ($p > 0.05$).

Stage 1 Validation Dataset

All SNP-SNP pairs that mapped to the four gene-gene interactions found in discovery were tested in the Stage 1 validation data set (31,068 total independent tests: *CACNA1C-ATF6* (1,010 tests), *NOS1-GNAQ* (364 tests), *PLCB1-CACNA1C* (12,019 tests), and *RYR3-CACNA1C* (17,675 tests)). One SNP-SNP interaction mapping to *RYR3-CACNA1C* was significant after Bonferroni correction (Table 18). The effect of this interaction was in the same direction for both discovery and Stage 1 validation (Table 18, $\beta_{discovery} = 0.43$ and $\beta_{validation} = 0.25$), and as seen in Figure 24, Figure 25, and Figure 26. In both the discovery and Stage 1 validation interaction models, a minor allele in both genes corresponded to higher amyloid load (Figure 24, Figure 25, Figure 26) versus a minor allele in only one or none of the genes. This interaction explained 9% and 4% of

the variance in amyloid load in the discovery and Stage 1 validation datasets, respectively.

Stage 2 Validation Dataset

The four SNPs mapping to *RYR3-CACNA1C* from the discovery and Stage 1 validation datasets were tested for interactions in the Stage 2 validation dataset (4 total independent tests, Table 19; gene mapping can be seen in Table 23). None of these SNPs were in strong LD with each other (using a threshold of r^2>0.6). One SNP-SNP interaction (rs16972835-rs7132154) was significant after Bonferroni correction (p=0.0077, Table 18). The effect of this interaction was in the same direction as the interactions found in the Discovery and Stage 1 validation (Table 18, $\beta_{discovery}$ = 0.43, $\beta_{Stage1\text{-}validation}$ = 0.25, $\beta_{Stage2\text{-}validation}$= 0.45), and as seen in Figure 24, Figure 25, and Figure 26, in all three datasets, a minor allele in both genes corresponded to higher amyloid load versus a minor allele in only one or none of the genes. This interaction explained 6% of the variance in amyloid load in the Stage 2 validation dataset (Table 18).

Table 18 Significant SNP-SNP Interactions in *RYR3-CACNA1C* from discovery and validation analyses from genetic interaction association with PET amyloid load

					Main Effect		Interaction Term		
	N	Gene	SNP	MAF†	β#	P*	β#	$R^{2\,\#\#}$	p*
Discovery	163	RYR3	rs16972835	0.09	-0.12	0.04	0.43	0.09	2.49E-06
		CACNA1C	rs2302729	0.17	-0.06	0.14			
Stage 1 Validation	373	RYR3	rs12901404	0.14	-0.06	0.05	0.25	0.04	2.22E-06
		CACNA1C	rs7132154	0.21	-0.08	0.003			
Stage 2 Validation	95	RYR3	rs16972835	0.12	-0.13	0.21	0.45	0.06	7.70E-03
		CACNA1C	rs7132154	0.25	-0.18	0.02			

† MAF: Minor Allele Frequency for each SNP#β : beta coefficient in linear regression model for SNP (in Main Effect) or SNP-SNP interaction (in Interaction Term) representing effect on amyloid deposition
* p: nominal p-value of interaction term
R2: R2 (full model) – R2 (model without interaction included)
N: number of subjects

Table 19 SNP-SNP Interactions in *RYR3-CACNA1C* from Stage 2 validation of genetic interaction association with PET amyloid load

		Validation-Stage 2				
		Main Effect		Interaction Term		
		β#	p*	β#	$R^{2\,\#\#}$	p*
RYR3	rs16972835	-0.15	0.21	0.45	0.06	7.70E-03
CACNA1C	rs7132154	-0.18	0.02			
RYR3	rs16972835	0.04	0.70	0.13	0.01	3.03E-01
CACNA1C	rs2302729	<0.01	0.99			
RYR3	rs12901404	0.13	0.24	-0.10	4.00E-03	5.11E-01
CACNA1C	rs7132154	-0.06	0.48			
RYR3	rs12901404	0.12	0.20	-0.17	0.01	3.22E-01
CACNA1C	rs2302729	0.14	0.16			

β : beta coefficient for SNP (Main Effect) or SNP-SNP interaction (Interaction Term) representing effect on amyloid deposition.
* p: nominal p-value of interaction term
R^2: R^2 (full model) – R^2 (model without interaction included)
Interactions significant at Bonferroni corrected level are highlighted

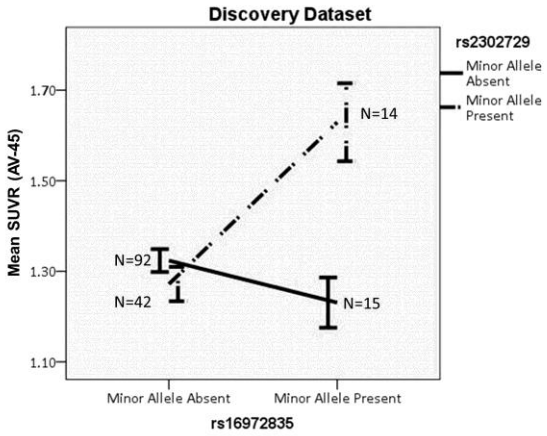

Figure 24: Discovery dataset results from study of gene-gene interactions associated with amyloid load.

Effect of *RYR3* (rs16972835) and *CACNA1C* (rs2302729) on Amyloid Deposition (measured by AV-45 ligand) in Discovery Dataset. Bars represent one standard error and N is the number of subjects in each group.

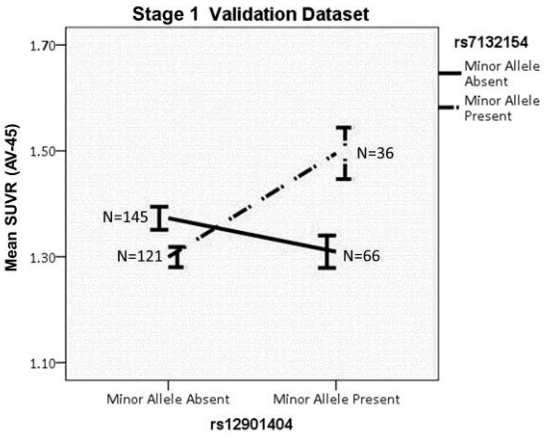

Figure 25: Stage 1 validation dataset results from study of gene-gene interactions associated with amyloid load.

Effect of *RYR3* (rs12901404) and *CACNA1C* (rs7132154) on Amyloid Deposition (measured by AV-45 ligand) in Stage 1 Validation Dataset. Bars represent one standard error and N is the number of subjects in each group.

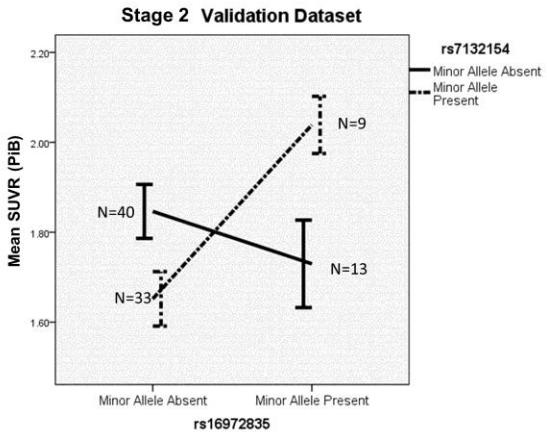

Figure 26: Stage 2 validation dataset results from study of gene-gene interactions associated with amyloid load.

Effect of RYR3 (rs16972835) and CACNA1C (rs7132154) on Amyloid Deposition (measured by PiB ligand) in Stage 2 Validation Dataset. Bars represent one standard error and N is the number of subjects in each group.

Discussion

Calcium homeostasis and its relationship to amyloidogenesis

In the present work, a genetic interaction between the *RYR3* and *CACNA1C* genes explained variance in amyloid deposition above and beyond other major known risk factors for LOAD. Such an interaction is biologically feasible given that the proteins encoded by *CACNA1C* and *RYR3* interact to maintain calcium homeostasis necessary for normal brain function [180,181] and that many studies outlined below have shown a relationship between calcium homeostasis and amyloidogenesis, whereby increased intracellular calcium levels lead to increased amyloid beta deposition. An increase in

amyloid beta is considered a key event in AD etiology (e.g., Jack et al. 2013), and calcium dysregulation is thought to assist in amyloid formation and deposition and has been hypothesized to be very important in the etiology of AD [183]. Increases in intracellular calcium increase amyloid beta production in human cell lines [184]. High levels of intracellular calcium also induce transient phosphorylation of amyloid precursor protein in neurons, leading to increased production of amyloid beta [185]. Lastly, calcium ions themselves promote the formation of neurotoxic amyloid beta oligomers *in vitro* [186]. Our findings are further strengthened by accumulating evidence that *RYR3* modulates amyloid beta plaque deposition [187–189] and that *CACNA1C* increases intracellular calcium levels in the presence of amyloid beta [190–192].

This interaction could have an important clinical application, since both proteins encoded by these two genes are calcium channels that have FDA approved channel blocking drugs and blocking either channel has been proposed as a therapy for AD pathology [193,194]. A combination of these therapies could be investigated as an enhanced approach to AD treatment.

RYR3 and *CACNA1C*

RYR3 encodes ryanodine receptor (RyR)-3, which is a receptor expressed in the brain [195] located on the endoplasmic reticulum (ER) that regulates intracellular calcium homeostasis [183]. *CACNA1C* encodes the pore-forming alpha 1C subunit of voltage-dependent L-type calcium channels (LTCCs) which are also expressed in the brain [196]. The major characteristics of this channel, including voltage-sensitivity, ion selectivity, and pharmacological responsivity to calcium channel blockers, are encoded by

CACNA1C [197]. This subunit forms a pore in the cell membrane through which calcium ions flow into the cell [197].

RYR3 in Alzheimer's Disease pathogenesis

In animal models of AD, the relationship between RyR and amyloid beta has been extensively explored. Transgenic mice which overexpress the precursor of amyloid beta (*APP*, encoding amyloid precursor protein (APP)) have increased RyR expression in their neuroblastoma cell lines [189]. Specifically, extracellular amyloid selectively increases RyR-3 (but not RyR-1 or -2) isoform expression in cortical neurons of both wild type and AD-model mice [188]. Transgenic mice that harbor human *APP* mutations have increased RyR expression in isolated cortical neurons, and this overexpression of RyR disrupts calcium homeostasis by increasing ER calcium release [189]. Furthermore, this relationship between RyR and amyloid beta is bi-directional, such that RyRs can also affect amyloid beta levels. Dantrolene is a pharmacological agent that blocks calcium release from RyR-1 and RyR-3 and has been used in cell and animal models to diminish cell death resulting from neuronal injury [194]. Interestingly, when it was used to block RyR and decrease calcium release in mouse models that either overexpressed APP or had an *APP* mutation, this decrease in calcium level reduced levels of intracellular and extracellular amyloid beta, as well as the number of amyloid beta plaques [189]. Thus, RyR-induced calcium levels seem to influence amyloid beta levels. This has also been shown in human cell lines: in human neuroglioma and embryonic cell lines transfected with *APP*, amyloid beta production increased as levels of intracellular calcium increased and RyR-mediated calcium release increased [184,198]. In summary, the existing literature indicates that there is a bi-directional relationship between RyR and amyloid beta, such

that increased amyloid beta has been associated with increased RyR expression, and RyR-driven calcium release has been associated with increased amyloid beta levels.

CACNA1C in Alzheimer's Disease pathogenesis

CACNA1C encodes the pore-forming subunit of voltage-dependent LTCCs. Its role in AD etiology can be better understood through its relationship with amyloid beta and its effects on calcium dysregulation. In rat cortical cell lines, the presence of amyloid beta increased calcium uptake by LTCCs by almost two-fold [190]. In human cerebral cortical cell lines, amyloid beta destabilized neuronal calcium regulation and rendered neurons more vulnerable to environmental stimuli that elevate intracellular calcium levels [191]. Up-regulation of the expression of *CACNA1C* was observed in human neuroblastoma cell lines after treatment with amyloid beta [193], and amyloid beta promotes the insertion of the subunit encoded by *CACNA1C* into the plasma membrane [192]. In summary, amyloid beta modulates LTCC function to increase intracellular calcium and as described above, this increase in intracellular calcium can further increase amyloid beta production and deposition.

RYR3-CACNA1C interaction and amyloid load

Both of the products of *RYR3* and *CACNA1C* have a relationship with cellular amyloid beta. These products physically interact with each other: in a study of cerebellar granule cells, RyRs and LTCCs are functionally coupled, with RyRs controlling the activity of LTCCs [199]. In a separate study in *in vitro* rat neuronal cell lines, immunoprecipitation revealed an association between LTCCs and RyRs, and immunohistochemistry confirmed the co-localization of LTCC and RyR clusters on axons [181]. In that same study,

depolarization sensed by LTCCs activated RyRs, which caused the release of toxic levels of calcium [181]. This interaction was also demonstrated in a study of rat hippocampal tissue, where a physical interaction between the N-terminus of the LTCC and the N-terminus of a RyR was observed [180]. Finally, an interaction between RyRs and LTCCs has been observed in cardiac and skeletal muscle, where these proteins are also expressed [200,201].

With the evidence of physical interaction between the RyR and LTCC proteins and the evidence outlined above relating RyR, LTCC, calcium release, and amyloid beta to each other, the statistical genetic interaction we report herein might be reflective of causal variants in *RYR3* and *CACNA1C* interacting to cause disruption of calcium homeostasis and to increase intracellular calcium levels leading to increased amyloid beta production and deposition as detected by PET.

Conclusion

In this study, we have explored the relationship between genes within the AD pathway and their relationships to amyloid beta plaque levels in humans. We found evidence for a statistical association between calcium dysregulation and amyloid beta deposition as detected by PET amyloid imaging. In light of prior studies associating the products of *RYR3* and *CACNA1C* with each other and with AD pathology, this result is certainly biologically plausible. This interaction is of particular clinical significance because pharmacological manipulation of the two channels involved is feasible for future AD treatment. Combined therapy, using LTCC- and RyR-blockers, could first be tested in cell lines and animal models to determine its effect on amyloid beta plaque load and neuronal cell death.

Fine-mapping and functional analysis of the SNPs identified could help clarify the implications of these statistical genetic interactions and provide greater specificity when attempting to leverage these results to identify targets for clinical intervention. Because we validated our results at the gene-gene level and not the SNP-SNP level, further delving into the function of each of these SNPs or the causal variant these SNPs are tagging would be necessary to understand whether the discovery and validation models represent the same effect. For example, if each SNP increases the expression of its respective gene, we could conclude that the effect was truly replicated and that increased expression of both genes is associated with increased amyloid load (regardless of which SNP caused the over expression). In summary, the effect that each SNP has on expression level or function would have to be explored to determine true replication of effect.

The exact SNP-SNP interactions do not replicate across the samples, but we would argue (as others have) this lack of replication does not necessarily indicate a false positive result and may instead be due to one or several biological reasons [176], including allelic heterogeneity (wherein different alleles at the same locus are each responsible for increased disease risk in different subjects), differences in minor allele frequency, or differences in LD structure across samples. The power to replicate at the SNP level drops dramatically with a change in allele frequency between datasets, and there were differences in allele frequency across the three data sets used here (Table 18) [202]. Differences in LD structure across the two samples between each tag-SNP and the causal variant could cause the same high-risk allele to have different patterns of association with the marker alleles [176]. The gene-based replication approach we employed here attenuates these issues and has been proposed as the “gold standard” for replication and the “natural end point for association analysis” [176]. This is perhaps

especially important in gene-gene interaction studies where these issues are amplified. If the datasets had been genotyped on the same chip, an analysis on a combined dataset would be of interest, and would have alleviated this issue.

The present results must be interpreted within the framework of our statistical models. In all cases, we included covariates related to disease status and progression, including age, education, diagnosis, sex, and *APOE* status. Thus, all significant interactions explained variance beyond known predictors of risk, and while the contributions of these interactions appear to be meaningful, the implications should not be extended without considering the variance accounted for by the other factors in our model. The interactions in this study represent dominant effects (carriers versus non-carriers), and the results have been interpreted accordingly. We did not test mitochondrial genes in this study. This could be explored in a further analysis

Supporting Information

Example code used in this analysis is available in Appendix D

Chapter 6

CONCLUSIONS AND FUTURE DIRECTIONS

Alzheimer's Disease (AD) is a devastating, incurable, degenerative neurological disease and is the most common cause of dementia in both the general population and in patients with Down Syndrome (DS). The etiology of this disease still eludes us despite its prevalence and considerable research efforts dedicated to its discovery. The research described in the preceding chapters employed an innovative strategy combining imaging and genetic data to address three major challenges in AD research: (1) validating non-invasive biomarkers of neuropathology, (2) dis-entangling clinical heterogeneity of the disease, and (3) discovering biological interactions contributing to this disease's initiation and progression. I have investigated the use of a novel non-invasive biomarker of amyloid beta in humans (Chapter 2) and the use of T1-weighted Magnetic Resonance Imaging (MRI) to capture age related volumetric changes in brain structure in DS subjects (Chapter 3). I also have used quantitative endophenotypes to dissect clinical heterogeneity, and have directly investigated genetic interactions for their association with disease pathologies (Chapters 4 and 5).

Summary and Future Directions for Chapter 2

Validation of T1ρ Magnetic Resonance Imaging in human adults with amyloid beta plaque deposition

Prior to this research, the results from the mouse model studies of amyloid beta detected by T1ρ-weighted MRI had not been validated in human subjects. We were able to apply this sequence to patients with DS, who, due to triplication of the *APP* gene encoded on chromosome 21, have a high probability of amyloid plaque load. Though we were not able to validate its use as it was unable to distinguish DS subjects from subjects in the general population, this might indicate suboptimal optimization of the sequence parameters to accurately detect amyloid beta load. Further optimization of the sequence parameters is warranted before we can draw definitive conclusions about the ability of T1ρ to detect amyloid plaques in humans *in vivo*. This could include: 1) using more than two spin lock time values in image acquisition or 2) changing voxel size in order to allow detection of amyloid beta plaque. When computing T1ρ from the slope of the natural logarithm of signal as a function of TSL, we were not be able to rule out voxels based on r^2 value because we only had two TSL values. This would have eliminated voxels that are outliers, perhaps due to partial volume effects. Therefore in the future, using more than two TSL values in image acquisition would allow for further quality control of the images and their quantification. The voxel size of the images acquired on our human subjects may have been too large to detect the effects of amyloid beta plaque, as the voxels were over four orders of magnitude larger than those seen in the successful mouse model study. Alternative strategies for analyzing these images, including analyzing the *distribution*, or kurtosis and skewness, of T1ρ values within each region of

interest across the groups, are being investigated. Early indications suggest that the two distributions between the DS and normal control groups may be different. Furthermore, the theoretical trend for ERC values has not been well established, and discussion with faculty at the VUIIS is ongoing regarding this topic. In our results of ERC, an interesting trend may be forming, but in order to definitevely draw a conclusions, the sample size for each group must be increased to inform this discussion. In the future, this sequence could be validated on an autopsy brain of a patient with clinically diagnosed AD or an elderly individual with DS, using a study design similar to that which was performed in the mouse model [59] or in previous PET validation studies [55].

Summary and Future Directions for Chapter 3

DIFFERENCES IN AGE-RELATED EFFECTS ON BRAIN VOLUME IN DOWN SYNDROME AS COMPARED TO WILLIAMS SYNDROME AND TYPICAL DEVELOPMENT

In this chapter, we used a whole-brain region of interest approach to explore the relationship between age and MRI-derived brain volume across adults with DS, adults with another neurodevelopmental disorder (William Syndrome, WS), and adults with typical development, while incorporating cognitive data and genetic risk data in a secondary exploratory analysis of the DS cohort. We were able to validate that subjects with DS showed significant age-related effects in grey matter regions of the orbitofrontal cortex and the parietal cortex, and in the left and right inferior lateral ventricles, when compared to adults with WS. When imaging and cognitive data were combined in the DS

group, we discovered that the inferior lateral ventricles were associated with dementia rating scores. *APOE*, a risk gene for AD and brain atrophy, also showed a trend for association with regional brain volume. With the sample size currently analyzed, we were likely underpowered to detect more subtle AD-related changes. Each of these studies would benefit from a larger sample size to accurately estimate the effects. These conclusions were drawn based on cross-sectional data, and longitudinal T1-weighted MRI scans on these subjects should be acquired and analyzed in the future to determine the effect of aging on these subjects' brain volumes. Alternatively, other MRI intermediate phenotypes could be utilized in these studies including cortical thickness or density from the T1-weighted images, or phenotypes derived from other MRI sequences including FLAIR which can detect white matter disease, diffusion tensor imaging (DTI) which can give information on white matter structure, or functional MRI (fMRI), which can measure brain activity during tasks.

Summary and Future Directions for Chapter 4

GENETIC INTERACTIONS ASSOCIATED WITH LONGITUDINAL CHANGES IN VENTRICLE SIZE IN ALZHEIMER'S DISEASE

This study was the first to complete a comprehensive analysis of gene-gene interactions in relation to the dilation of the inferior lateral ventricles, with data available on a large number of subjects in the Alzheimer's Disease Neuroimaging Initiative (ADNI) cohort. We conducted a genetic interaction analysis on these existing data in order to derive

knowledge of the genetic etiology of AD and neuroatrophy, as it relates to AD and perhaps other neurodegenerative diseases.

We used a pathway based approach to identify four SNP-SNP interactions significantly associated with volume change of the inferior lateral ventricles. One SNP-SNP interaction was significantly associated with both the right and left inferior lateral ventricles, and we focused our literature review on this interaction between the *SYNJ2* and *PI4KA* genes, and based on this review, we suggested that volume change in the brain might be mediated by alterations of the inositol signaling pathway, leading to deficits in neuroprotective mechanisms.

In the future, the interactions found in this study should be tested for replication. Functional analyses are also warranted to elucidate the physiological basis of these interactions. Molecular studies on the relationship between the products of *SYNJ2* and *PI4KA* could greatly inform the relationship between these genes and increased neurodegeneration. These studies could elucidate whether variation in either *SYNJ2* or *PI4KA* might modulate the efficiency of the inositol signaling pathway, and if disruption of both enzymes is required to have detrimental effects seen in our study as increased ventricle dilation.

Summary and Future Directions for Chapter 5

Genetic Interactions Found Between Calcium Channel Genes Modulate Amyloid Load Measured by Positron Emission Tomography

Prior to this study, there had been no comprehensive analyses of gene-gene interactions in relation to quantitative measurements of amyloid beta pathology. We used Positron Emission Tomography (PET) data available on a large number of subjects in the Alzheimer's Disease Neuroimaging Initiative (ADNI) cohort and conducted a genetic interaction analysis on these existing data in order to explore genetic mechanisms behind amyloid beta deposition.

We found a statistical association between calcium dysregulation and amyloid beta deposition, specifically between the *RYR3* and *CACNA1C* calcium channel genes. Based on prior research associating the products of these two genes with each other and with AD pathology, this result is certainly biologically plausible. This interaction is of particular clinical significance because pharmacological manipulation of the two channels involved is feasible for future AD treatment. In the future, combined therapy, using calcium channel blocking drugs could first be tested in cell lines and animal models to determine its effect on amyloid beta plaque load and neuronal cell death.

Fine-mapping and functional analysis of the SNPs identified here could also be performed to clarify the implications of these statistical genetic interactions and provide greater specificity when attempting to leverage these results to identify targets for clinical intervention. Further, analysis for statistical interactions beyond those between genes in the AD KEGG pathway should be performed. For instance, we could use the same strategy from the analysis presented in Chapter 4, looking within all known pathways, or we could look at interactions between genes that arise in any pathway or between genes in the AD pathway with genes that arise in any other pathway.

In all of these instances, and in both the studies outlined in chapters 4 and 5, we limited our studies to interactions within pathways, but interactions between genes across pathways may be related to disease risk as well and warrant further exploration. It is perhaps likely that variants in genes across pathways interact as well, but these interactions have yet to be discovered. The challenge of such an analysis is largely computational and only increases the burden of correcting for multiple tests. Some possible strategies for investigating these issues are using empirical significance strategies like permutation testing or bootstrapping or investigating an *a priori* specified hypothesis to limit test number.

Conclusions

We focused our studies in imaging genetics on two amyloid based diseases, Alzheimer's Disease and Down Syndrome. We were able to draw interesting conclusions from these investigations, and we advocate for similar analyses in larger cohorts of these diseases or in other complex neurological or neuropsychiatric disorders to improve our understanding of the mechanisms underlying genetic risk for disease. There are most certainly more genetic associations to be found. Future work should use alternative strategies for discovering additional gene-gene interactions and for exploring gene-environment or even higher order (i.e. gene-gene-gene) interactions.

Appendix A

SUPPORTING INFORMATION FOR CHAPTER 2

Other images acquired/analyzed

T1 and T2

Three full brain Echo Planar T1 images were acquired in the same space as the T1ρ images, with TR = 100 ms and TE = 2.4, 2.4, 3.0 ms corresponding to images with flip angles of 15, 30, and 60 degrees respectively.

Six full brain T2 Turbo Spin-Echo pulse sequences were acquired in the same space as the T1ρ and T1 images, with TR = 2700 ms and TE = 15, 30, 45, 60, 75, and 90 ms.

The T1 and T2 images were originally included in the analysis before deciding to discard them from further analyses. Code for their analysis can be found in this appendix. Each T1 and T2 image was aligned in SPM to the first T1 and T2 image acquired, respectively, which were then all aligned to the first T1ρ image acquired. T1 was quantified by solving:

$$S(TR) = So * \alpha \frac{(1-e^{-\frac{TR}{T1}})}{(1-e^{(-\frac{TR}{T1})}*cos\alpha)} \quad (3)$$

with MATLAB code provided by VUIIS faculty, where α is the flip angle and TR is the repetition time with which each of the three images is acquired. These quantified images

were theoretically representative of T1ρ at infinite Hz, and therefore were plotted far from the collected FSL values at 2000 Hz.

T2 was quantified by solving:

$$S(TE) = So * e^{-\frac{TE}{T2}} \quad (4)$$

in SPM, where TE are the echo times with which each of the six images is acquired. Since T1ρ approaches T2 as FSL goes to 0 Hz [203] these quantified images were plotted at 0 Hz in the dispersion curve plots.

The T1 images were discarded from analysis because their quantified values drown out the signal from the quantified T1ρ images (Figure 27).

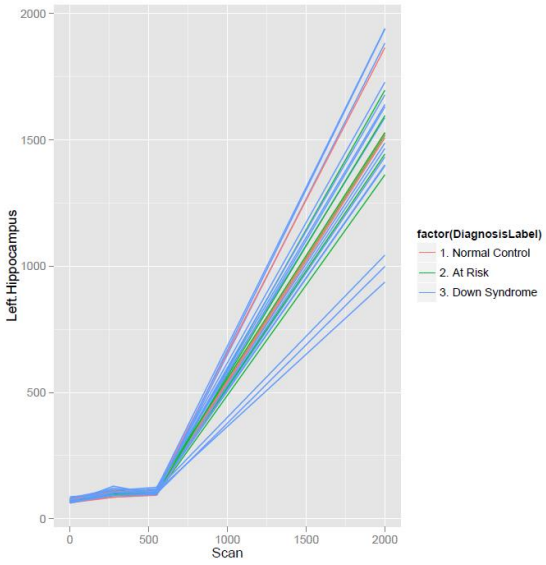

Figure 27: Dispersion curves with quantified T1 images included at 2000 Hz.

The T2 images were discontinued and replaced by T1ρ acquired with an FSL of 0 Hz. T1ρ approaches T2 as FSL goes to 0 Hz, and the results from the quantified T2 images

were distorted by inherent inhomogeneities in the MRI machine, which caused a deviation from the expected dispersion curve, where T2 was less than T1ρ (Figure 28) [203]. After inclusion of acquiring T1 at 0 Hz, the dispersion curve behaved as expected (Figure 29).

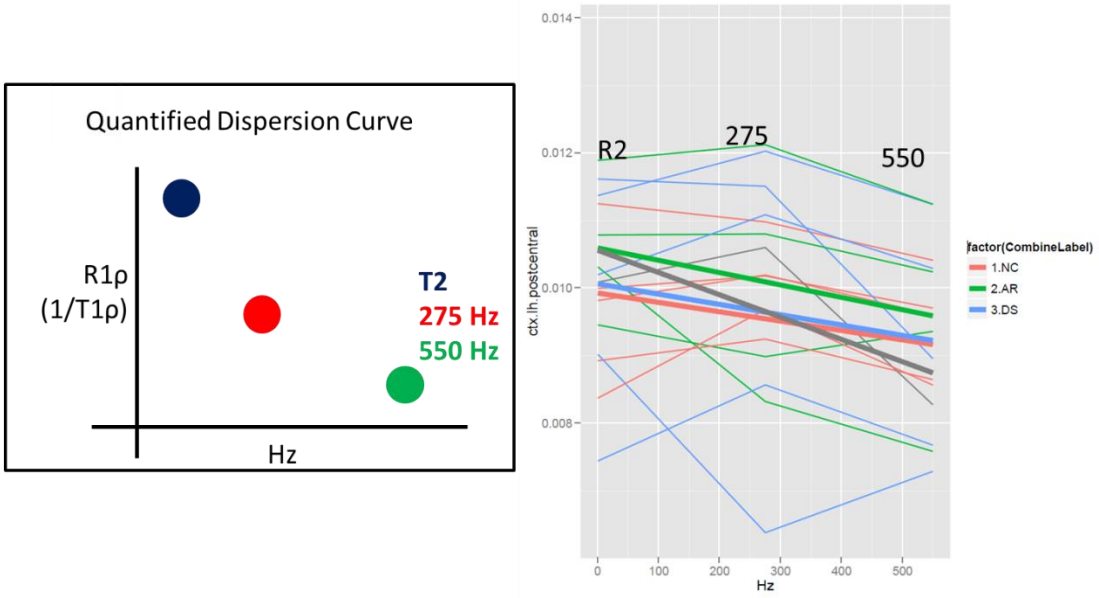

Figure 28: Example of discrepancy between expected and actual dispersion curve when R2 (1/T2) was used.

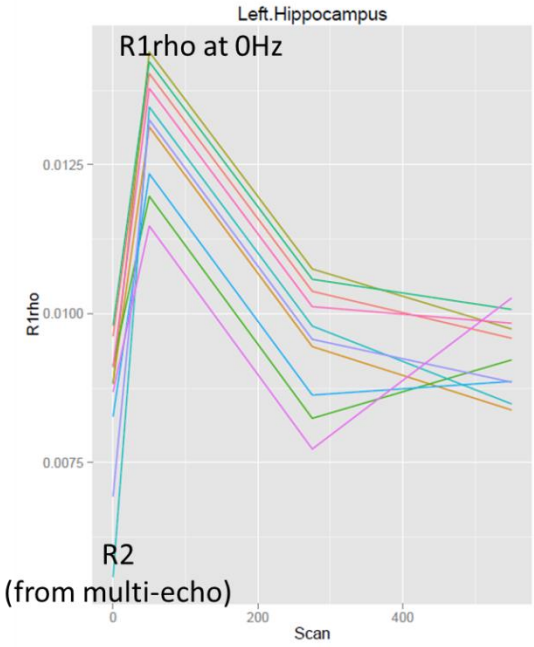

Figure 29: Dispersion curve with both R2 and R1ρ collected at 0Hz plotted.

R2 is plotted at x-axis = 0 and R1ρ (0Hz) plotted at x-axis = 50. The dispersion curve with R1ρ (0Hz) shows congruency with the expected result.

Region of Interest Based Analysis

FreeSurfer Log Creation Code

```
#!/bin/tcsh
#PBS -M mike.sivley@vanderbilt.edu
#PBS -m bae
#PBS -l walltime=48:00:00
#PBS -l mem=5000mb
#PBS -l nodes=vision.mc.vanderbilt.edu
setenv FREESURFER_HOME /usr/analysis/software/FreeSurfer_v.5.1.0
source $FREESURFER_HOME/SetUpFreeSurfer.csh
mkdir -p /projects/twells/Data/%(study)s/FreeSurfer/
setenv SUBJECTS_DIR /projects/twells/Data/%(study)s/FreeSurfer/
recon-all -i %(file)s -all -s %(scanid)s -hippo-subfields >
/projects/twells/sivleyrm/mario/log/t1w_3d_%(scanid)s_%(iter)s.lo
g
```

FreeSurfer Template and Recon-All code

```
#!/bin/tcsh
#PBS -M mike.sivley@vanderbilt.edu
#PBS -m bae
#PBS -l nodes=vision.mc.vanderbilt.edu
#PBS -l walltime=2:00:00:00
#PBS -l mem=8000mb

## Setup FreeSurfer variables
setenv FREESURFER_HOME /usr/analysis/software/FreeSurfer_v.5.1.0
source $FREESURFER_HOME/SetUpFreeSurfer.csh
setenv SUBJECTS_DIR /labs/twells/data/%(study)s/FreeSurfer
setenv ANALYSIS_DIR /labs/twells/data/%(study)s/t1rho/%(scanid)s

# Ensure the directories exist
mkdir -p $SUBJECTS_DIR
mkdir -p $ANALYSIS_DIR/275
mkdir -p $ANALYSIS_DIR/550

setenv T1W275 $ANALYSIS_DIR/275/%(t1w_filename)s
setenv T1W550 $ANALYSIS_DIR/550/%(t1w_filename)s

cp -f %(t1w_abs)s $T1W275
cp -f %(t1w_abs)s $T1W550

## Run recon-all
recon-all -i $T1W275 -all -s %(scanid)s -hippo-subfields –nowmsa
```

FreeSurfer Post-Processing and Analysis Template

```
#!/bin/tcsh
#PBS -M mike.sivley@vanderbilt.edu
#PBS -m bae
#PBS -l nodes=vision.mc.vanderbilt.edu
#PBS -l walltime=1:00:00:00
#PBS -l mem=8000mb

## Setup FreeSurfer variables
setenv FREESURFER_HOME /usr/analysis/software/FreeSurfer_v.5.1.0
source $FREESURFER_HOME/SetUpFreeSurfer.csh
setenv SUBJECTS_DIR /labs/twells/data/%(study)s/FreeSurfer
```

```
setenv ANALYSIS_DIR
/labs/twells/data/%(study)s/t1rho/%(roi_type)s/%(scanid)s/%(hz)s

# Ensure the directories exist
mkdir -p $ANALYSIS_DIR

## Setup script variables
setenv T1W      $ANALYSIS_DIR/%(t1w_filename)s
setenv T2             $ANALYSIS_DIR/%(t2_filename)s

if ( "%(roi_type)s" == "largeROI" ) then
  setenv mgzLABELFILE
          $SUBJECTS_DIR/%(scanid)s/mri/aparc.a2009s+aseg.mgz
else if ( "%(roi_type)s" == "smallROI" ) then
  setenv mgzLABELFILE $SUBJECTS_DIR/%(scanid)s/mri/aparc+aseg.mgz
endif

setenv mgzT1W_MASK    $SUBJECTS_DIR/%(scanid)s/mri/brainmask.mgz
setenv T1W_MASK
          $ANALYSIS_DIR/%(scanid)smri_convertbrainmaskRAS.nii
setenv LABELFILE
          $ANALYSIS_DIR/%(scanid)smri_convertaparc.a2009s+asegRA
S.nii
setenv rLABELFILE
          $ANALYSIS_DIR/r%(scanid)smri_convertaparc.a2009s+asegR
AS.nii
setenv T1RHO20
          $ANALYSIS_DIR/%(t1rho_20_filename)s
setenv T1RHO50
          $ANALYSIS_DIR/%(t1rho_50_filename)s
setenv T1RHO80
          $ANALYSIS_DIR/%(t1rho_80_filename)s
setenv T1RHO                    $ANALYSIS_DIR/Thornton-
Wells_%(roi_type)s_%(scanid)s_%(hz)sHz_t1-rho.nii
setenv T1FLIP15
          $ANALYSIS_DIR/%(t1_flip_15_filename)s
setenv T1FLIP30
          $ANALYSIS_DIR/%(t1_flip_30_filename)s
setenv T1FLIP60
          $ANALYSIS_DIR/%(t1_flip_60_filename)s
setenv T1                       $ANALYSIS_DIR/Thornton-
Wells_%(roi_type)s_%(scanid)s_t1.nii
setenv INVBETAIMG     $ANALYSIS_DIR/inv_beta.img
setenv MATLAB                   %(matlab)s

setenv T1rCOREGT1
          $ANALYSIS_DIR/r_T1rcoregT1%(t1rho_20_filename)s
setenv BINMULT
          $ANALYSIS_DIR/binmult_%(scanid)s.nii
```

```
setenv SEGSTAT1
          $ANALYSIS_DIR/%(scanid)s_20T1ρ_stats
setenv SEGSTAT2
          $ANALYSIS_DIR/%(scanid)s_T1xT1ρbinary_stats
setenv SEGSTAT3
          $ANALYSIS_DIR/%(scanid)s_T1_stats
setenv SEGSTAT4
          $ANALYSIS_DIR/%(scanid)s_T2beta_stats
setenv SEGSTAT5
          $ANALYSIS_DIR/%(scanid)s_T1flip_stats

## Setup log variable
setenv LOG
          $MARIO/log/t1rho_%(scanid)s_%(hz)s.log

## Copy all input images to the analysis folder

cp -f %(t1w_abs)s $T1W
cp -rf %(t2_abs)s $T2
cp -f %(t1rho_20_abs)s $T1RHO20
%(comment_50_0)scp -f %(t1rho_50_abs)s $T1RHO50
cp -f %(t1rho_80_abs)s $T1RHO80
cp -f %(t1_flip_15_abs)s $T1FLIP15
cp -f %(t1_flip_30_abs)s $T1FLIP30
cp -f %(t1_flip_60_abs)s $T1FLIP60

## Marker
echo "MRI Convert: " >> $LOG

## Run mri_convert
mri_convert --in_type mgz --out_type nii --out_orientation RAS
$mgzLABELFILE $LABELFILE
mri_convert --in_type mgz --out_type nii --out_orientation RAS
$mgzT1W_MASK $T1W_MASK

## Have to change to a directory with SPM in it.
##cd $ANALYSIS_DIR
cd %(matlab_pathdef)s

## marker
echo "T1 Rho Calculation: " >> $LOG

## ----- Start matlab ---- ##
$MATLAB -nodisplay -nodesktop -nosplash < %(t1rho_matlab)s

mri_segstats --seg $rLABELFILE --ctab
$FREESURFER_HOME/FreeSurferColorLUT.txt --empty --excludeid 0 --
sum $SEGSTAT1 --i $T1RHO
```

```
mri_segstats --seg $LABELFILE --ctab
$FREESURFER_HOME/FreeSurferColorLUT.txt --empty --excludeid 0 --
sum $SEGSTAT2 --i $BINMULT

mri_segstats --seg $mgzLABELFILE --ctab
$FREESURFER_HOME/FreeSurferColorLUT.txt --empty --excludeid 0 --
sum $SEGSTAT3 --i $mgzT1W_MASK

mri_segstats --seg $rLABELFILE --ctab
$FREESURFER_HOME/FreeSurferColorLUT.txt --empty --excludeid 0 --
sum $SEGSTAT4 --i $INVBETAIMG

mri_segstats --seg $rLABELFILE --ctab
$FREESURFER_HOME/FreeSurferColorLUT.txt --empty --excludeid 0 --
sum $SEGSTAT5 --i $T1
```

MATLAB and SPM Code for T1ρ, T1, and T2 calculation

```
try


        ANALYSIS_DIR =
'/labs/twells/data/%(study)s/t1rho/%(roi_type)s/%(scanid)s/%(hz)s';

        T1W     = strcat(ANALYSIS_DIR,'/%(t1w_filename)s');
        T2_PATH       = strcat(ANALYSIS_DIR,'/%(t2_filename)s');
        T1W_MASK  =
strcat(ANALYSIS_DIR,'/%(scanid)smri_convertbrainmaskRAS.nii');
        LABELFILE =
strcat(ANALYSIS_DIR,'/%(scanid)smri_convertaparc.a2009s+asegRAS.nii');
        T1RHO20   = strcat(ANALYSIS_DIR,'/%(t1rho_20_filename)s');
        T1RHO50   = strcat(ANALYSIS_DIR,'/%(t1rho_50_filename)s');
        T1RHO80   = strcat(ANALYSIS_DIR,'/%(t1rho_80_filename)s');
        T1RHO     = strcat(ANALYSIS_DIR,'/Thornton-
Wells_%(roi_type)s_%(scanid)s_%(hz)sHz_t1-rho.nii');
        T1FLIP15  = strcat(ANALYSIS_DIR,'/%(t1_flip_15_filename)s');
        T1FLIP30  = strcat(ANALYSIS_DIR,'/%(t1_flip_30_filename)s');
        T1FLIP60  = strcat(ANALYSIS_DIR,'/%(t1_flip_60_filename)s');
        T1      = strcat(ANALYSIS_DIR,'/Thornton-
Wells_%(roi_type)s_%(scanid)s_t1.nii');

        T1rCOREGT1 =
strcat(ANALYSIS_DIR,'/r_T1rcoregT1%(t1rho_20_filename)s');
        BINMULT   = strcat(ANALYSIS_DIR,'/binmult_%(scanid)s.nii');
        BETAIMG       = strcat(ANALYSIS_DIR,'/spm/beta_0002.img');
        INVBETAIMG= strcat(ANALYSIS_DIR,'/inv_beta.img');
```

```
%% Realign
clear matlabbatch;
spm_jobman('initcfg');
spm('defaults', 'FMRI');

matlabbatch{1}.spm.spatial.coreg.estimate.ref = {


 T1RHO20


};
matlabbatch{1}.spm.spatial.coreg.estimate.source = {


                    T1W_MASK


  };
matlabbatch{1}.spm.spatial.coreg.estimate.other = {


   LABELFILE


 };
matlabbatch{1}.spm.spatial.coreg.estimate.eoptions.cost_fun = 'nmi';
matlabbatch{1}.spm.spatial.coreg.estimate.eoptions.sep = [4 2];
matlabbatch{1}.spm.spatial.coreg.estimate.eoptions.tol = [0.02 0.02 0.02
0.001 0.001 0.001 0.01 0.01 0.01 0.001 0.001 0.001];
matlabbatch{1}.spm.spatial.coreg.estimate.eoptions.fwhm = [1 1];

matlabbatch{2}.spm.spatial.realign.estimate.data = {

                                        {

                                        T1RHO20
                                        %(comment_50_1)sT1RHO50

                                        T1RHO80
                                        }

                                       }';

matlabbatch{2}.spm.spatial.realign.estimate.eoptions.quality = 0.9;
matlabbatch{2}.spm.spatial.realign.estimate.eoptions.sep = 4;
```

```
matlabbatch{2}.spm.spatial.realign.estimate.eoptions.fwhm = 1;

matlabbatch{2}.spm.spatial.realign.estimate.eoptions.rtm = 1;

matlabbatch{2}.spm.spatial.realign.estimate.eoptions.interp = 2;
matlabbatch{2}.spm.spatial.realign.estimate.eoptions.wrap = [0 0 0];
matlabbatch{2}.spm.spatial.realign.estimate.eoptions.weight = '';

matlabbatch{3}.spm.spatial.realign.write.data = {


 T1RHO20


 LABELFILE


};
matlabbatch{3}.spm.spatial.realign.write.roptions.which = [1 0];
matlabbatch{3}.spm.spatial.realign.write.roptions.interp = 0;
matlabbatch{3}.spm.spatial.realign.write.roptions.wrap = [0 0 0];
matlabbatch{3}.spm.spatial.realign.write.roptions.mask = 1;
matlabbatch{3}.spm.spatial.realign.write.roptions.prefix = 'r';

matlabbatch{4}.spm.spatial.realign.estimate.data = {

                                        {

                                        T1FLIP15
                                        T1FLIP30
                                        }

                                       }';

matlabbatch{4}.spm.spatial.realign.estimate.eoptions.quality = 0.9;
matlabbatch{4}.spm.spatial.realign.estimate.eoptions.sep = 4;

matlabbatch{4}.spm.spatial.realign.estimate.eoptions.fwhm = 1;

matlabbatch{4}.spm.spatial.realign.estimate.eoptions.rtm = 1;

matlabbatch{4}.spm.spatial.realign.estimate.eoptions.interp = 2;
matlabbatch{4}.spm.spatial.realign.estimate.eoptions.wrap = [0 0 0];
matlabbatch{4}.spm.spatial.realign.estimate.eoptions.weight = '';

matlabbatch{5}.spm.spatial.realign.estimate.data = {

                                        {
```

```
                                        T1FLIP15
                                        T1FLIP60
                                        }

                                       }';

matlabbatch{5}.spm.spatial.realign.estimate.eoptions.quality = 0.9;
matlabbatch{5}.spm.spatial.realign.estimate.eoptions.sep = 4;

matlabbatch{5}.spm.spatial.realign.estimate.eoptions.fwhm = 1;

matlabbatch{5}.spm.spatial.realign.estimate.eoptions.rtm = 1;

matlabbatch{5}.spm.spatial.realign.estimate.eoptions.interp = 2;
matlabbatch{5}.spm.spatial.realign.estimate.eoptions.wrap = [0 0 0];
matlabbatch{5}.spm.spatial.realign.estimate.eoptions.weight = '';

matlabbatch{6}.spm.spatial.coreg.estimate.ref = {


 T1RHO20


};
matlabbatch{6}.spm.spatial.coreg.estimate.source = {


                T1FLIP15


  };
matlabbatch{6}.spm.spatial.coreg.estimate.other = {


   T1FLIP30


   T1FLIP60


 };
matlabbatch{6}.spm.spatial.coreg.estimate.eoptions.cost_fun = 'nmi';
matlabbatch{6}.spm.spatial.coreg.estimate.eoptions.sep = [4 2];
matlabbatch{6}.spm.spatial.coreg.estimate.eoptions.tol = [0.02 0.02 0.02
0.001 0.001 0.001 0.01 0.01 0.01 0.001 0.001 0.001];
matlabbatch{6}.spm.spatial.coreg.estimate.eoptions.fwhm = [1 1];
spm_jobman('run',matlabbatch);
```

```
%% Calculate T1ρ and T1

addpath('/labs/twells/mario/src');


V = {T1RHO20;...

                                        %(comment_50_1)sT1RHO50;...


                                        T1RHO80};



calc_t1_rho(V,T1RHO);

V = {T1FLIP15;...
                                        T1FLIP30;...
                                        T1FLIP60};
calc_t1(V,T1)


%% Binarize and mask

clear matlabbatch;
matlabbatch{1}.spm.spatial.coreg.estimate.ref = {T1RHO20};
matlabbatch{1}.spm.spatial.coreg.estimate.source = {T1W_MASK};
matlabbatch{1}.spm.spatial.coreg.estimate.other = {''};
matlabbatch{1}.spm.spatial.coreg.estimate.eoptions.cost_fun = 'nmi';
matlabbatch{1}.spm.spatial.coreg.estimate.eoptions.sep = [4 2];
matlabbatch{1}.spm.spatial.coreg.estimate.eoptions.tol = [0.02 0.02 0.02
0.001 0.001 0.001 0.01 0.01 0.01 0.001 0.001 0.001];
matlabbatch{1}.spm.spatial.coreg.estimate.eoptions.fwhm = [1 1];
matlabbatch{2}.spm.spatial.coreg.write.ref = {T1W_MASK};
matlabbatch{2}.spm.spatial.coreg.write.source = {T1RHO20};
matlabbatch{2}.spm.spatial.coreg.write.roptions.interp = 1;
matlabbatch{2}.spm.spatial.coreg.write.roptions.wrap = [0 0 0];
matlabbatch{2}.spm.spatial.coreg.write.roptions.mask = 0;
matlabbatch{2}.spm.spatial.coreg.write.roptions.prefix = 'r_T1rcoregT1';
matlabbatch{3}.spm.util.imcalc.input = {T1W_MASK

                                                T1rCOREGT1

                                                };
matlabbatch{3}.spm.util.imcalc.output = BINMULT;
```

```
matlabbatch{3}.spm.util.imcalc.outdir = {ANALYSIS_DIR};
matlabbatch{3}.spm.util.imcalc.expression = 'i1.*(i2>0)';
matlabbatch{3}.spm.util.imcalc.options.dmtx = 0;
matlabbatch{3}.spm.util.imcalc.options.mask = 0;
matlabbatch{3}.spm.util.imcalc.options.interp = 1;
matlabbatch{3}.spm.util.imcalc.options.dtype = 16;

spm_jobman('run',matlabbatch);


%% T2 Analysis

%% Sanitize the T2 images to only those ending in -0001.nii
list_dir = dir(T2_PATH);
san_dir = {};
[len n] = size(list_dir);
for i=3:len
        token = strtok(list_dir(i).name,'.');
        if token(end) == '1'
                san_dir{end+1} = list_dir(i).name;
        end
end
san_dir = san_dir';

%% Take the log of all T2 images ending in -0001.nii
log_dir = {};
[len n] = size(san_dir);
for i=1:len
        log_dir{end+1} = strcat(T2_PATH,'/log',san_dir{i});

        clear matlabbatch;
        matlabbatch{1}.spm.util.imcalc.input =
{strcat(T2_PATH,'/',san_dir{i})};
        matlabbatch{1}.spm.util.imcalc.output =
strcat(T2_PATH,'/log',san_dir{i});
        matlabbatch{1}.spm.util.imcalc.outdir = {ANALYSIS_DIR};
        matlabbatch{1}.spm.util.imcalc.expression = 'log(i1)';
        matlabbatch{1}.spm.util.imcalc.options.dmtx = 0;
        matlabbatch{1}.spm.util.imcalc.options.mask = 0;
        matlabbatch{1}.spm.util.imcalc.options.interp = 1;
        matlabbatch{1}.spm.util.imcalc.options.dtype = 16;

        spm_jobman('run',matlabbatch);
end
log_dir = log_dir';

clear matlabbatch;
mkdir(strcat(ANALYSIS_DIR,'/spm'));
```

```
		matlabbatch{1}.spm.stats.factorial_design.dir =
{strcat(ANALYSIS_DIR,'/spm')};
		matlabbatch{1}.spm.stats.factorial_design.des.mreg.scans = log_dir;
		matlabbatch{1}.spm.stats.factorial_design.des.mreg.mcov.c = [15
                                                             30
                                                             45
                                                             60
                                                             75
                                                             90];
		matlabbatch{1}.spm.stats.factorial_design.des.mreg.mcov.cname = 'TEs';
		matlabbatch{1}.spm.stats.factorial_design.des.mreg.mcov.iCC = 5;
		matlabbatch{1}.spm.stats.factorial_design.des.mreg.incint = 1;
		matlabbatch{1}.spm.stats.factorial_design.cov = struct('c', {}, 'cname', {},
'iCFI', {}, 'iCC', {});
		matlabbatch{1}.spm.stats.factorial_design.masking.tm.tm_none = 1;
		matlabbatch{1}.spm.stats.factorial_design.masking.im = 1;
		matlabbatch{1}.spm.stats.factorial_design.masking.em = {''};
		matlabbatch{1}.spm.stats.factorial_design.globalc.g_omit = 1;
		matlabbatch{1}.spm.stats.factorial_design.globalm.gmsca.gmsca_no = 1;
		matlabbatch{1}.spm.stats.factorial_design.globalm.glonorm = 1;
		matlabbatch{2}.spm.stats.fmri_est.spmmat =
{strcat(ANALYSIS_DIR,'/spm/SPM.mat')};
		matlabbatch{2}.spm.stats.fmri_est.method.Classical = 1;
		matlabbatch{3}.spm.util.imcalc.input = {BETAIMG};
		matlabbatch{3}.spm.util.imcalc.output = INVBETAIMG;
		matlabbatch{3}.spm.util.imcalc.outdir = {ANALYSIS_DIR};
		matlabbatch{3}.spm.util.imcalc.expression = '-1./i1';
		matlabbatch{3}.spm.util.imcalc.options.dmtx = 0;
		matlabbatch{3}.spm.util.imcalc.options.mask = 0;
		matlabbatch{3}.spm.util.imcalc.options.interp = 1;
		matlabbatch{3}.spm.util.imcalc.options.dtype = 16;


		spm_jobman('run',matlabbatch);

catch
		disp('There was an error in the first-level matlab call.');
end
quit;
```

Analysis Template

```
#!/bin/tcsh
#PBS -M maryellen.koran@gmail.com
#PBS -m bae
#PBS -l nodes=vision.mc.vanderbilt.edu
#PBS -l walltime=1:00:00:00
#PBS -l mem=8000mb

## Setup FreeSurfer variables
setenv ANALYSIS_DIR
/labs/twells/data/%(study)s/t1rho_voxel/%(scanid)s/%(hz)s

# Ensure the directories exist
mkdir -p $ANALYSIS_DIR

## Setup script variables
setenv T1W      $ANALYSIS_DIR/%(t1w_filename)s

setenv T1RHO20
          $ANALYSIS_DIR/%(t1rho_20_filename)s
setenv T1RHO80
          $ANALYSIS_DIR/%(t1rho_80_filename)s
setenv T1RHO                    $ANALYSIS_DIR/Thornton-
Wells_%(scanid)s_%(hz)sHz_t1-rho-voxel.nii
setenv T1FLIP15
          $ANALYSIS_DIR/%(t1_flip_15_filename)s
setenv T1FLIP30
          $ANALYSIS_DIR/%(t1_flip_30_filename)s
setenv T1FLIP60
          $ANALYSIS_DIR/%(t1_flip_60_filename)s
setenv T1                       $ANALYSIS_DIR/Thornton-
Wells_%(scanid)s_t1-voxel.nii
setenv MATLAB                   %(matlab)s

## Setup log variable
setenv LOG
          $MARIO/log/t1rho_voxel_%(scanid)s_%(hz)s.log

## Copy all input images to the analysis folder

cp -f %(t1w_abs)s $T1W
```

```
cp -f %(t1rho_20_abs)s $T1RHO20
cp -f %(t1rho_80_abs)s $T1RHO80
cp -f %(t1_flip_15_abs)s $T1FLIP15
cp -f %(t1_flip_30_abs)s $T1FLIP30
cp -f %(t1_flip_60_abs)s $T1FLIP60

##cd $ANALYSIS_DIR
cd %(matlab_pathdef)s

## marker
echo "T1 Rho Calculation: " >> $LOG

## ----- Start matlab ---- ##
$MATLAB -nodisplay -nodesktop -nosplash < %(t1rho_matlab)s
```

MATLAB and SPM Code for T1ρ, T1, and T2 calculation

```
try

        ANALYSIS_DIR =
'/labs/twells/data/%(study)s/t1rho_voxel/%(scanid)s/%(hz)s';

        T1W      = strcat(ANALYSIS_DIR,'/%(t1w_filename)s');
        T1RHO20   = strcat(ANALYSIS_DIR,'/%(t1rho_20_filename)s');
        T1RHO80   = strcat(ANALYSIS_DIR,'/%(t1rho_80_filename)s');
        T1RHO     = strcat(ANALYSIS_DIR,'/Thornton-Wells
_%(scanid)s_%(hz)sHz_t1-rho-voxel.nii');
        T1FLIP15  = strcat(ANALYSIS_DIR,'/%(t1_flip_15_filename)s');
        T1FLIP30  = strcat(ANALYSIS_DIR,'/%(t1_flip_30_filename)s');
        T1FLIP60  = strcat(ANALYSIS_DIR,'/%(t1_flip_60_filename)s');
        T1       = strcat(ANALYSIS_DIR,'/Thornton-Wells _%(scanid)s_t1-
voxel.nii');

        wT1RHO20   = strcat(ANALYSIS_DIR,'/w','%(t1rho_20_filename)s');
        wT1RHO80   = strcat(ANALYSIS_DIR,'/w','%(t1rho_80_filename)s');
        wT1FLIP15  = strcat(ANALYSIS_DIR,'/w','%(t1_flip_15_filename)s');
        wT1FLIP30  = strcat(ANALYSIS_DIR,'/w','%(t1_flip_30_filename)s');
        wT1FLIP60  = strcat(ANALYSIS_DIR,'/w','%(t1_flip_30_filename)s');


        %% Realign
        clear matlabbatch;
        spm_jobman('initcfg');
        spm('defaults', 'FMRI');
```

```
matlabbatch{1}.spm.spatial.realign.estimate.data = {
                                                    {
                                                    T1RHO20
T1RHO80
}
                                                    }';
matlabbatch{1}.spm.spatial.realign.estimate.eoptions.quality = 0.9;
matlabbatch{1}.spm.spatial.realign.estimate.eoptions.sep = 4;
matlabbatch{1}.spm.spatial.realign.estimate.eoptions.fwhm = 1;
matlabbatch{1}.spm.spatial.realign.estimate.eoptions.rtm = 0;
matlabbatch{1}.spm.spatial.realign.estimate.eoptions.interp = 2;
matlabbatch{1}.spm.spatial.realign.estimate.eoptions.wrap = [0 0 0];
matlabbatch{1}.spm.spatial.realign.estimate.eoptions.weight = '';
matlabbatch{2}.spm.spatial.realign.estimate.data = {
                                                    {
T1FLIP15
T1FLIP30
T1FLIP60
                                                    }
                                                    }';
matlabbatch{2}.spm.spatial.realign.estimate.eoptions.quality = 0.9;
matlabbatch{2}.spm.spatial.realign.estimate.eoptions.sep = 4;
matlabbatch{2}.spm.spatial.realign.estimate.eoptions.fwhm = 1;
matlabbatch{2}.spm.spatial.realign.estimate.eoptions.rtm = 0;
matlabbatch{2}.spm.spatial.realign.estimate.eoptions.interp = 2;
matlabbatch{2}.spm.spatial.realign.estimate.eoptions.wrap = [0 0 0];
matlabbatch{2}.spm.spatial.realign.estimate.eoptions.weight = '';
matlabbatch{3}.spm.spatial.coreg.estimate.ref = { T1W       };
matlabbatch{3}.spm.spatial.coreg.estimate.source = {T1RHO20};
matlabbatch{3}.spm.spatial.coreg.estimate.other = {
                                                   T1RHO80                                                  };
matlabbatch{3}.spm.spatial.coreg.estimate.eoptions.cost_fun = 'mi';
matlabbatch{3}.spm.spatial.coreg.estimate.eoptions.sep = [4 2];
matlabbatch{3}.spm.spatial.coreg.estimate.eoptions.tol = [0.02 0.02 0.02 0.001 0.001
0.001 0.01 0.01 0.01 0.001 0.001 0.001];
matlabbatch{3}.spm.spatial.coreg.estimate.eoptions.fwhm = [7 7];
matlabbatch{4}.spm.spatial.coreg.estimate.ref = { T1W       };
matlabbatch{4}.spm.spatial.coreg.estimate.source = { T1FLIP15
};
matlabbatch{4}.spm.spatial.coreg.estimate.other = {
T1FLIP30
T1FLIP60
                                                   };
matlabbatch{4}.spm.spatial.coreg.estimate.eoptions.cost_fun = 'mi';
matlabbatch{4}.spm.spatial.coreg.estimate.eoptions.sep = [4 2];
matlabbatch{4}.spm.spatial.coreg.estimate.eoptions.tol = [0.02 0.02 0.02 0.001 0.001
0.001 0.01 0.01 0.01 0.001 0.001 0.001];
matlabbatch{4}.spm.spatial.coreg.estimate.eoptions.fwhm = [7 7];
```

```
matlabbatch{5}.spm.spatial.normalise.estwrite.subj.source = { T1W       };
matlabbatch{5}.spm.spatial.normalise.estwrite.subj.wtsrc = '';
%%
matlabbatch{5}.spm.spatial.normalise.estwrite.subj.resample = {
                                                    T1FLIP15
T1FLIP30
T1FLIP60
T1RHO20
T1RHO80
                                                    };
%%
matlabbatch{5}.spm.spatial.normalise.estwrite.eoptions.template =
{'/home/pryweljr/spm8/templates/T1.nii,1'};
matlabbatch{5}.spm.spatial.normalise.estwrite.eoptions.weight = '';
matlabbatch{5}.spm.spatial.normalise.estwrite.eoptions.smosrc = 8;
matlabbatch{5}.spm.spatial.normalise.estwrite.eoptions.smoref = 0;
matlabbatch{5}.spm.spatial.normalise.estwrite.eoptions.regtype = 'mni';
matlabbatch{5}.spm.spatial.normalise.estwrite.eoptions.cutoff = 25;
matlabbatch{5}.spm.spatial.normalise.estwrite.eoptions.nits = 16;
matlabbatch{5}.spm.spatial.normalise.estwrite.eoptions.reg = 1;
matlabbatch{5}.spm.spatial.normalise.estwrite.roptions.preserve = 0;
matlabbatch{5}.spm.spatial.normalise.estwrite.roptions.bb = [-78 -112 -50
                                                    78 76 85];
matlabbatch{5}.spm.spatial.normalise.estwrite.roptions.vox = [2 2 2];
matlabbatch{5}.spm.spatial.normalise.estwrite.roptions.interp = 1;
matlabbatch{5}.spm.spatial.normalise.estwrite.roptions.wrap = [0 0 0];
matlabbatch{5}.spm.spatial.normalise.estwrite.roptions.prefix = 'w';
spm_jobman('run',matlabbatch);
```

```
%% Calculate T1ρ and T1

addpath('/labs/twells/mario/src');


V = {wT1RHO20;...


%(comment_50_1)sT1RHO50;...


wT1RHO80};


calc_t1_rho(V,T1RHO);
```

```
                V = {wT1FLIP15;...
                                        wT1FLIP30;...
                                        wT1FLIP60};
                calc_t1(V,T1)


catch
                disp('There was an error in the first-level matlab call.');
end
quit;
```

Quantifying Images

Quantification of T1ρ-weighted Images

```
function calc_t1_rho(V,outfile)

% T1ρ Calculation 2.0
% Includes Normalization
%
% Requires SPM
%
% Jared Cobb, VUIIS
% Adapted by Manus J. Donahue
% Adapted by R. Michael Sivley, CHGR

%% Ensure we do not get stuck in MATLAB
try

[NUM_FILES,dim] = size(V);
if NUM_FILES < 1
   disp('Too few files. Terminating...');
   return
end

FileName = cell(1,NUM_FILES);
PathName = cell(1,NUM_FILES);

for i = 1:NUM_FILES
   [pth,nam,ext] = spm_fileparts(V{i});
```

```
   FileName{i} = strcat(nam,ext);
   PathName{i} = pth;
   if exist(fullfile(pth,[nam ext])) ~= 2
      disp('File does not exist. Terminating...');
      return
   end
end

if NUM_FILES == 3
                  SLT = {'20';'50';'80'};
else if NUM_FILES == 2
                  SLT = {'20';'80'};
else
                  disp('Number of files not recognized');
                  disp('Terminating...');
                  return
   end
end

%reformat from column vector to row vector
SLT = transpose(SLT);

%convert to matrix
SLT = cellfun(@str2num,SLT);

IM = vuOpenImage(fullfile(PathName{1},FileName{1}));
[i,j,k] = size(IM.Data);

% initialize the final t1-rho image
t1_rho = zeros(i,j,k);

for i = 1:NUM_FILES
   IM = vuOpenImage(fullfile(PathName{i},FileName{i}));
   % all 3D data from all images
   full_stack(:,:,:,i) = IM.Data(:,:,:);
end


%Loop for each slice
for sl = 1:k

   % local stack contains 1 2D slice per image
   stack(:,:,:) = full_stack(:,:,sl,:);


   %%
   %close all; clc;

   % slice is chosen above for simplicity
```

```
[nRows nCols numEcho] = size(stack);


%create threshold mask
firstImage_m = squeeze(stack(:,:,numEcho));
maxValue = max(firstImage_m(:));
%mask_m = (firstImage_m > 0.05 * maxValue ); % 5% mask
mask_m = (firstImage_m > 0);

% COBBJG : START Single Parm MonoExponential Fit MAP
warning off all
%Initial Conditions & Settings


t2_m = zeros(nRows, nCols);
s0_m = zeros(nRows, nCols);
R_m = zeros(nRows,nCols);
t2lim = 500;  % upper limit based on type o scan / tissue
echoes = SLT';


for row = 1:nRows
   for col = 1:nCols
      % is this mask what accounts for black pixels?
      if (mask_m(row,col) == 1)
         % stack is a stack of scans
         % signal_v is the stack of voxels at row,col
         signal_v = squeeze(stack(row, col, :));
         % the log of the images is taken at the last second
         signal_v(isfinite(signal_v)==0)=500;
         coeff_v = polyfit(echoes, max(0,log(signal_v)), 1);
         slope = coeff_v(1);
         logS0 = coeff_v(2); % Intercept.
         fit = polyval(coeff_v, echoes);
         R_squared = corrcoef(signal_v, fit);
         t2 = -1 / slope;
         % Force a lower limit on the slope:
         if (isfinite(t2)==0)
            t2 = t2lim;
         end
         if (t2 > t2lim)
            t2 = t2lim;
         end
         if (t2 < 0)
            t2 = 0;
         end
         %end slope limit
         t2_m(row,col) = t2;
         s0_m(row,col) = exp(logS0);
```

```
            R_m(row,col) = R_squared(2);
          end
        end
    end
    % assign the t2_m to the current t1_rho slice
    t1_rho(:,:,sl) = t2_m(:,:);
    warning on all

end % end the slice loop

% Optimize the output parameters for T1-Rho
IM.Parms.datatype = 16;
IM.Parms.bitpix = 32;
IM.Parms.scl_slope = 1;
IM.Parms.scl_inter = 0;

% Or building a more unique name for the output
[path,descrip,ext] = fileparts(outfile); %must be 80 characters
for ii = size(descrip,2)+1:80
        descrip = [descrip ' '];
end
IM.Parms.descrip = descrip;

% copy the computed t1_rho into the image data
IM.Data(:,:,:) = t1_rho(:,:,:);

vuWriteImage(IM,outfile);

catch
disp('There was an error while computing T1ρ.');
end
```

Quantification of T1 Images

```
%
% T1 MAP from dynamic flip angle diminish data
%Provided by E. Brian Welch, PhD
%
function calc_t1(V,outfile)

%% Ensure we do not get stuck in MATLAB
try

na = length(V);
```

```
FileName = cell(1,na);
PathName = cell(1,na);

for i = 1:na
                [pth,nam,ext] = spm_fileparts(V{i});
                FileName{i}   = strcat(nam,ext);
                PathName{i}   = pth;
                if exist(fullfile(pth,[nam ext])) ~= 2
                                disp('File does not exist. Terminating...');
                                return
                end
end

IM = vuOpenImage(fullfile(PathName{1},FileName{1}));
[nx,ny,nz] = size(IM.Data);

%%[info] = loadPARREC('parfile_prefixes{1}');
%%nx = info.datasize(1);
%%ny = info.datasize(2);
%%nz = info.datasize(3);
%%na = length(parfile_prefixes);

data_total = zeros([nx ny nz na],'double');

%%flip_angles_degrees = zeros(length(parfile_prefixes),1);
flip_angles_degrees = [15 30 60];

%%tr = str2num(info.pardef.Repetition_time_ms) / 1000; % grab TR from info struct
tr = .1; %TR in seconds here so T1 should be in seconds

%% load all of the data
for a=1:na,
   %%[data,info] = loadPARREC(parfile_prefixes{a});
   IM = vuOpenImage(fullfile(PathName{a},FileName{a}));
   data = IM.Data;
   data_total(:,:,:,a) = data;
   %%flip_angles_degrees(a) = info.imgdef.image_flip_angle_in_degrees.uniq(1);
end

%% find a mask using Otsu's method for fasting execition
data_total = data_total - min(data_total(:));
data_total = data_total / max(data_total(:));
data_sum_all_angles = sum(data_total,4);
otsu_level = graythresh(data_sum_all_angles);
mask_xyz = data_sum_all_angles > otsu_level;

%% setup for the lsqcurvefit
xdata = flip_angles_degrees(:) * pi/180.0;
LB=[]; UB=[];
```

```
m0 = zeros(nx,ny,nz,'double');
t1 = zeros(nx,ny,nz,'double');
resnorm_array = zeros(nx,ny,nz,'double');
residual_array = zeros(nx,ny,nz,na,'double');
exitflag_array = zeros(nx,ny,nz,'double');

% turn warnings off
warning off;

try
  options = optimset('lsqcurvefit');
catch
  options = [];
end
options = optimset(options,'Display','off');
options = optimset(options,'Algorithm','levenberg-marquardt');

%% Loop over 3D volume
for xidx=[1:nx],
    for yidx=[1:ny],
        for zidx=[1:nz],

            ydata = data_total(xidx,yidx,zidx,:);
            ydata = ydata(:);

            if mask_xyz(xidx,yidx,zidx),
                x0 = [1];
                [x,resnorm,residual,exitflag,output] = lsqcurvefit(@(x,xdata)
ssi(x,xdata,tr,ydata),x0,xdata,ydata,LB,UB,options);

                t1(xidx,yidx,zidx) = x(1);

                resnorm_array(xidx,yidx,zidx) = resnorm;
                residual_array(xidx,yidx,zidx,:) = residual;
                exitflag_array(xidx,yidx,zidx) = exitflag;

                E1 = exp(-tr/ t1(xidx,yidx,zidx) );
                F = sin(xdata) .* (1-E1)./(1-E1.*cos(xdata));
                m0(xidx,yidx,zidx) = F\ydata;
            end
        end
    end
    disp( sprintf('Completed %03d of %03d', xidx, nx) );
end

%% make an r1 map
r1 = zeros(nx,ny,nz);
r1(mask_xyz) = 1./( t1(mask_xyz) + eps);
```

```
% Optimize the output parameters for T1
IM.Parms.datatype = 16;
IM.Parms.bitpix = 32;
IM.Parms.scl_slope = 1;
IM.Parms.scl_inter = 0;

% Or building a more unique name for the output
[path,descrip,ext] = fileparts(outfile); %must be 80 characters
for ii = size(descrip,2)+1:80
        descrip = [descrip ' '];
end
IM.Parms.descrip = descrip;

% copy the computed t1_rho into the image data
IM.Data(:,:,:) = t1(:,:,:);

vuWriteImage(IM,outfile);

%% turn warnings back on
warning on;

catch
disp('An error occured while calculating T1.');
end
```

Appendix B

SUPPORTING INFORMATION FOR CHAPTER 3

Table 20 Results from analysis of relationship between volume and age using typically developing controls as the control group. DS = Down Syndrome. WS = William's Syndrome.

ROI	Group	t	p-value
LeftInfLatVent	DS	4.32	3.21E-05
RightInfLatVent	DS	4.05	8.85E-05
lh_superiorparietal_volume	DS	-4.04	9.26E-05
lh_inferiorparietal_volume	DS	-3.98	1.16E-04
lh_parsorbitalis_volume	DS	-3.81	2.21E-04
rh_postcentral_volume	DS	-3.67	3.56E-04
nonWMhypointensities	DS	3.41	8.84E-04
lh_precuneus_volume	DS	-3.39	9.29E-04
lh_medialorbitofrontal_volume	DS	-3.37	1.01E-03
LeftPallidum	DS	-3.28	1.35E-03
rh_cuneus_volume	DS	-3.25	1.46E-03
rh_superiorfrontal_volume	DS	-3.25	1.46E-03
RightPallidum	DS	-3.22	1.61E-03
lh_isthmuscingulate_volume	DS	-3.18	1.84E-03
rh_lateralorbitofrontal_volume	DS	-3.14	2.09E-03
lh_parstriangularis_volume	DS	-3.13	2.21E-03
LeftHippocampus	DS	-3.11	2.30E-03
RightLateralVentricle	DS	3.05	2.78E-03
rh_paracentral_volume	DS	-3.02	3.10E-03
rh_parsorbitalis_volume	DS	-3.00	3.28E-03
RightThalamusProper	DS	-3.00	3.31E-03
rhCortexVol	DS	-2.98	3.47E-03
CortexVol	DS	-2.97	3.60E-03
CC_Mid_Anterior	DS	-2.95	3.80E-03
rh_rostralmiddlefrontal_volume	DS	-2.95	3.82E-03
lhCortexVol	DS	-2.94	3.89E-03
RightAmygdala	DS	-2.91	4.22E-03
LeftAmygdala	DS	-2.91	4.23E-03

rh_precuneus_volume	DS	-2.91	4.33E-03
lh_postcentral_volume	DS	-2.86	4.97E-03
lh_rostralmiddlefrontal_volume	DS	-2.85	5.09E-03
LeftLateralVentricle	DS	2.78	6.27E-03
rh_entorhinal_volume	DS	-2.78	6.37E-03
RightAccumbensarea	DS	-2.77	6.46E-03
TotalGrayVol	DS	-2.77	6.54E-03
lh_middletemporal_volume	DS	-2.76	6.58E-03
rh_temporalpole_volume	DS	-2.73	7.20E-03
rh_medialorbitofrontal_volume	DS	-2.73	7.20E-03
lh_paracentral_volume	DS	-2.71	7.60E-03
lh_lateralorbitofrontal_volume	DS	-2.69	8.08E-03
LeftThalamusProper	DS	-2.69	8.22E-03
rh_frontalpole_volume	DS	-2.69	8.23E-03
rh_parstriangularis_volume	DS	-2.62	9.97E-03
rh_isthmuscingulate_volume	DS	-2.61	1.00E-02
rh_inferiorparietal_volume	DS	-2.58	1.11E-02
lh_parahippocampal_volume	DS	-2.57	1.13E-02
rh_superiortemporal_volume	DS	-2.53	1.27E-02
rh_insula_volume	DS	-2.47	1.50E-02
SupraTentorialVol	DS	-2.45	1.56E-02
lh_superiorfrontal_volume	DS	-2.45	1.58E-02
lh_fusiform_volume	DS	-2.43	1.66E-02
lh_parsopercularis_volume	DS	-2.33	2.12E-02
lh_lateraloccipital_volume	DS	-2.32	2.22E-02
rh_lateraloccipital_volume	DS	-2.25	2.60E-02
rh_posteriorcingulate_volume	DS	-2.22	2.79E-02
rh_fusiform_volume	DS	-2.17	3.21E-02
lh_superiortemporal_volume	DS	-2.13	3.49E-02
rh_middletemporal_volume	DS	-2.02	4.52E-02
lh_posteriorcingulate_volume	DS	-1.98	4.95E-02
LeftPutamen	DS	-1.95	5.36E-02
lhCorticalWhiteMatterVol	DS	-1.95	5.39E-02
LeftCaudate	DS	-1.94	5.51E-02
CorticalWhiteMatterVol	DS	-1.93	5.54E-02
rh_pericalcarine_volume	DS	-1.92	5.67E-02
rh_superiorparietal_volume	DS	-1.92	5.68E-02
CC_Anterior	DS	-1.91	5.84E-02
rhCorticalWhiteMatterVol	DS	-1.91	5.85E-02
rh_inferiortemporal_volume	DS	-1.90	5.95E-02
lh_inferiortemporal_volume	DS	-1.89	6.16E-02

rh_supramarginal_volume	DS	-1.84	6.76E-02
RightPutamen	DS	-1.82	7.07E-02
rh_bankssts_volume	DS	-1.81	7.22E-02
lh_insula_volume	DS	-1.81	7.24E-02
SubCortGrayVol	DS	-1.74	8.38E-02
rh_caudalanteriorcingulate_volume	DS	-1.74	8.48E-02
rh_parsopercularis_volume	DS	-1.70	9.22E-02
RightCaudate	DS	-1.69	9.26E-02
LeftVentralDC	DS	-1.68	9.64E-02
rh_lingual_volume	DS	-1.67	9.65E-02
lh_cuneus_volume	DS	-1.67	9.69E-02
rh_parahippocampal_volume	DS	-1.67	9.80E-02
rh_transversetemporal_volume	DS	-1.66	9.86E-02
lh_rostralanteriorcingulate_volume	DS	-1.66	9.97E-02
LeftAccumbensarea	DS	-1.64	1.03E-01
RightVentralDC	DS	-1.63	1.06E-01
lh_caudalanteriorcingulate_volume	DS	-1.59	1.14E-01
lh_temporalpole_volume	DS	-1.56	1.21E-01
CC_Central	DS	-1.55	1.23E-01
lh_lingual_volume	DS	-1.51	1.34E-01
BrainStem	DS	-1.49	1.39E-01
Rightvessel	DS	-1.48	1.43E-01
rh_precentral_volume	DS	-1.46	1.46E-01
RightHippocampus	DS	-1.42	1.59E-01
lh_transversetemporal_volume	DS	-1.38	1.69E-01
Leftvessel	DS	-1.36	1.76E-01
CC_Posterior	DS	-1.31	1.94E-01
lh_pericalcarine_volume	DS	-1.27	2.06E-01
CC_Mid_Posterior	DS	-1.22	2.24E-01
RightCerebellumCortex	DS	-1.13	2.59E-01
lh_precentral_volume	DS	-1.11	2.71E-01
lh_supramarginal_volume	DS	-1.10	2.73E-01
lh_bankssts_volume	DS	-1.08	2.84E-01
rh_rostralanteriorcingulate_volume	DS	-1.06	2.93E-01
Leftchoroidplexus	DS	-1.05	2.97E-01
LeftCerebellumCortex	DS	-0.93	3.54E-01
lh_frontalpole_volume	DS	-0.93	3.57E-01
lh_entorhinal_volume	DS	-0.91	3.62E-01
lh_caudalmiddlefrontal_volume	DS	-0.87	3.84E-01
LeftCerebellumWhiteMatter	DS	-0.83	4.08E-01
WMhypointensities	DS	0.81	4.20E-01

rh_caudalmiddlefrontal_volume	DS	-0.80	4.24E-01
RightCerebellumWhiteMatter	DS	-0.71	4.78E-01
OpticChiasm	DS	-0.45	6.50E-01
Rightchoroidplexus	DS	-0.05	9.59E-01
CSF	DS	-0.02	9.85E-01
LeftnonWMhypointensities	DS	NA	NA
LeftWMhypointensities	DS	NA	NA
RightnonWMhypointensities	DS	NA	NA
RightWMhypointensities	DS	NA	NA
WMhypointensities	WS	3.27	1.39E-03
rh_medialorbitofrontal_volume	WS	-2.37	1.94E-02
Leftvessel	WS	-2.20	2.98E-02
rh_entorhinal_volume	WS	-1.93	5.63E-02
lh_superiorparietal_volume	WS	-1.91	5.84E-02
lh_parstriangularis_volume	WS	-1.85	6.72E-02
Leftchoroidplexus	WS	-1.84	6.74E-02
OpticChiasm	WS	-1.71	8.90E-02
rh_superiorfrontal_volume	WS	-1.60	1.11E-01
RightVentralDC	WS	-1.55	1.23E-01
rh_temporalpole_volume	WS	-1.54	1.26E-01
rh_parstriangularis_volume	WS	-1.53	1.29E-01
rh_bankssts_volume	WS	-1.51	1.34E-01
rh_superiorparietal_volume	WS	-1.48	1.41E-01
lh_paracentral_volume	WS	-1.47	1.44E-01
Rightchoroidplexus	WS	-1.45	1.49E-01
rh_parsorbitalis_volume	WS	-1.44	1.53E-01
lh_entorhinal_volume	WS	-1.42	1.57E-01
LeftCerebellumWhiteMatter	WS	1.39	1.67E-01
rh_fusiform_volume	WS	-1.36	1.77E-01
RightCerebellumWhiteMatter	WS	1.34	1.81E-01
LeftCerebellumCortex	WS	-1.30	1.95E-01
lh_parsorbitalis_volume	WS	-1.30	1.97E-01
lh_precuneus_volume	WS	-1.28	2.02E-01
lh_caudalanteriorcingulate_volume	WS	-1.27	2.06E-01
RightCerebellumCortex	WS	-1.24	2.19E-01
rhCortexVol	WS	-1.23	2.21E-01
TotalGrayVol	WS	-1.22	2.25E-01
rh_paracentral_volume	WS	-1.21	2.28E-01
CortexVol	WS	-1.20	2.33E-01
lh_fusiform_volume	WS	-1.19	2.35E-01
lh_rostralanteriorcingulate_volume	WS	-1.19	2.35E-01

lh_precentral_volume	WS	-1.19	2.36E-01
lh_superiorfrontal_volume	WS	-1.17	2.46E-01
RightInfLatVent	WS	-1.16	2.47E-01
lhCortexVol	WS	-1.16	2.48E-01
lh_inferiorparietal_volume	WS	-1.09	2.77E-01
lh_lateralorbitofrontal_volume	WS	-1.09	2.78E-01
lh_cuneus_volume	WS	-1.08	2.81E-01
nonWMhypointensities	WS	-1.08	2.83E-01
rh_postcentral_volume	WS	-1.07	2.85E-01
rh_inferiortemporal_volume	WS	-1.07	2.87E-01
CC_Mid_Anterior	WS	1.06	2.90E-01
SubCortGrayVol	WS	-1.05	2.98E-01
rh_inferiorparietal_volume	WS	-1.04	2.99E-01
lh_supramarginal_volume	WS	-1.04	2.99E-01
lh_parsopercularis_volume	WS	-1.03	3.03E-01
rh_precuneus_volume	WS	-1.01	3.13E-01
rh_rostralmiddlefrontal_volume	WS	-1.01	3.14E-01
LeftVentralDC	WS	-1.01	3.15E-01
RightAccumbensarea	WS	-0.99	3.22E-01
rh_precentral_volume	WS	-0.96	3.40E-01
rh_frontalpole_volume	WS	-0.94	3.50E-01
lh_insula_volume	WS	-0.92	3.59E-01
rh_supramarginal_volume	WS	-0.91	3.64E-01
RightLateralVentricle	WS	-0.90	3.70E-01
rh_middletemporal_volume	WS	-0.90	3.71E-01
lh_middletemporal_volume	WS	-0.85	3.94E-01
LeftAccumbensarea	WS	-0.85	3.97E-01
rh_isthmuscingulate_volume	WS	-0.84	4.00E-01
rh_parahippocampal_volume	WS	-0.84	4.01E-01
SupraTentorialVol	WS	-0.84	4.05E-01
lh_rostralmiddlefrontal_volume	WS	-0.82	4.14E-01
LeftLateralVentricle	WS	-0.79	4.33E-01
lh_superiortemporal_volume	WS	-0.75	4.57E-01
rh_lateraloccipital_volume	WS	-0.74	4.62E-01
lh_posteriorcingulate_volume	WS	-0.69	4.91E-01
rh_lateralorbitofrontal_volume	WS	-0.68	4.97E-01
LeftCaudate	WS	-0.68	4.98E-01
CC_Central	WS	0.66	5.13E-01
RightThalamusProper	WS	-0.65	5.16E-01
RightPallidum	WS	0.64	5.23E-01
rh_cuneus_volume	WS	-0.63	5.27E-01

lh_parahippocampal_volume	WS	-0.62	5.33E-01
lh_lateraloccipital_volume	WS	-0.62	5.38E-01
lh_lingual_volume	WS	-0.62	5.38E-01
LeftPutamen	WS	-0.60	5.47E-01
rh_superiortemporal_volume	WS	-0.59	5.59E-01
RightPutamen	WS	-0.58	5.64E-01
lh_medialorbitofrontal_volume	WS	-0.58	5.64E-01
lh_caudalmiddlefrontal_volume	WS	-0.57	5.71E-01
RightCaudate	WS	-0.53	5.96E-01
rh_insula_volume	WS	-0.50	6.15E-01
rh_lingual_volume	WS	-0.47	6.37E-01
rh_transversetemporal_volume	WS	0.47	6.39E-01
rh_caudalanteriorcingulate_volume	WS	-0.44	6.62E-01
RightAmygdala	WS	0.44	6.62E-01
rh_posteriorcingulate_volume	WS	-0.41	6.82E-01
lh_temporalpole_volume	WS	-0.41	6.83E-01
lhCorticalWhiteMatterVol	WS	-0.34	7.37E-01
CorticalWhiteMatterVol	WS	-0.31	7.60E-01
CC_Posterior	WS	-0.29	7.76E-01
LeftPallidum	WS	-0.27	7.84E-01
rhCorticalWhiteMatterVol	WS	-0.27	7.85E-01
BrainStem	WS	-0.26	7.93E-01
LeftInfLatVent	WS	-0.26	7.96E-01
lh_frontalpole_volume	WS	-0.26	7.97E-01
lh_bankssts_volume	WS	-0.25	8.04E-01
lh_isthmuscingulate_volume	WS	-0.24	8.12E-01
RightHippocampus	WS	-0.24	8.14E-01
CC_Mid_Posterior	WS	0.20	8.46E-01
lh_pericalcarine_volume	WS	-0.19	8.48E-01
lh_postcentral_volume	WS	-0.19	8.48E-01
LeftThalamusProper	WS	0.16	8.70E-01
lh_transversetemporal_volume	WS	0.15	8.79E-01
rh_pericalcarine_volume	WS	-0.14	8.85E-01
LeftHippocampus	WS	0.13	8.95E-01
rh_caudalmiddlefrontal_volume	WS	0.12	9.03E-01
rh_rostralanteriorcingulate_volume	WS	-0.07	9.45E-01
CC_Anterior	WS	0.05	9.58E-01
CSF	WS	-0.04	9.70E-01
lh_inferiortemporal_volume	WS	-0.03	9.76E-01
LeftAmygdala	WS	0.03	9.77E-01
Rightvessel	WS	-0.01	9.91E-01

rh_parsopercularis_volume	WS	-0.01	9.92E-01

Table 21 Results from analysis comparing relationship with volume and age between participants with Down Syndrome and Williams Syndrome.

ROI	t	p-value
nonWMhypointensities	4.32	7.92E-05
RightLateralVentricle	4.30	8.64E-05
LeftLateralVentricle	4.16	1.35E-04
RightInfLatVent	2.93	5.25E-03
RightPallidum	-2.63	1.14E-02
WMhypointensities	2.57	1.34E-02
LeftInfLatVent	2.55	1.42E-02
lh_parstriangularis_volume	-2.51	1.57E-02
LeftThalamusProper	-2.30	2.61E-02
rh_parstriangularis_volume	-2.13	3.83E-02
CC_Mid_Anterior	-2.11	4.05E-02
LeftPallidum	-2.10	4.15E-02
rh_bankssts_volume	-2.07	4.36E-02
rh_medialorbitofrontal_volume	-2.07	4.38E-02
Leftvessel	-2.07	4.41E-02
lh_isthmuscingulate_volume	-2.06	4.52E-02
LeftHippocampus	-2.04	4.67E-02
RightThalamusProper	-2.04	4.71E-02
X.4thVentricle	2.01	5.05E-02
RightAmygdala	-1.96	5.57E-02
lh_inferiorparietal_volume	-1.85	7.08E-02
lh_superiorparietal_volume	-1.78	8.14E-02
rh_superiorfrontal_volume	-1.77	8.39E-02
lh_medialorbitofrontal_volume	-1.76	8.57E-02
lh_postcentral_volume	-1.75	8.65E-02
rh_postcentral_volume	-1.72	9.17E-02
LeftAmygdala	-1.70	9.49E-02
rh_cuneus_volume	-1.69	9.84E-02
lh_superiorparietal_volume	-1.63	1.09E-01
lh_parsorbitalis_volume	-1.63	1.10E-01
WMhypointensities	-1.59	1.18E-01
lh_fusiform_volume	-1.57	1.23E-01
X.3rdVentricle	1.56	1.25E-01
lh_precuneus_volume	-1.56	1.26E-01
lh_precuneus_volume	-1.54	1.29E-01
rh_lateralorbitofrontal_volume	-1.53	1.33E-01
lh_supramarginal_volume	-1.53	1.33E-01

LeftCerebellumWhiteMatter	1.53	1.33E-01
rh_rostralmiddlefrontal_volume	-1.51	1.38E-01
rh_lingual_volume	-1.50	1.40E-01
lh_rostralmiddlefrontal_volume	-1.49	1.43E-01
RightAccumbensarea	-1.48	1.45E-01
LeftPutamen	-1.46	1.50E-01
rh_fusiform_volume	-1.45	1.53E-01
rh_inferiorparietal_volume	-1.45	1.55E-01
LeftCerebellumCortex	-1.44	1.55E-01
rh_insula_volume	-1.44	1.56E-01
lh_superiorfrontal_volume	-1.44	1.57E-01
rh_rostralmiddlefrontal_volume	-1.43	1.61E-01
CC_Central	-1.42	1.61E-01
rhCortexVol	-1.42	1.62E-01
rh_precuneus_volume	-1.42	1.62E-01
LeftCerebellumWhiteMatter	-1.42	1.63E-01
rh_parsorbitalis_volume	-1.41	1.67E-01
TotalGrayVol	-1.40	1.69E-01
X.3rdVentricle	1.39	1.71E-01
CortexVol	-1.38	1.75E-01
CC_Anterior	-1.36	1.81E-01
rh_transversetemporal_volume	-1.35	1.83E-01
rh_superiorparietal_volume	-1.34	1.87E-01
lhCortexVol	-1.33	1.91E-01
RightPutamen	-1.32	1.95E-01
rh_superiortemporal_volume	-1.31	1.96E-01
rh_middletemporal_volume	-1.31	1.97E-01
lh_parsorbitalis_volume	-1.30	2.01E-01
RightCerebellumWhiteMatter	1.30	2.01E-01
RightVentralDC	-1.29	2.03E-01
lh_middletemporal_volume	-1.29	2.04E-01
RightAccumbensarea	-1.28	2.05E-01
rh_pericalcarine_volume	-1.28	2.07E-01
lh_lateralorbitofrontal_volume	-1.28	2.08E-01
lh_entorhinal_volume	-1.27	2.09E-01
rh_inferiortemporal_volume	-1.26	2.13E-01
rh_isthmuscingulate_volume	-1.26	2.14E-01
rhCorticalWhiteMatterVol	-1.26	2.15E-01
rh_parsopercularis_volume	-1.25	2.16E-01
lh_rostralanteriorcingulate_volume	-1.25	2.17E-01
CorticalWhiteMatterVol	-1.25	2.18E-01

rh_precuneus_volume	-1.24	2.21E-01
CortexVol	-1.24	2.21E-01
lhCortexVol	-1.24	2.22E-01
rhCortexVol	-1.24	2.23E-01
lhCorticalWhiteMatterVol	-1.23	2.25E-01
lh_caudalanteriorcingulate_volume	-1.22	2.29E-01
lh_paracentral_volume	-1.22	2.29E-01
lh_parahippocampal_volume	-1.22	2.29E-01
lh_rostralmiddlefrontal_volume	-1.21	2.31E-01
CSF	1.21	2.34E-01
RightCerebellumWhiteMatter	-1.20	2.35E-01
rh_paracentral_volume	-1.19	2.40E-01
LeftAccumbensarea	-1.18	2.42E-01
rh_posteriorcingulate_volume	-1.18	2.44E-01
rh_paracentral_volume	-1.17	2.47E-01
BrainStem	-1.17	2.47E-01
rh_frontalpole_volume	-1.17	2.49E-01
SupraTentorialVol	-1.17	2.49E-01
rh_supramarginal_volume	-1.17	2.49E-01
rh_entorhinal_volume	-1.16	2.54E-01
lh_inferiorparietal_volume	-1.15	2.54E-01
RightCerebellumCortex	-1.15	2.54E-01
lh_precentral_volume	-1.15	2.58E-01
lh_inferiortemporal_volume	-1.14	2.59E-01
lh_posteriorcingulate_volume	-1.14	2.62E-01
lh_lateraloccipital_volume	-1.13	2.63E-01
TotalGrayVol	-1.13	2.64E-01
rh_temporalpole_volume	-1.13	2.65E-01
lh_cuneus_volume	-1.12	2.67E-01
rh_superiorfrontal_volume	-1.12	2.70E-01
lh_middletemporal_volume	-1.10	2.76E-01
lh_insula_volume	-1.08	2.85E-01
SubCortGrayVol	-1.08	2.86E-01
rh_postcentral_volume	-1.08	2.87E-01
Rightvessel	-1.08	2.88E-01
lh_parstriangularis_volume	-1.07	2.88E-01
lh_parsopercularis_volume	-1.07	2.90E-01
lh_lateralorbitofrontal_volume	-1.07	2.90E-01
rh_inferiorparietal_volume	-1.07	2.91E-01
rh_precentral_volume	-1.06	2.95E-01
rh_parsorbitalis_volume	-1.04	3.05E-01

rh_parstriangularis_volume	-1.02	3.13E-01
lh_transversetemporal_volume	-1.02	3.15E-01
rh_parahippocampal_volume	-1.01	3.17E-01
lh_lingual_volume	-1.01	3.19E-01
rh_superiortemporal_volume	-1.00	3.23E-01
OpticChiasm	-0.99	3.27E-01
LeftCaudate	-0.98	3.34E-01
lh_superiortemporal_volume	-0.96	3.44E-01
CC_Mid_Posterior	-0.95	3.46E-01
rh_lateraloccipital_volume	-0.95	3.48E-01
LeftPutamen	-0.95	3.49E-01
lh_parsopercularis_volume	-0.94	3.52E-01
lh_fusiform_volume	-0.93	3.57E-01
lh_superiortemporal_volume	-0.93	3.58E-01
lh_posteriorcingulate_volume	-0.92	3.62E-01
RightLateralVentricle	0.91	3.67E-01
RightPutamen	-0.90	3.73E-01
lh_superiorfrontal_volume	-0.89	3.78E-01
rh_caudalanteriorcingulate_volume	-0.89	3.79E-01
lh_isthmuscingulate_volume	-0.88	3.81E-01
rh_lateralorbitofrontal_volume	-0.87	3.87E-01
LeftPallidum	-0.87	3.91E-01
RightCaudate	-0.86	3.94E-01
Rightchoroidplexus	0.86	3.95E-01
lh_pericalcarine_volume	-0.85	3.98E-01
X.4thVentricle	-0.85	3.99E-01
LeftVentralDC	-0.85	4.00E-01
LeftLateralVentricle	0.84	4.05E-01
rh_temporalpole_volume	-0.82	4.14E-01
lh_temporalpole_volume	-0.81	4.23E-01
OpticChiasm	0.80	4.26E-01
rh_frontalpole_volume	-0.79	4.35E-01
lh_caudalmiddlefrontal_volume	-0.77	4.43E-01
rh_middletemporal_volume	-0.77	4.45E-01
rh_cuneus_volume	-0.76	4.51E-01
lh_paracentral_volume	-0.76	4.53E-01
lh_parahippocampal_volume	-0.73	4.67E-01
rh_isthmuscingulate_volume	-0.73	4.69E-01
RightHippocampus	-0.73	4.70E-01
rh_rostralanteriorcingulate_volume	-0.72	4.76E-01
rh_supramarginal_volume	-0.71	4.80E-01

lh_bankssts_volume	-0.71	4.81E-01
rh_lateraloccipital_volume	-0.68	5.03E-01
rh_posteriorcingulate_volume	-0.67	5.08E-01
CC_Mid_Anterior	0.65	5.16E-01
rh_caudalmiddlefrontal_volume	-0.65	5.19E-01
lh_insula_volume	-0.65	5.22E-01
CC_Posterior	-0.63	5.32E-01
SupraTentorialVol	-0.62	5.39E-01
rh_inferiortemporal_volume	-0.61	5.43E-01
rh_parahippocampal_volume	-0.60	5.48E-01
lh_lateraloccipital_volume	-0.60	5.52E-01
rh_insula_volume	-0.59	5.57E-01
rh_entorhinal_volume	-0.59	5.61E-01
rh_fusiform_volume	-0.58	5.67E-01
rh_caudalanteriorcingulate_volume	-0.57	5.69E-01
LeftAccumbensarea	-0.57	5.72E-01
rh_rostralanteriorcingulate_volume	-0.57	5.73E-01
LeftVentralDC	-0.56	5.76E-01
SubCortGrayVol	-0.56	5.79E-01
X.5thVentricle	0.54	5.89E-01
lh_lingual_volume	-0.54	5.91E-01
lh_bankssts_volume	-0.53	5.98E-01
LeftThalamusProper	0.53	5.99E-01
rh_pericalcarine_volume	-0.52	6.06E-01
lh_pericalcarine_volume	-0.52	6.06E-01
Rightvessel	-0.50	6.19E-01
lh_cuneus_volume	-0.49	6.28E-01
BrainStem	0.48	6.33E-01
RightThalamusProper	-0.47	6.37E-01
LeftInfLatVent	0.47	6.37E-01
Leftchoroidplexus	0.44	6.61E-01
lh_medialorbitofrontal_volume	-0.44	6.65E-01
rh_lingual_volume	-0.41	6.86E-01
nonWMhypointensities	0.40	6.88E-01
rh_precentral_volume	-0.40	6.88E-01
lh_frontalpole_volume	-0.40	6.90E-01
rh_superiorparietal_volume	-0.37	7.11E-01
lh_rostralanteriorcingulate_volume	-0.36	7.21E-01
rh_parsopercularis_volume	-0.35	7.27E-01
Leftvessel	0.35	7.28E-01
RightHippocampus	-0.33	7.39E-01

rh_medialorbitofrontal_volume	-0.33	7.41E-01
lh_inferiortemporal_volume	-0.32	7.50E-01
CC_Central	0.32	7.54E-01
Leftchoroidplexus	-0.31	7.56E-01
rh_bankssts_volume	-0.30	7.66E-01
lh_caudalanteriorcingulate_volume	-0.29	7.74E-01
lh_postcentral_volume	-0.27	7.87E-01
RightInfLatVent	-0.27	7.91E-01
CC_Posterior	0.26	7.94E-01
lh_caudalmiddlefrontal_volume	-0.25	8.01E-01
rhCorticalWhiteMatterVol	0.25	8.02E-01
CorticalWhiteMatterVol	0.25	8.02E-01
lhCorticalWhiteMatterVol	0.25	8.04E-01
lh_entorhinal_volume	0.24	8.09E-01
lh_temporalpole_volume	-0.23	8.17E-01
X.5thVentricle	0.20	8.43E-01
RightAmygdala	0.19	8.47E-01
rh_caudalmiddlefrontal_volume	0.16	8.72E-01
lh_transversetemporal_volume	-0.16	8.72E-01
LeftCaudate	-0.15	8.80E-01
rh_transversetemporal_volume	-0.14	8.88E-01
RightVentralDC	-0.14	8.90E-01
LeftCerebellumCortex	0.12	9.09E-01
DSxAge	0.11	9.10E-01
RightPallidum	0.11	9.14E-01
lh_frontalpole_volume	-0.09	9.30E-01
CC_Mid_Posterior	-0.09	9.32E-01
RightCaudate	-0.07	9.42E-01
lh_supramarginal_volume	-0.06	9.49E-01
RightCerebellumCortex	-0.03	9.76E-01
Rightchoroidplexus	-0.03	9.77E-01
LeftAmygdala	0.03	9.78E-01
CC_Anterior	0.02	9.84E-01
LeftHippocampus	-0.02	9.85E-01
CSF	0.01	9.95E-01
lh_precentral_volume	0.00	9.99E-01

Appendix C

SUPPORTING INFORMATION FOR CHAPTER 4

Table 22 Post-hoc analysis of effect of significant interactions between *SYNJ2-PI4KA*, *PARD3-MYH2*, *PDE3A- ABHD12B*, and *OR2L13-PRKG1* on the volume of RILV and LILV combined.

	Gene 1		Gene 2		
	Gene	SNP	Gene	SNP	p-value
LILV/RILV	*SYNJ2*	rs9289528	*PI4KA*	rs1780541	1.52×10^{-13}
	PARD3	rs11596284	*MYH2*	rs3744566	3.49×10^{-8}
	PDE3A	rs11614805	*ABHD12B*	rs7154732	1.34×10^{-10}
	OR2L13	rs11590865	*PRKG1*	rs1922127	1.85x10-7

Code for InterSNP program used in gene-gene interaction analysis

```
Keyword    Parameter  Comment
TPED
          /labs/twells/MEK/PWIA_Slope_Volume/ADNI_QC_FINAL_same_
keepsubjects.tped     // path to the tped-File
TFAM
          /labs/twells/MEK/PWIA_Slope_Volume/all_path_6cov/Pheno
_RILV_slopes_2/RILV_slopes.tfam
ANNOTATIONFILE
          /labs/twells/MEK/InterSNP/annotationIlluSorted.txt
COVARIATEFILE
          /labs/twells/MEK/PWIA_Slope_Volume/ADNI1_Volume_First_
covariates.txt
PATHWAYFILE
          /labs/twells/MEK/InterSNP/KEGG_2_snp_b129.txt
```

```
STOREALL   1          "// 1=complete data will be read and
stored, or 0=data will be read line by line for the current test
and than deleted"
QT                    1
SINGLE_MARKER         4
SINGLETOP  100
TWO_MARKER 1          "// Two-marker-analysis: 1=yes, 0=no"""
TEST                  5          "// 1=chi-square-test, 2= log-
linear model, " 6 = genotypic
COVARIATES 1-6;
PATHWAY               1
SIMULATION 0
MC_WITH_SM 0
PRINTTOP   100        // Best n mulitmarker p-values are printed
ANNOTATE   1
GENECOL               5
OUTPUTNAME
           /labs/twells/MEK/PWIA_Slope_Volume/all_path_6cov/Pheno
_RILV_slopes_3/output_RILV_slopes

END
```

Appendix D

SUPPORTING INFORMATION FOR CHAPTER 5

Table 23 Mapping of Single Nucleotide Polymorphisms from significant interactions to gene and base pair location.

SNP: reference SNP number of first SNP in SNP-SNP pair. Chr: Chromosome. BP:

Base pair location.

Gene	*RYR3*	*RYR3*	*CACNA1C*	*CACNA1C*
SNP	rs16972835	rs12901404	rs7132154	rs2302729
Chr	15	15	12	12
BP	33878846	34075300	2461223	2783972

Code for InterSNP program used in gene-gene interaction analysis

```
Keyword    Parameter  Comment
TPED
           /labs/twells/MEK/AD_Pathway_InterSNP/AV45/dx_last_oppo
sitechip_followup/omni_follow.tped          // path to the tped-
File
TFAM
           /labs/twells/MEK/AD_Pathway_InterSNP/AV45/dx_last_oppo
sitechip_followup/omni/Pheno_Pheno_meanDVR/Pheno_meanDVR.tfam
ANNOTATIONFILE
           /labs/twells/MEK/InterSNP/annotationIlluSorted.txt
COVARIATEFILE
           /labs/twells/MEK/AD_Pathway_InterSNP/AV45/omni/AV45_SU
BJECTS_ADNI2omni_Cov6_dxlast.txt
STOREALL   1          "// 1=complete data will be read and
stored, or 0=data will be read line by line for the current test
and than deleted"
```

```
QT                    1
SINGLE_MARKER         4
SINGLETOP  10000
TWO_MARKER 1          "// Two-marker-analysis: 1=yes, 0=no"""
TEST                  5          "// 1=chi-square-test, 2= log-
linear model, " 6 = genotypic
COVARIATES 1-6;
SIMULATION 0
MC_WITH_SM 0
PRINTTOP   1000       // Best n mulitmarker p-values are printed
ANNOTATE   1
GENECOL               5
OUTPUTNAME
           /labs/twells/MEK/AD_Pathway_InterSNP/AV45/dx_last_oppo
sitechip_followup/omni/Pheno_Pheno_meanDVR/output_Pheno_meanDVR
END
```

REFERENCES

1. Alzheimer disease. (2013). at <http://ghr.nlm.nih.gov/condition/alzheimer-disease>

2. Hebert, L. E., Scherr, P. A., Bienias, J. L., Bennett, D. A. & Evans, D. A. Alzheimer Disease in the US Population. **60,** (2013).

3. The Alzheimer's Association. 2013 Alzheimer's Disease Facts and Figures. *Alzheimer's Dement.* **9,** (2013).

4. Minati, L., Edginton, T., Bruzzone, M. G. & Giaccone, G. Current concepts in Alzheimer's disease: a multidisciplinary review. *Am. J. Alzheimers. Dis. Other Demen.* **24,** 95–121 (2009).

5. Walsh, D. M. & Selkoe, D. J. Deciphering the molecular basis of memory failure in Alzheimer's disease. *Neuron* **44,** 181–93 (2004).

6. Weintraub, S., Wicklund, A. H. & Salmon, D. P. The neuropsychological profile of Alzheimer disease. *Cold Spring Harb. Perspect. Med.* **2,** a006171 (2012).

7. Hardy, J. & Selkoe, D. J. The amyloid hypothesis of Alzheimer's disease: progress and problems on the road to therapeutics. *Science* **297,** 353–6 (2002).

8. Lorenzo, A. & Yankner, B. A. Beta-amyloid neurotoxicity requires fibril formation and is inhibited by congo red. *Proc. Natl. Acad. Sci.* **91,** 12243–12247 (1994).

9. Brun, A. & Englund, E. Regional pattern of degeneration in Alzheimer's disease: neuronal loss and histopathological grading. *Histopathology* **5,** 549–564 (1981).

10. Gatz, M. *et al.* Heritability for Alzheimer's disease: the study of dementia in Swedish twins. *J. Gerontol. A. Biol. Sci. Med. Sci.* **52,** M117–25 (1997).

11. Naj, A. C. *et al.* Common variants at MS4A4/MS4A6E, CD2AP, CD33 and EPHA1 are associated with late-onset Alzheimer's disease. *Nat. Genet.* **43,** 436–41 (2011).

12. Saunders, A. M. *et al.* Association of apolipoprotein E allele 4 with late-onset familial and sporadic Alzheimer's disease. *Neurology* **43,** 1467–1472 (1993).

13. Corder, E. H. *et al.* Gene dose of apolipoprotein E type 4 allele and the risk of Alzheimer's disease in late onset families. *Science* **261,** 921–3 (1993).

14. Lambert, J. C. *et al.* Meta-analysis of 74,046 individuals identifies 11 new susceptibility loci for Alzheimer's disease. *Nat. Genet.* (2013). doi:10.1038/ng.2802

15. Bertram, L. & Tanzi, R. E. The genetics of Alzheimer's disease. *Prog. Mol. Biol. Transl. Sci.* **107,** 79–100 (2012).

16. Pericak-Vance, M. A. & Haines, J. L. Genetic susceptibility to Alzheimer disease. *Trends Genet.* **11,** 504–8 (1995).

17. Schellenberg, G. D. & Montine, T. J. The genetics and neuropathology of Alzheimer's disease. *Acta Neuropathol.* **124,** 305–23 (2012).

18. Parker, S. E. *et al.* Updated National Birth Prevalence estimates for selected birth defects in the United States, 2004-2006. *Birth Defects Res. A. Clin. Mol. Teratol.* **88,** 1008–16 (2010).

19. Mégarbané, A. *et al.* The 50th anniversary of the discovery of trisomy 21: The past, present, and future of research and treatment of Down syndrome. *Genet. Med.* **11,** 611–616 (2009).

20. Lott, I. T. & Dierssen, M. Cognitive deficits and associated neurological complications in individuals with Down's syndrome. *Lancet Neurol.* **9,** 623–33 (2010).

21. Dierssen, M. Down syndrome: the brain in trisomic mode. *Nat. Rev. Neurosci.* **13,** 844–58 (2012).

22. Penrose, L. The incidence of mongolism in the general population. *J. Ment. Sci.* **95,** 685–8 (1949).

23. Urbano, R. C. & Roizen, N. J. in *Int. Rev. Res. Ment. Retard.* **39,** 2–33 (2010).

24. Evenhuis, H. M. The natural history of dementia in Down's syndrome. *Arch. Neurol.* **47,** 263–7 (1990).

25. Zigman, W. B. *et al.* Incidence and prevalence of dementia in elderly adults with mental retardation without down syndrome. *Am. J. Ment. Retard.* **109,** 126–41 (2004).

26. Evenhuis, H.M., Kengen, M.M.F., & Eurlings, H. A. L. Dementia Questionnaire for People with Learning Disabilities (DLD). (2007).

27. Prasher, V. P. Dementia Questionnaire for Persons with Mental Retardation (DMR): Modified Criteria for Adults with Down's Syndrome. *J. Appl. Res. Intellect. Disabil.* **10,** 54–60 (1997).

28. Oliver, C., Crayton, L., Holland, A., Hall, S. & Bradbury, J. A four year prospective study of age-related cognitive change in adults with Down's syndrome. *Psychol. Med.* **28,** 1365–77 (1998).

29. Holland, A. J., Hon, J., Huppert, F. A. & Stevens, F. Incidence And Course Of Dementia In People With Down's Syndrome: Findings From A Population-Based Study. *J. Intellect. Disabil. Res.* **44,** 138–146 (2001).

30. Cooper, S. A. & Prasher, V. P. Maladaptive behaviours and symptoms of dementia in adults with Down's syndrome compared with adults with intellectual disability of other aetiologies. *J. Intellect. Disabil. Res.* **42 (Pt 4),** 293–300 (1998).

31. Temple, V., Jozsvai, E., Konstantareas, M. M. & Hewitt, T. A. Alzheimer dementia in Down's syndrome: the relevance of cognitive ability. *J. Intellect. Disabil. Res.* **45,** 47–55 (2001).

32. Mann, D. M. The pathological association between Down syndrome and Alzheimer disease. *Mech. Ageing Dev.* **43,** 99–136 (1988).

33. Oyama, F. *et al.* Down's Syndrome: Up-Regulation of β-Amyloid Protein Precursor and τ mRNAs and Their Defective Coordination. *J. Neurochem.* **62,** 1062–1066 (1994).

34. Bertram, L. & Tanzi, R. E. Thirty years of Alzheimer's disease genetics: the implications of systematic meta-analyses. *Nat. Rev. Neurosci.* **9,** 768–78 (2008).

35. Rovelet-Lecrux, A. *et al.* APP locus duplication causes autosomal dominant early-onset Alzheimer disease with cerebral amyloid angiopathy. *Nat. Genet.* **38,** 24–6 (2006).

36. Prasher, V. P. *et al.* Molecular mapping of Alzheimer-type dementia in Down's syndrome. *Ann. Neurol.* **43,** 380–3 (1998).

37. Coppus, A. M. W. *et al.* The impact of apolipoprotein E on dementia in persons with Down's syndrome. *Neurobiol. Aging* **29,** 828–35 (2008).

38. Rumble, B. *et al.* Amyloid A4 protein and its precursor in Down's syndrome and Alzheimer's disease. *N. Engl. J. Med.* **320,** 1446–52 (1989).

39. Teipel, S. J. *et al.* Age-related cortical grey matter reductions in non-demented Down's syndrome adults determined by MRI with voxel-based morphometry. *Brain* **127,** 811–824 (2004).

40. Beacher, F. *et al.* Brain anatomy and ageing in non-demented adults with Down's syndrome: an in vivo MRI study. *Psychol. Med.* **40,** 611–9 (2010).

41. Scheltens, P. Imaging in Alzheimer's disease. *Dialogues Clin. Neurosci.* **11,** 191–9 (2009).

42. Dickerson, B. C. *et al.* Alzheimer-signature MRI biomarker predicts AD dementia in cognitively normal adults. *Neurology* **76,** 1395–402 (2011).

43. Holland, D. & Dale, A. M. Nonlinear registration of longitudinal images and measurement of change in regions of interest. *Med. Image Anal.* **15,** 489–97 (2011).

44. Salat, D. H. *et al.* Hippocampal degeneration is associated with temporal and limbic gray matter/white matter tissue contrast in Alzheimer's disease. *Neuroimage* **54,** 1795–802 (2011).

45. Dubois, B. *et al.* Research criteria for the diagnosis of Alzheimer's disease: revising the NINCDS–ADRDA criteria. *Lancet Neurol.* **6,** 734–746 (2007).

46. Devanand, D. P. *et al.* Hippocampal and entorhinal atrophy in mild cognitive impairment: prediction of Alzheimer disease. *Neurology* **68,** 828–36 (2007).

47. Pennanen, C. *et al.* Hippocampus and entorhinal cortex in mild cognitive impairment and early AD. *Neurobiol. Aging* **25,** 303–10 (2004).

48. Thompson, P. M. *et al.* Mapping hippocampal and ventricular change in Alzheimer disease. *Neuroimage* **22,** 1754–1766 (2004).

49. Jack, C. R. *et al.* MRI as a biomarker of disease progression in a therapeutic trial of milameline for AD. *Neurology* **60,** 253–260 (2003).

50. Ridha, B. H. *et al.* Volumetric MRI and cognitive measures in Alzheimer disease : comparison of markers of progression. *J. Neurol.* **255,** 567–574 (2008).

51. Jack, C. R. *et al.* Comparison of different MRI brain atrophy rate measures with clinical disease progression in AD. *Neurology* **62,** 591 –600 (2004).

52. Weiner, M. W. Expanding ventricles may detect preclinical Alzheimer disease. *Neurology* **70,** 824 –825 (2008).

53. Sperling, R. A. *et al.* Toward defining the preclinical stages of Alzheimer's disease: Recommendations from the National Institute on Aging-Alzheimer's Association workgroups on diagnostic guidelines for Alzheimer's disease. *Alzheimer's Dement.* **7,** 280–292 (2011).

54. Albert, M. S. *et al.* The diagnosis of mild cognitive impairment due to Alzheimer's disease: recommendations from the National Institute on Aging-Alzheimer's Association workgroups on diagnostic guidelines for Alzheimer's disease. *Alzheimers. Dement.* **7,** 270–9 (2011).

55. Clark, C. M. *et al.* Use of florbetapir-PET for imaging beta-amyloid pathology. *JAMA* **305,** 275–83 (2011).

56. Ikonomovic, M. D. *et al.* Post-mortem correlates of in vivo PiB-PET amyloid imaging in a typical case of Alzheimer's disease. *Brain* **131,** 1630–45 (2008).

57. Sabbagh, M. N. *et al.* Positron emission tomography and neuropathologic estimates of fibrillar amyloid-β in a patient with Down syndrome and Alzheimer disease. *Arch. Neurol.* **68,** 1461–6 (2011).

58. Handen, B. L. *et al.* Imaging brain amyloid in nondemented young adults with Down syndrome using Pittsburgh compound B. *Alzheimers. Dement.* **8,** 496–501 (2012).

59. Borthakur, A. *et al.* In vivo measurement of plaque burden in a mouse model of Alzheimer's disease. *J. Magn. Reson. Imaging* **24,** 1011–7 (2006).

60. Charagundla, S. R. T1ρ-weighted magnetic resonance imaging: Principles and diagnostic application. *Appl. Radiol.* **33,** (2004).

61. Donner, A. & Eliasziw, M. Statistical implications of the choice between a dichotomous or continuous trait in studies of interobserver agreement. *Biometrics* **50,** 550–5 (1994).

62. Gottesman, I. I. & Gould, T. The Endophenotype Concept in Psychiatry: Etymology and Strategic Intentions. *Am. J. Psychiatry* **160,** 636–645 (2003).

63. McKhann, G. M. *et al.* The diagnosis of dementia due to Alzheimer's disease: recommendations from the National Institute on Aging-Alzheimer's Association workgroups on diagnostic guidelines for Alzheimer's disease. *Alzheimers. Dement.* **7,** 263–9 (2011).

64. Potkin, S. G. *et al.* Genome-wide strategies for discovering genetic influences on cognition and cognitive disorders: methodological considerations. *Cogn. Neuropsychiatry* **14,** 391–418 (2009).

65. Peper, J. S., Brouwer, R. M., Boomsma, D. I., Kahn, R. S. & Hulshoff Pol, H. E. Genetic influences on human brain structure: a review of brain imaging studies in twins. *Hum. Brain Mapp.* **28,** 464–73 (2007).

66. Hinrichs, A. L. *et al.* Cortical binding of pittsburgh compound B, an endophenotype for genetic studies of Alzheimer's disease. *Biol. Psychiatry* **67,** 581–3 (2010).

67. Eisenberg, D. T. A., Kuzawa, C. W. & Hayes, M. G. Worldwide allele frequencies of the human apolipoprotein E gene: climate, local adaptations, and evolutionary history. *Am. J. Phys. Anthropol.* **143,** 100–11 (2010).

68. Qiu, C. Risk and protective effects of the APOE gene towards Alzheimer's disease in the Kungsholmen project: variation by age and sex. *J. Neurol. Neurosurg. Psychiatry* **75,** 828–833 (2004).

69. Tang, M. X. *et al.* The APOE-epsilon4 allele and the risk of Alzheimer disease among African Americans, whites, and Hispanics. *JAMA* **279,** 751–5 (1998).

70. Ramanan, V. K. *et al.* APOE and BCHE as modulators of cerebral amyloid deposition: a florbetapir PET genome-wide association study. *Mol. Psychiatry* (2013). doi:10.1038/mp.2013.19

71. Reiman, E. M. *et al.* Fibrillar amyloid-beta burden in cognitively normal people at 3 levels of genetic risk for Alzheimer's disease. *Proc. Natl. Acad. Sci. U. S. A.* **106,** 6820–5 (2009).

72. Kemppainen, N. M. *et al.* PET amyloid ligand [11C]PIB uptake is increased in mild cognitive impairment. *Neurology* **68,** 1603–6 (2007).

73. Okello, A. *et al.* Conversion of amyloid positive and negative MCI to AD over 3 years: an 11C-PIB PET study. *Neurology* **73,** 754–60 (2009).

74. Shen, L. *et al.* Whole genome association study of brain-wide imaging phenotypes for identifying quantitative trait loci in MCI and AD: A study of the ADNI cohort. *Neuroimage* **53,** 1051–1063 (2010).

75. Potkin, S. G. *et al.* Hippocampal atrophy as a quantitative trait in a genome-wide association study identifying novel susceptibility genes for Alzheimer's disease. *PLoS One* **4,** e6501 (2009).

76. Darvesh, S., Hopkins, D. A. & Geula, C. Neurobiology of butyrylcholinesterase. *Nat. Rev. Neurosci.* **4,** 131–8 (2003).

77. Lehmann, D. J., Johnston, C. & Smith, A. D. Synergy between the genes for butyrylcholinesterase K variant and apolipoprotein E4 in late-onset confirmed Alzheimer's disease. *Hum. Mol. Genet.* **6,** 1933–1936 (1997).

78. Holmes, C. *et al.* Rate of progression of cognitive decline in Alzheimer's disease: effect of butyrylcholinesterase K gene variation. *J. Neurol. Neurosurg. Psychiatry* **76,** 640–3 (2005).

79. Stein, J. L. *et al.* Genome-wide analysis reveals novel genes influencing temporal lobe structure with relevance to neurodegeneration in Alzheimer's disease. *Neuroimage* **51,** 542–54 (2010).

80. Swaminathan, S. *et al.* Amyloid pathway-based candidate gene analysis of [(11)C]PiB-PET in the Alzheimer's Disease Neuroimaging Initiative (ADNI) cohort. *Brain Imaging Behav.* **6,** 1–15 (2012).

81. Thambisetty, M. *et al.* Effect of Complement CR1 on Brain Amyloid Burden During Aging and Its Modification by APOE Genotype. *Biol. Psychiatry* (2012). doi:10.1016/j.biopsych.2012.08.015

82. Hohman, T. J., Koran, M. E. I. & Thornton-Wells, T. A. Interactions between GSK3β and amyloid genes explain variance in amyloid burden. *Neurobiol. Aging* (2013). doi:10.1016/j.neurobiolaging.2013.08.032

83. Meda, S. A., Koran, M. E. I., Pryweller, J. R., Vega, J. N. & Thornton-Wells, T. A. Genetic interactions associated with 12-month atrophy in hippocampus and entorhinal cortex in Alzheimer's Disease Neuroimaging Initiative. *Neurobiol. Aging* **34,** 1518.e9–1518.e18 (2013).

84. Borthakur, A. *et al.* In vivo measurement of T1rho dispersion in the human brain at 1.5 tesla. *J. Magn. Reson. Imaging* **19,** 403–9 (2004).

85. Virta, A., Komu, M. & Kormano, M. T1ρ of protein solutions at very low fields: Dependence on molecular weight, concentration, and structure. *Magn. Reson. Med.* **37,** 53–7 (1997).

86. Aronen, H. J. *et al.* 3D spin-lock imaging of human gliomas. *Magn. Reson. Imaging* **17,** 1001–10 (1999).

87. Santyr, G. E. MR imaging of the breast. Imaging and tissue characterization without intravenous contrast. *Magn. Reson. Imaging Clin. N. Am.* **2,** 673–90 (1994).

88. Regatte, R. R., Akella, S. V. S., Lonner, J. H., Kneeland, J. B. & Reddy, R. T1rho relaxation mapping in human osteoarthritis (OA) cartilage: comparison of T1rho with T2. *J. Magn. Reson. Imaging* **23,** 547–53 (2006).

89. Haris, M. *et al.* T1rho (T(1rho)) MR imaging in Alzheimer' disease and Parkinson's disease with and without dementia. *J.Neurol.* (2010). doi:10.1007/s00415-010-5762-6 [doi]

90. Haris, M. *et al.* T(1rho) MRI in Alzheimer's Disease: Detection of Pathological Changes in Medial Temporal Lobe. *J.Neuroimaging* (2010). doi:JON467 [pii];10.1111/j.1552-6569.2010.00467.x [doi]

91. Haris, M. *et al.* Early marker for Alzheimer's disease: hippocampus T1rho estimation. *J. Magn. Reson. imaging* **29,** 1008–1012 (2009).

92. Borthakur, A., Sochor, M., Davatzikos, C., Trojanowski, J. Q. & Clark, C. M. T1rho MRI of Alzheimer's disease. *Neuroimage* **41,** 1199–205 (2008).

93. Jack, C. R. *et al.* Hypothetical model of dynamic biomarkers of the Alzheimer's pathological cascade. *Lancet Neurol.* **9,** 119–28 (2010).

94. Dale, A., Fischl, B. & Sereno, M. I. Cortical Surface-Based Analysis: I. Segmentation and Surface Reconstruction. *Neuroimage* **9,** 179–194 (1999).

95. Segonne, F. *et al.* A hybrid approach to the skull stripping problem in MRI. *Neuroimage* **22,** 1060–1075 (2004).

96. Fischl, B. *et al.* Automatically Parcellating the Human Cerebral Cortex. *Cereb. Cortex* **14,** 11–22 (2004).

97. Segonne, F., Pacheco, J. & Fischl, B. Geometrically accurate topology-correction of cortical surfaces using nonseparating loops. *IEEE Trans Med Imaging* **26,** 518–529 (2007).

98. Desikan, R. S. *et al.* An automated labeling system for subdividing the human cerebral cortex on MRI scans into gyral based regions of interest. *Neuroimage* **31,** 968–80 (2006).

99. Fischl, B. *et al.* Whole brain segmentation: automated labeling of neuroanatomical structures in the human brain. *Neuron* **33,** 341–55 (2002).

100. Borthakur, A. *et al.* Sodium and T1ρ MRI for molecular and diagnostic imaging of articular cartilage. *NMR Biomed.* **19,** 781–821 (2006).

101. Cobb, J. G., Xie, J., Li, K., Gochberg, D. F. & Gore, J. C. Exchange-mediated contrast agents for spin-lock imaging. *Magn. Reson. Med.* **67,** 1427–33 (2012).

102. *International Review of Research in Mental Retardation: Health Issues in Down Syndrome*. (Academic Press, 2010).

103. Korenberg, J. R. *et al.* VI Genome structure and cognitive map of Williams syndrome. *J.Cogn Neurosci.* **12 Suppl,** 89–107 (2000).

104. Strømme, P., Bjørnstad, P. G. & Ramstad, K. Prevalence estimation of Williams syndrome. *J. Child Neurol.* **17,** 269–71 (2002).

105. Martens, M. A., Wilson, S. J. & Reutens, D. C. Research Review: Williams syndrome: a critical review of the cognitive, behavioral, and neuroanatomical phenotype. *J. Child Psychol. Psychiatry.* **49,** 576–608 (2008).

106. Meyer-Lindenberg, A., Mervis, C. B. & Berman, K. F. Neural mechanisms in Williams syndrome: a unique window to genetic influences on cognition and behaviour. *Nat.Rev.Neurosci.* **7,** 380–393 (2006).

107. Conners, F. A., Moore, M. S., Loveall, S. J. & Merrill, E. C. Memory profiles of Down, Williams, and fragile X syndromes: implications for reading development. *J. Dev. Behav. Pediatr.* **32,** 405–17 (2011).

108. Dykens, E. M., Rosner, B. A., Ly, T. & Sagun, J. Music and anxiety in Williams syndrome: a harmonious or discordant relationship? *Am J Ment.Retard.* **110,** 346–358 (2005).

109. Hocking, D. R., Rinehart, N. J., McGinley, J. L., Moss, S. A. & Bradshaw, J. L. A kinematic analysis of visually-guided movement in Williams syndrome. *J. Neurol. Sci.* **301,** 51–8 (2011).

110. Mobbs, D. *et al.* Frontostriatal dysfunction during response inhibition in Williams syndrome. *Biol. Psychiatry* **62,** 256–61 (2007).

111. Tsai, S.-W., Wu, S.-K., Liou, Y.-M. & Shu, S.-G. Early development in Williams syndrome. *Pediatr. Int.* **50,** 221–4 (2008).

112. Dykens, E. M. Anxiety, fears, and phobias in persons with Williams syndrome. *Dev.Neuropsychol.* **23,** 291–316 (2003).

113. Mervis, C. B. & John, A. E. Cognitive and behavioral characteristics of children with Williams syndrome: implications for intervention approaches. *Am. J. Med. Genet. C. Semin. Med. Genet.* **154C,** 229–48 (2010).

114. Morris, C. A. The behavioral phenotype of Williams syndrome: A recognizable pattern of neurodevelopment. *Am. J. Med. Genet. C. Semin. Med. Genet.* **154C,** 427–31 (2010).

115. Cherniske, E. M. *et al.* Multisystem study of 20 older adults with Williams syndrome. *Am.J.Med.Genet.A* **131,** 255–264 (2004).

116. Reiss, A. L. *et al.* IV. Neuroanatomy of Williams syndrome: a high-resolution MRI study. *J.Cogn Neurosci.* **12 Suppl 1,** 65–73 (2000).

117. Chiang, M.-C. *et al.* 3D pattern of brain abnormalities in Williams syndrome visualized using tensor-based morphometry. *Neuroimage* **36,** 1096–109 (2007).

118. Meda, S. A., Pryweller, J. R. & Thornton-Wells, T. A. Regional Brain Differences in Cortical Thickness, Surface Area and Subcortical Volume in Individuals with Williams Syndrome. *PLoS One* **7,** e31913 (2012).

119. Jernigan, T. L. L., Bellugi, U., Sowell, E., Doherty, S. & Hesselink, J. R. R. Cerebral morphologic distinctions between Williams and Down syndromes. *Arch. Neurol.* **50,** 186–91 (1993).

120. Devenny, D. A. *et al.* Developmental Neuropsychology Age-Associated Memory Changes in Adults With Williams Syndrome. *Dev. Neuropsychol.* **26,** 691–706 (2004).

121. Shultz, J. *et al.* Evaluation of screening tools for dementia in older adults with mental retardation. *Am. J. Ment. Retard.* **109,** 98–110 (2004).

122. Newsom, J. Coding of Categorical Predictors and ANCOVA. (2012). at <http://www.upa.pdx.edu/IOA/newsom/da2/ho_coding1.pdf>

123. Farrer, L. A. *et al.* Effects of age, sex, and ethnicity on the association between apolipoprotein E genotype and Alzheimer disease. *J. Am. Med. Assoc.* **278,** 1349–1356 (1997).

124. Forte, G. I. *et al.* Apolipoprotein E genotypic frequencies among Down syndrome patients imply early unsuccessful aging for ApoE4 carriers. *Rejuvenation Res.* **10,** 293–9 (2007).

125. Storandt, M., Mintun, M. A., Head, D. & Morris, J. C. Cognitive decline and brain volume loss as signatures of cerebral amyloid-beta peptide deposition identified with Pittsburgh compound B: cognitive decline associated with Abeta deposition. *Arch. Neurol.* **66,** 1476–81 (2009).

126. Haier, R. J., Head, K., Head, E. & Lott, I. T. Neuroimaging of individuals with Down's syndrome at-risk for dementia: evidence for possible compensatory events. *Neuroimage.* **39,** 1324–1332 (2008).

127. Kesslak, J. P., Nagata, S. F., Lott, I. & Nalcioglu, O. Magnetic resonance imaging analysis of age-related changes in the brains of individuals with Down's syndrome. *Neurology* **44,** 1039–1045 (1994).

128. Pearlson, G. D. D. *et al.* MRI brain changes in subjects with Down syndrome with and without dementia. *Dev. Med. Child Neurol.* **40,** 326–34 (1998).

129. Pinter, J. D. *et al.* Amygdala and hippocampal volumes in children with Down syndrome: a high-resolution MRI study. *Neurology* **56,** 972–974 (2001).

130. Mann, D. M. & Esiri, M. M. The pattern of acquisition of plaques and tangles in the brains of patients under 50 years of age with Down's syndrome. *J. Neurol. Sci.* **89,** 169–79 (1989).

131. Chou, Y.-Y. *et al.* Mapping genetic influences on ventricular structure in twins. *Neuroimage* **44,** 1312–1323 (2009).

132. Aylward, E. H. *et al.* MRI volumes of the hippocampus and amygdala in adults with Down's syndrome with and without dementia. *Am. J. Psychiatry* **156,** 564–8 (1999).

133. Wishart, H. A. *et al.* Regional brain atrophy in cognitively intact adults with a single APOE epsilon4 allele. *Neurology* **67,** 1221–1224 (2006).

134. Cherbuin, N., Anstey, K. J., Réglade-Meslin, C. & Sachdev, P. S. In vivo hippocampal measurement and memory: a comparison of manual tracing and automated segmentation in a large community-based sample. *PLoS One* **4,** e5265 (2009).

135. Lobo, I. Epistasis: Gene Interaction and the Phenotypic Expression of Complex Diseases Like Alzheimer's. *Nat. Educ.* **1,** (2008).

136. Qin, S. *et al.* An association study of the N-methyl-D-aspartate receptor NR1 subunit gene (GRIN1) and NR2B subunit gene (GRIN2B) in schizophrenia with universal DNA microarray. *Eur. J. Hum. Genet.* **13,** 807–14 (2005).

137. Ma, D. Q. *et al.* Identification of significant association and gene-gene interaction of GABA receptor subunit genes in autism. *Am. J. Hum. Genet.* **77,** 377–388 (2005).

138. Cho YM *et al.* Multifactor-dimensionality reduction shows a two-locus interaction associated with Type 2 diabetes mellitus. *Diabetologia* **47,** 549–554 (2004).

139. Rodríguez-Rodríguez, E. *et al.* Epistasis between intracellular cholesterol trafficking-related genes (NPC1 and ABCA1) and Alzheimer's disease risk. *J. Alzheimers. Dis.* **21,** 619–25 (2010).

140. Rodríguez-Rodríguez, E. *et al.* Interaction between HMGCR and ABCA1 cholesterol-related genes modulates Alzheimer's disease risk. *Brain Res.* **1280,** 166–71 (2009).

141. Mateo, I. *et al.* Epistasis between tau phosphorylation regulating genes (CDK5R1 and GSK-3beta) and Alzheimer's disease risk. *Acta Neurol. Scand.* **120,** 130–3 (2009).

142. Tartaglia, M. C., Rosen, H. J. & Miller, B. L. Neuroimaging in Dementia. *Neurotherapeutics* **8,** 82–92 (2011).

143. Ma, L., Clark, A. G. & Keinan, A. Gene-Based Testing of Interactions in Association Studies of Quantitative Traits. *PLoS Genet.* **9,** e1003321 (2013).

144. Kwon, J. M. & Goate, A. M. The candidate gene approach. *Alcohol Res. Heal.* **24,** 164–168 (2000).

145. Ma, L. *et al.* Knowledge-driven analysis identifies a gene-gene interaction affecting high-density lipoprotein cholesterol levels in multi-ethnic populations. *PLoS Genet.* **8,** e1002714 (2012).

146. Mueller, S. G. *et al.* The Alzheimer's disease neuroimaging initiative. *Neuroimaging Clin. N. Am.* **15,** 869–77, xi–xii (2005).

147. Trojanowski, J. Q. *et al.* Update on the biomarker core of the Alzheimer's Disease Neuroimaging Initiative subjects. *Alzheimers. Dement.* **6,** 230–8 (2010).

148. Saykin, A. J. *et al.* Alzheimer's Disease Neuroimaging Initiative biomarkers as quantitative phenotypes: Genetics core aims, progress, and plans. *Alzheimer's Dement.* **6,** 265–273 (2010).

149. Biffi, A. *et al.* Genetic variation and neuroimaging measures in Alzheimer disease. *Arch. Neurol.* **67,** 677–85 (2010).

150. Purcell, S. *et al.* PLINK: a tool set for whole-genome association and population-based linkage analyses. *Am. J. Hum. Genet.* **81,** 559–75 (2007).

151. Jack, C. R. *et al.* The Alzheimer's Disease Neuroimaging Initiative (ADNI): MRI methods. *J. Magn. Reson. imaging* **27,** 685–91 (2008).

152. Jack, C. R. *et al.* Update on the magnetic resonance imaging core of the Alzheimer's disease neuroimaging initiative. *Alzheimers. Dement.* **6,** 212–20 (2010).

153. Fischl, B. FreeSurfer. *Neuroimage* **62,** 774–81 (2012).

154. Mormino, E. C. *et al.* Episodic memory loss is related to hippocampal-mediated beta-amyloid deposition in elderly subjects. *Brain* **132,** 1310–23 (2009).

155. Reuter, M., Schmansky, N. J., Rosas, H. D. & Fischl, B. Within-Subject Template Estimation for Unbiased Longitudinal Image Analysis. *Neuroimage* **61,** 1402–1418 (2012).

156. Herold, C., Steffens, M., Brockschmidt, F. F., Baur, M. P. & Becker, T. INTERSNP: genome-wide interaction analysis guided by a priori information. *Bioinformatics* **25,** 3275–3281 (2009).

157. Kanehisa, M. & Goto, S. KEGG: kyoto encyclopedia of genes and genomes. *Nucleic Acids Res.* **28,** 27–30 (2000).

158. Kanehisa, M., Goto, S., Sato, Y., Furumichi, M. & Tanabe, M. KEGG for integration and interpretation of large-scale molecular data sets. *Nucleic Acids Res.* **40,** D109–14 (2012).

159. Takeda, S. & Matsuzawa, T. Age-Related Brain Atrophy: A Study With Computed Tomography. *J Gerontol* **40,** 159–163 (1985).

160. Gur, R. C. *et al.* Gender differences in age effect on brain atrophy measured by magnetic resonance imaging. *Proc. Natl. Acad. Sci.* **88,** 2845–2849 (1991).

161. Brayne, C. *et al.* Education, the brain and dementia: neuroprotection or compensation? *Brain* **133,** 2210–6 (2010).

162. Jack, C. R. *et al.* Comparison of different MRI brain atrophy rate measures with clinical disease progression in AD. *Neurology* **62,** 591–600 (2004).

163. Jolles, J., Bothmer, J., Markerink, M. & Ravid, R. Phosphatidylinositol kinase is reduced in Alzheimer's disease. *J. Neurochem.* **58,** 2326–9 (1992).

164. Stokes, C. E. & Hawthorne, J. N. Reduced Phosphoinositide Concentrations in Anterior Temporal Cortex of Alzheimer-Diseased Brains. *J. Neurochem.* **48,** 1018–1021 (1987).

165. Bothmer, J., Markerink, M. & Jolles, J. Phosphoinositide kinase activities in synaptosomes prepared from brains of patients with Alzheimer's disease and controls. *Neurosci. Lett.* **176,** 169–172 (1994).

166. Franke, T. F., Kaplan, D. R., Cantley, L. C. & Toker, A. Direct regulation of the Akt proto-oncogene product by phosphatidylinositol-3,4-bisphosphate. *Science* **275,** 665–8 (1997).

167. Dudek, H. *et al.* Regulation of Neuronal Survival by the Serine-Threonine Protein Kinase Akt. *Science (80-.).* **275,** 661–665 (1997).

168. Martín, D. *et al.* Effect of the Alzheimer amyloid fragment Aβ(25-35) on Akt/PKB kinase and survival of PC12 cells. *J. Neurochem.* **78,** 1000–1008 (2001).

169. Malagelada, C., Jin, Z. H. & Greene, L. A. RTP801 is induced in Parkinson's disease and mediates neuron death by inhibiting Akt phosphorylation/activation. *J. Neurosci.* **28,** 14363–71 (2008).

170. Nemoto, Y. *et al.* Identification and characterization of a synaptojanin 2 splice isoform predominantly expressed in nerve terminals. *J. Biol. Chem.* **276,** 41133–42 (2001).

171. Datson, N. A. *et al.* A molecular blueprint of gene expression in hippocampal subregions CA1, CA3, and DG is conserved in the brain of the common marmoset. *Hippocampus* **19,** 739–52 (2009).

172. Aston, C., Jiang, L. & Sokolov, B. P. Transcriptional profiling reveals evidence for signaling and oligodendroglial abnormalities in the temporal cortex from patients with major depressive disorder. *Mol. Psychiatry* **10,** 309–22 (2005).

173. Lopez, L. M. *et al.* Evolutionary conserved longevity genes and human cognitive abilities in elderly cohorts. *Eur. J. Hum. Genet.* **20,** 341–7 (2012).

174. Nagamani, S. C. S. *et al.* Interstitial deletion of 6q25.2-q25.3: a novel microdeletion syndrome associated with microcephaly, developmental delay, dysmorphic features and hearing loss. *Eur. J. Hum. Genet.* **17,** 573–81 (2009).

175. Pattin, K. A. & Moore, J. H. Exploiting the proteome to improve the genome-wide genetic analysis of epistasis in common human diseases. *Hum. Genet.* **124,** 19–29 (2008).

176. Neale, B. & Sham, P. The future of association studies: gene-based analysis and replication. *Am. J. Hum. Genet.* **75,** 353–62 (2004).

177. Jagust, W. J. *et al.* The Alzheimer's Disease Neuroimaging Initiative positron emission tomography core. *Alzheimers. Dement.* **6,** 221–9 (2010).

178. Jagust, W. J. *et al.* Relationships between biomarkers in aging and dementia. *Neurology* **73,** 1193–9 (2009).

179. Landau, S. M. & Jagust, W. J. Florbetapir Processing Methods. (2012). at <http://adni.loni.ucla.edu/methods/pet-analysis/>

180. Kim, S. *et al.* Functional interaction of neuronal Cav1.3 L-type calcium channel with ryanodine receptor type 2 in the rat hippocampus. *J. Biol. Chem.* **282,** 32877–89 (2007).

181. Ouardouz, M. *et al.* Depolarization-Induced Ca2+ Release in Ischemic Spinal Cord White Matter Involves L-type Ca2+ Channel Activation of Ryanodine Receptors. *Neuron* **40,** 53–63 (2003).

182. Jack, C. R. *et al.* Tracking pathophysiological processes in Alzheimer's disease: an updated hypothetical model of dynamic biomarkers. *Lancet Neurol.* **12,** 207–16 (2013).

183. Berridge, M. J. Calcium hypothesis of Alzheimer's disease. *Pflugers Arch.* **459,** 441–9 (2010).

184. Querfurth, H. W. & Selkoe, D. J. Calcium Ionophore Increases Amyloid beta Peptide Production by Cultured Cells. *Biochemistry* **33,** 4550–4561 (1994).

185. Pierrot, N. *et al.* Calcium-mediated transient phosphorylation of tau and amyloid precursor protein followed by intraneuronal amyloid-beta accumulation. *J. Biol. Chem.* **281,** 39907–14 (2006).

186. Itkin, A. *et al.* Calcium ions promote formation of amyloid β-peptide (1-40) oligomers causally implicated in neuronal toxicity of Alzheimer's disease. *PLoS One* **6,** e18250 (2011).

187. Kelliher, M. *et al.* Alterations in the ryanodine receptor calcium release channel correlate with Alzheimer's disease neurofibrillary and beta-amyloid pathologies. *Neuroscience* **92,** 499–513 (1999).

188. Supnet, C., Grant, J., Kong, H., Westaway, D. & Mayne, M. Amyloid-beta-(1-42) increases ryanodine receptor-3 expression and function in neurons of TgCRND8 mice. *J. Biol. Chem.* **281,** 38440–7 (2006).

189. Oulès, B. *et al.* Ryanodine receptor blockade reduces amyloid-β load and memory impairments in Tg2576 mouse model of Alzheimer disease. *J. Neurosci.* **32,** 11820–34 (2012).

190. Ueda, K., Shinohara, S., Yagami, T., Asakura, K. & Kawasaki, K. Amyloid beta protein potentiates Ca2+ influx through L-type voltage-sensitive Ca2+ channels: a possible involvement of free radicals. *J. Neurochem.* **68,** 265–71 (1997).

191. Mattson, M. *et al.* beta-Amyloid peptides destabilize calcium homeostasis and render human cortical neurons vulnerable to excitotoxicity. *J. Neurosci.* **12,** 376–389 (1992).

192. Scragg, J. L. *et al.* Alzheimer's amyloid peptides mediate hypoxic up-regulation of L-type Ca2+ channels. *FASEB J.* **19,** 150–2 (2005).

193. Anekonda, T. S. *et al.* L-type voltage-gated calcium channel blockade with isradipine as a therapeutic strategy for Alzheimer's disease. *Neurobiol. Dis.* **41,** 62–70 (2011).

194. Fruen, B. R., Mickelson, J. R. & Louis, C. F. Dantrolene inhibition of sarcoplasmic reticulum Ca2+ release by direct and specific action at skeletal muscle ryanodine receptors. *J. Biol. Chem.* **272,** 26965–71 (1997).

195. Giannini, G. The ryanodine receptor/calcium channel genes are widely and differentially expressed in murine brain and peripheral tissues. *J. Cell Biol.* **128,** 893–904 (1995).

196. Perez-Reyes, E., Wei, X. Y., Castellano, A. & Birnbaumer, L. Molecular diversity of L-type calcium channels. Evidence for alternative splicing of the transcripts of three non-allelic genes. *J. Biol. Chem.* **265,** 20430–6 (1990).

197. Bhat, S. *et al.* CACNA1C (Ca(v)1.2) in the pathophysiology of psychiatric disease. *Prog. Neurobiol.* **99,** 1–14 (2012).

198. Buxbaum, J. D., Ruefli, A. A., Parker, C. A., Cypess, A. M. & Greengard, P. Calcium regulates processing of the Alzheimer amyloid protein precursor in a protein kinase C-independent manner. *Proc. Natl. Acad. Sci. U. S. A.* **91,** 4489–93 (1994).

199. Chavis, P., Fagni, L., Lansman, J. B. & Bockaert, J. Functional coupling between ryanodine receptors and L-type calcium channels in neurons. *Nature* **382,** 719–22 (1996).

200. Squecco, R., Bencini, C., Piperio, C. & Francini, F. L-type Ca2+ channel and ryanodine receptor cross-talk in frog skeletal muscle. *J. Physiol.* **555,** 137–52 (2004).

201. Cannell, M. B. & Soeller, C. Numerical analysis of ryanodine receptor activation by L-type channel activity in the cardiac muscle diad. *Biophys. J.* **73,** 112–22 (1997).

202. Greene, C. S., Penrod, N. M., Williams, S. M. & Moore, J. H. Failure to replicate a genetic association may provide important clues about genetic architecture. *PLoS One* **4,** e5639 (2009).

203. Koskinen, S. K., Niemi, P. T., Kajander, S. A. & Komu, M. E. S. T1rho Dispersion profile of rat tissues in vitro at very low locking fields. *Magn. Reson. Imaging* **24,** 295–9 (2006).